Magnetic and Physical Characteristics of Magnetite Associated with Deformation and Exsolution

A DISSERTATION
SUBMITTED TO THE FACULTY OF THE GRADUATE SCHOOL
OF THE UNIVERSITY OF MINNESOTA
BY

Jessica Lynn Till

IN PARTIAL FULFILLMENT OF THE REQUIREMENTS
FOR THE DEGREE OF
Doctor of Philosophy

Bruce M. Moskowitz, advisor

October, 2011

Acknowledgements

I have had lots of help along the way during my graduate studies, and I am grateful to many people for their advice, shared expertise, support, and encouragement. Thanks to my parents, sister, and the rest of my family for being unfailingly positive about my academic pursuits and cheering me on along the way. My partner Maxwell Brown has been endlessly supportive and encouraging beyond anything I could have asked for.

I cannot thank my advisor Bruce Moskowitz enough for everything I have been able to learn and do during my time in graduate school. I am grateful for his encouragement to seek out interesting problems and for providing every possible opportunity to freely pursue them. I thank Mike Jackson for being an incredible resource of knowledge and experience, and I have benefitted very much from his patient explanations and insights into my work. The Institute for Rock Magnetism has been a wonderful academic home during my PhD and I am lucky to have been surrounded by such a collection of estimable colleagues there. I am very appreciative of the efforts of IRM staff members Julie Bowles and Peat Solheid for helping to make my lab work go smoothly and for keeping the lab running in general. Also thanks to Brian Carter, Ioan Lascu, Thelma Berquo, Anna Lindquist, Evan Finnes and the other current and former members of the IRM. I have enjoyed their friendship, camaraderie and encouragement, in addition to the benefit of their scientific expertise.

I am deeply grateful to David Kohlstedt for help and research guidance from the start, and am glad to have had the chance to learn so much from him. I very much appreciate having had access to his excellent rock and mineral physics lab. Much of the work in this thesis would not have been possible without Mark Zimmermann and his extensive expertise and help in planning and performing experiments in the lab. I also thank the students and post-docs of the Kohlstedt lab for teaching me much about the

mysteries of laboratory deformation, and for sharing their time and knowledge in the lab.

I thank Jim Stout for inspiring some of the ideas for experiments in this thesis, and for many thoughtful and insightful scientific discussions over the years. Thanks also to Marc Hirschmann and Josh Feinberg for sharing expert knowledge and advice on some of my research ideas. I have appreciated the fellowship of many graduate students and post-docs in the department over the years and thank them for making my time in Minneapolis memorable.

I owe many thanks to Bruce Watson for generously sharing the code to his diffusion model for rutile needle growth in quartz, which I adapted for the modeling in Chapter 3, and for providing many helpful insights and advice on aspects of mineral chemistry. Thanks also to the reviewers and journal editors of the manuscripts reproduced in Chapters 2 and 4 for making helpful improvements and suggestions.

The majority of this research was supported by an EAR grant from the National Science Foundation. The Mineralogical Society of America is thanked for providing a student research grant for experimental work. The Geological Society of America also provided a student research grants for various parts of the work presented here. The Department of Earth Sciences at the University of Minnesota is thanked for providing several graduate fellowships throughout my PhD. Thanks also to the department for generally providing such a stimulating and friendly environment in which to work for the past several years.

Abstract

This thesis contains a collection of laboratory-based studies designed to characterize the magnetic properties and physical aspects of magnetite that result from deformation or high temperature growth. In Chapter 2, a detailed rock magnetic characterization of rocks containing nanoscale magnetite exsolved from volcanic glass identifies the location of domain-state thresholds through distinct transitions in remanence and susceptibility properties. This unique material is an excellent candidate for standard material to be used in studies of magnetite granulometry.

In Chapter 3, theoretical timescales for the growth of sub-microscopic magnetite needles during exsolution from plagioclase are calculated using results of diffusion experiments. Measured diffusivities are modeled to calculate the amount of diffusion-limited growth possible under different conditions of nucleation temperature and cooling rate.

In Chapters 4 and 5, the development and evolution of magnetic fabrics are investigated through deformation experiments on synthetic rock-analogues at high temperatures and ductile conditions. Stress-induced changes in rock magnetic properties after deformation are significant. Examination of deformation-induced remagnetization demonstrates that a primary remanence can survive conditions equivalent to moderate metamorphism in certain cases and that petrofabric can play an important role in determining the remanence stability. High-temperature deformation experiments result in a pattern of anisotropy development that indicates plastic deformation of magnetic grains, which is distinct from anisotropy development resulting from different magnetite strain responses. Experimental data are combined with theoretical magnetic anisotropy models and used to estimate effective magnetite strains and strain partitioning from magnetic fabric data in deformed samples.

Finally, observations of strong shape-preferred orientation and deformation-induced microstructures in magnetite grains from high-temperature shear experiments indicate plastic deformation of magnetite. Microstructural observations place constraints on the rheological behavior of magnetite and the conditions in which dislocation creep is dominant. These observations prompt a re-examination of the previously established magnetite flow laws which are modified and used to construct new deformation

mechanism maps.

Contents

List of Tables

List of Figures

Chapter 1

Introduction

A number of high-temperature processes are responsible for producing the magnetic properties of solid rocks and the physical characteristics of the associated magnetic particles within. Magnetic signatures of rocks are strongly influenced by ancient conditions of temperature, pressure, and magnetic field, but laboratory studies are necessary to understand how these factors combine to produce the magnetic properties observed in nature. Simulated metamorphic conditions in laboratory studies can provide insight into the magnetic and mechanical behavior of magnetic minerals in the Earths crust. The effects of elevated temperature and pressure on fundamental magnetic properties are important for understanding the performance of magnetic minerals as paleomagnetic recorders. Understanding the response of magnetic minerals to deformation is needed to improve the utility of magnetic fabric analysis to tectonic studies, and to characterize the rheological behavior of common crustal minerals. Magnetite is the most important magnetic mineral to paleomagnetism and applied rock magnetism and is the most frequent target of laboratory studies in fundamental rock magnetism.

This thesis investigates the fundamental behavior of magnetite under geologically significant conditions and discusses the implications for palaeomagnetism and applied rock magnetism. The topics of research addressed here are broadly divided into two categories:

1. The occurrence and significance of nanoscale magnetite particles, including a characterization of the diagnostic size-sensitive magnetic properties associated with

them (Chapter 2), and the kinetics of the growth process by which they may form during exsolution from feldspar (Chapter 3).

2. The effects of deformation on magnetite particles, including the development and evolution of magnetic anisotropy in deforming rocks (Chapters 4 and 5) and features indicative of plastic deformation in magnetite (Chapter 6).

Nanoscale magnetite particles are often magnetically structured in the single-domain state and capable of carrying a strong and stable remanence (Dunlop & Özdemir, 1997). In nature, assemblages of single-domain magnetite grains with weak or no interactions can be found as exsolution features in Fe-bearing silicate phases such as pyroxenes, feldspars, or pyroclastic and basaltic glasses. Such particles are often ideal paleomagnetic recorders over geologically long time periods (Renne et al., 2002; Tarduno et al., 2006). Magnetite particles as small as 10 nm in diameter have been synthesized (Maher, 1988) and can be studied in materials such as ferrofluid (Dunlop & Carter-Stiglitz, 2006; Jackson et al., 2006). However, synthesized particles can have broad size distributions and assemblages of such particles are often strongly interacting due to the difficulty of dispersing magnetic grains (Worm & Jackson, 1999). Attempts to correlate specific rock magnetic properties to magnetite grain size are often restricted to determining the range of grain size and shape corresponding to a particular domain state based on theoretical predictions such as those of Butler & Banerjee (1975).

In Chapter 2, a collection of rock magnetic measurements is presented from an ashflow tuff containing nanoscale magnetite particles exsolved from volcanic glass. In a densely sampled stratigraphic section, systematic variations in grain-size sensitive magnetic properties are observed with height above the base of the flow. A progressive increase in magnetite grain size resulted from a cooling rate gradient in the unit. Distinct transitions in magnetic properties demarcate the grain size thresholds that represent transitions to different magnetic domain states. The very fine-grained magnetite particles in these rocks are rather unique in that they have narrow grain size distributions at each stratigraphic level and their uniform dispersion in the host glass minimizes the effect of magnetic interactions that would otherwise mask the grain-size dependence of many magnetic properties. Because both of these features are difficult to achieve with synthetic magnetite particles, the Tiva Canyon rocks represent a useful

standard for interpreting magnetite grain size from magnetic properties in natural rocks and sediments. The contents of Chapter 2 are published in the journal *Geochemistry, Geophysics, Geosystems* (Till et al., 2011).

The work presented in Chapter 3 attempts to determine the physical conditions of time and temperature that are likely to produce growth of single domain nanoscale magnetite in silicates. Exsolved silicate-hosted magnetite needles are important remanence carriers for studies of paleointensity and seafloor magnetism (Davis, 1981; Smirnov et al., 2003). Chapter 3 also addresses the question of whether complicated magnetic remanence can be acquired by magnetite growth along certain temperature paths, and whether such particles will be reliable recorders of paleomagnetic field direction and intensity. This topic is approached by presenting the results of annealing experiments to measure chemical diffusion of Fe in plagioclase. Fe diffusivities can be used to calculate time-temperature paths of diffusion-limited magnetite needle growth during exsolution from feldspar. Based on a preliminary analysis of Fe diffusion profiles measured with Rutherford backscattering spectrometry, an approximate rate law for Fe diffusion in plagioclase has been established. Limited evidence for water-enhanced diffusivity in some experiments raises the possibility that the presence of fluids or other forms of water-enrichment may have a significant impact on the kinetics of magnetite exsolution in nature. Theoretical timescales of magnetite growth depend strongly on cooling rates but the question of whether significant magnetite growth is possible below magnetic ordering temperatures ultimately relies on the future development of a geochemical solution model for Fe in plagioclase. The work presented in Chapter 3 is being prepared for submission to a publication still to be determined.

Chapters 4-6 investigate a range of questions associated with deformation-induced changes in magnetite through a series of laboratory deformation experiments on synthetic samples. Pertinent questions include: how stable is a primary magnetic remanence during deformation? What grain-scale processes are capable of inducing permanent remagnetization? How do magnetic and grain shape anisotropy change with different magnetite strain responses? Can magnetic fabric analysis be used to determine bulk rock strains or provide other information about thermotectonic histories? What conditions are necessary for plastic deformation of magnetite?

Anisotropy of magnetic susceptibility (AMS) has long been recognized as a useful

microstructural indicator in field studies of deformed rocks since the work of Graham (1966) who recognized a pattern between the principal directions of AMS and finite strain. While AMS has been shown to be a reliable indicator of paleostress directions and local changes in relative strain (Tarling & Hrouda, 1993; Borradaile & Jackson, 2004), the ability to extract quantitative strain information from magnitudes of magnetic anisotropy has eluded researchers. Factors such as strain partitioning, pre-deformational fabrics, and successive deformation events can complicate the interpretation of magnetic fabrics in terms of strain histories (Evans et al., 2003). While some studies have identified site-specific correlations between magnitudes of AMS and strain (Kneen, 1976; Kligfield et al., 1983; Cogné & Perroud, 1988), there is no indication that such relationships can be generalized to other rock types or tectonic settings. If it is possible to establish robust laboratory relationships between deformation parameters and magnetic anisotropy, magnetic fabric analysis may find much broader application to tectonic studies; however, it is also important to identify the limitations of the technique.

Previous experimental studies of magnetic fabrics involved room-temperature deformation work to study anisotropy development (Borradaile & Alford, 1988; Jackson et al., 1993), but crystal-plastic processes were absent in earlier experiments. Although models of theoretical magnetic anisotropy development exist for several different magnetic minerals and strain responses (Owens, 1974; Hrouda, 1993), these models are seldom applied to field studies of magnetic fabrics for interpretation of strain or deformation modes. Chapters 4 and 5 investigate patterns of magnetic anisotropy development in synthetic material deformed under elevated temperatures and pressures while also examining syn-deformational remagnetization processes.

Chapter 4 focuses on the physical processes that produce magnetic anisotropy in rocks deformed at moderate temperatures. This work examines the potential importance of magnetic anisotropy to paleomagnetic studies by influencing the stability of a natural remanence during deformation. Since some degree of anisotropy is present in a majority of crystalline rocks (Bouchez, 1997), these results deserve consideration in paleomagnetic studies of weakly metamorphosed terranes. Better understanding of paleomagnetic data quality in tectonized regions will help in understanding apparent polar wander paths, paleomagnetism-based tectonic plate reconstructions, and long term magnetic field behavior. The orientation relationships between the pre-existing fabric, a

primary remanence direction, and the principal stress directions associated with a later metamorphic or deformation event appear to play a role in determining the robustness of the primary remanence to the destructive effects of temperature and stress. The effects of pre-existing anisotropy on formation of deformation-induced magnetic fabric are also investigated. Chapter 4 has been published in similar form in *Geochemistry, Geophysics, Geosystems* (Till et al., 2010).

Chapter 5 is an investigation of magnetic fabric development under highly-ductile conditions at elevated temperatures designed to facilitate plastic deformation of magnetite. The magnitude of magnetic anisotropy resulting from high-temperature deformation is compared with the lower-temperature experiments from Chapter 4. Although only a handful of published examples of magnetic fabrics from rocks containing plastically deformed magnetite exist (Ruf et al., 1988; Housen et al., 1995), these are also compared with the high-temperature results. Theoretical strain response models of magnetic fabric development are applied to the empirical data to obtain approximate magnetite strains and compared with shape-preferred orientation of magnetite grains after deformation. Strain partitioning between magnetite and the silicate matrix are evident from patterns of magnetic fabric formation, which provide constraints on viscosity ratios. Chapter 5 is being prepared for submission to *Geophysical Journal International*.

Chapter 6 follows up on the descriptions of magnetic fabrics resulting from deformed magnetite with a study of microstructural features in deformed magnetite. The typical occurrence of magnetite as an accessory mineral in many rocks may be responsible for the lack of attention devoted to determining its relative rheological behavior and deformation state in field studies. A small number of experimental deformation studies on magnetite exist (Muller & Siemes, 1972; Hennig-Michaeli & Siemes, 1975, 1982; Crouch & Robertson, 1990), but the limited range of deformation conditions previously investigated are insufficient to describe the general deformation behavior of magnetite (Siemes et al., 1991). Even fewer studies on crystallographic texture development for magnetite have been published, and none at high temperatures (Muller & Siemes, 1972). However, highly-strained magnetite-rich rocks are found in some iron formations and oceanic crustal shear zones (Agar & Lloyd, 1997; Natland, 2002; Barbosa & Lagoeiro, 2010) so knowledge of rheological behavior in magnetite is useful for interpreting the conditions under which such rocks were deformed.

In the work presented in Chapter 6, crystallographic-preferred orientations of magnetite are measured and compared with internal microstructures in deformed grains. Misorientation analysis is applied to determine dominant slip systems in individual grains which are compared with previous observations of slip modes in other spinel-structured phases. Temperature-dependent microstructures are interpreted in terms of dominant deformation mechanisms. The observed magnetite strains prompt a re-examination of previously published theoretical flow laws for magnetite, which are modified and used to construct new deformation mechanism maps for magnetite. However, mechanical data from deformation experiments designed to directly study the conditions of magnetite plasticity will be useful in refining the deformation mechanism maps. Chapter 6 is being prepared for submission to *Earth and Planetary Science Letters.*

Chapter 2

Magnetic Properties in an Ashflow Tuff with Continuous Grain Size Variation: A Natural Reference for Magnetic Particle Granulometry

[1] The Tiva Canyon Tuff contains dispersed nanoscale Fe-Ti-oxide grains with a narrow magnetic grain-size distribution, making it an ideal material in which to identify and study grain-size-sensitive magnetic behavior in rocks. A detailed magnetic characterization was performed on samples from the basal 5 m of the tuff. The magnetic materials in this basal section consist primarily of (low-impurity) magnetite in the form of elongated sub-micron grains exsolved from volcanic glass. Magnetic properties studied include bulk magnetic susceptibility, frequency-dependent and temperature-dependent magnetic susceptibility, anhysteretic remanence acquisition, and hysteresis properties. The combined data constitute a distinct magnetic signature at each stratigraphic level

[1] Reproduced by permission of American Geophysical Union. Till, J., Jackson, M., Rosenbaum, J., Solheid, P., Magnetic properties in an ash flow tuff with continuous grain size variation: A natural reference for magnetic particle granulometry, *Geochemistry Geophysics Geosystems*, 12(7), Q07Z26, 2011.

in the section corresponding to different grain-size distributions. The inferred magnetic domain state changes progressively upward from superparamagnetic grains near the base, to particles with pseudo-single domain or metastable single domain characteristics near the top of the sampled section. Direct observations of magnetic grain-size confirm that distinct transitions in room temperature magnetic susceptibility and remanence probably denote the limits of stable single domain behavior in the section. These results provide a unique example of grain-size-dependent magnetic properties in non-interacting particle assemblages over three decades of grain size, including close approximations of ideal Stoner-Wohlfarth assemblages, and may be considered a useful reference for future rock magnetic studies involving grain-size-sensitive properties.

2.1 Introduction

The magnetic remanence characteristics of magnetic particles are strongly size-dependent. Therefore, being able to constrain magnetic particle sizes and domain states through measurement of magnetic properties is important for determining a rock's capacity for carrying a stable remanence. In magnetite, the most stable remanence is typically held in fine, submicron-sized grains. However, particles in this size range are the most difficult to study because their concentrations are low in natural samples and it is often not straightforward to image them, even with high-resolution techniques, and because of difficulties in dispersing synthetic particles well enough to eliminate magnetic interaction effects.

The Tiva Canyon Tuff of the Paintbrush Group is a rhyolitic welded ash-flow sheet that extends across Yucca Mountain, and through much of the nuclear test site in southern Nevada. The main part of the Tiva Canyon Tuff is compositionally zoned and covers a total area of more than 2,600 km^2 with an average thickness of about 120 m (Byers et al., 1976). $^{40}Ar/^{39}Ar$ dating puts the age of this sheet at 12.7 Ma (Sawyer et al., 1994). The magnetic properties of the Tiva Canyon Tuff have long been of interest in rock magnetism due to the narrow grain-size distribution and high dispersion of magnetic particles that greatly reduces magnetic interaction effects. Because these properties are rarely found in natural rocks, this tuff provides a unique opportunity to

isolate the effects of magnetic grain size on size-sensitive magnetic properties, particularly in the very fine superparamagnetic (SP) and small single-domain (SD) domain size ranges for magnetite.

We present here a collection of rock magnetic results from a densely sampled section of the Tiva Canyon Tuff with continuously changing grain size above the base of the unit. These data complement earlier magnetic studies on a small number of these and similar samples (Schlinger et al., 1991; Rosenbaum, 1993; Worm & Jackson, 1999; Pike et al., 2001; Egli & Lowrie, 2002; Jackson et al., 2006). The results of this work are intended to help elucidate the changes in magnetic behavior of very fine magnetic particles that occur with progressive increases in grain size for magnetic grain assemblages that closely approximate ideal Stoner-Wohlfarth populations.

The principal remanence carriers in various sections of the Tiva Canyon Tuff have been previously determined to consist of two distinct ferrimagnetic components (Schlinger et al., 1991; Rosenbaum, 1993). One component comprises multi-domain (MD) titanomagnetite phenocrysts that were present in the magma chamber of the source caldera prior to eruption. The other component consists of Fe-oxide microcrystals that precipitated from volcanic glass after emplacement of the pyroclastic material. However, Rosenbaum (1993) determined that while the MD phenocrysts are important remanence carriers in the middle section, Fe-oxide microcrystals are the primary carrier of remanence and magnetic susceptibility in the two 15-m-thick zones at the bottom and top of the unit. Therefore, variations in magnetic properties in the basal section of the Tiva Canyon Tuff are directly related to the size of Fe-oxide microcrystals, whose growth is in turn dependent on different cooling rates within the unit. The composition of the oxide microcrystals has been characterized as slightly impure magnetite, with an average composition around $Fe_{2.9}A_{0.1}O_4$ where A represents substitutional cations (Jackson et al., 2006). The impurities are mainly Mn and Cr, with minor amounts of Ti according to semiquantitative compositional analysis by Schlinger et al. (1991).

2.2 Samples and Measurements

Samples were collected from a 5-m-thick section of the basal zone of the Tiva Canyon Tuff. The section is located on the west flank of Yucca Mountain, in the Topopah Springs

Quadrangle (36.82°N, 116.47°W) and corresponds to a site sampled by Rosenbaum et al. (1991) and Site IV of Schlinger et al. (1991). Samples were primarily collected as drilled cylindrical cores of 2.5 cm diameter, and were taken directly adjacent to the drill core holes left by previous studies. Hand samples were also collected in intervals with poor exposure for drilling (Table 2.1). The three-digit suffix on the end of each sample name reflects the stratigraphic height above the base of the unit in cm. Transmission electron microscope (TEM) observations by Schlinger et al. (1991) demonstrate that Fe-oxide microcrystals in glass in the ash-flow are spatially well-dispersed with a narrow grain-size distribution and elongated shapes. Various magnetic analyses by Worm & Jackson (1999), Pike et al. (2001), Egli & Lowrie (2002), and Shcherbakov & Fabian (2005) determined that magnetostatic interactions were detectable but weak in samples from the lower 2 m of the unit.

The Fe-oxide grain sizes and shapes measured by Schlinger et al. (1991) that correspond to our samples taken at equivalent heights within the bottom 2.5 m of the unit are listed in Table 2.1. From measurements reported by Schlinger et al. (1991) there is evidently a trend toward increasing grain aspect ratios with height in the studied section (Figure 2.1b). A small number of specimens from sampling heights above 2.5 m were polished using progressively finer grades of diamond lapping films and were analyzed with a scanning electron microscope (SEM) to verify the continuous increase in microcrystal dimensions. These observations are also included in Table 2.1. Although the resolution of the images is not great enough to make precise particle size measurements, the Fe-oxide laths appear to reach a size of around 1 μm long and 0.1 μm wide at the top of the section 2.2. Oxide particles in samples below 3.95 m could not conclusively be identified in SEM images. Magnetic-particle volumes calculated from the published TEM measurements have an approximately logarithmic increase in grain volume with sample height, z (Figure 2.1a). Thus, the variations in magnetic properties that we report as a function of stratigraphic height may be equivalently viewed roughly as a function of log-grain size.

Schlinger et al. (1991) observed a transition from what they termed the basal subzone to the middle subzone of the Tiva Canyon Tuff several meters above the base of the unit, noting a color change associated with this transition. In both TEM and optical microscope observations of samples from the middle subzone, Schlinger et al. (1991)

saw Fe-oxides in the form of tangles and linear aggregates of elongated magnetite. They suggested that these non-uniform distributions of Fe-oxide particles in glass signify a transition from homogeneous to heterogeneous nucleation between the basal and middle subzones. For the samples in the present study, we observe elongated microscale oxides in glass in sample TC04-395 with approximate particle lengths around 0.5 μm (Figure 2.2a). In this sample, two-particle intergrowths appear occasionally, but magnetite primarily occurs as dispersed, isolated grains. Above this height, samples TC04-455 and TC04-502 contain some dispersed Fe-oxide grains, but magnetite occurs primarily as clusters of elongated particles identical to those shown in Figure 11 of Schlinger et al. (1991), that appear to have nucleated heterogeneously. Sample TC04-502 is also noticeably darker in color than the lower samples. Therefore, it seems likely that the transition from the basal to the middle subzone in our sampled section lies between 4 and 4.5 m above the base of unit. Because the clustered magnetite particles in the middle subzone are closely spaced, we may expect the magnetic properties in the highest part of the section to be influenced by magnetic interactions.

For all samples, room temperature low-field bulk magnetic susceptibility, χ_0, was measured on a KLY-2 Kappabridge AC susceptibility meter. For selected samples, low-temperature frequency dependent magnetic susceptibilities were measured from 10 to 300 K or from 10 to 400 K using a Quantum Designs Magnetic Properties Measurement System at frequencies between 1 and 1000 Hz.

All samples were subjected to a 3-axis alternating field demagnetization with a maximum field of 200 mT. After demagnetization, samples were given an anhysteretic remanent magnetization (ARM) in an arbitrary direction using a direct current bias field of 0.01 mT. The anhysteretic susceptibility, χ_{ARM}, was determined by normalizing the remanent magnetization by the strength of the bias field. Remanence measurements were performed on a 2-G Enterprises superconducting 760-R SQUID magnetometer. Hysteresis loops were measured for representative samples on a Princeton Measurements Corporation MicroMag 2900 vibrating sample magnetometer with a saturating field of 1.0 T.

2.3 Results

2.3.1 Magnetic Susceptibility Measurements

Bulk magnetic susceptibility rises approximately linearly with stratigraphic height to a sharp maximum in samples TC04-075a, TC04-075b, and TC04-080 (Figure 2.3a), at approximately 0.75-0.80 m above the base of the unit. Above this level, χ_0 decreases continuously with increasing stratigraphic height and becomes nearly constant above 3.0 m. This pattern is similar to the variation in χ_0 theorized for an ideal collection of particles with increasing grain volume near the transition from a SP magnetic domain state to a stable SD state (e.g., O′Reilly, 1984, ch.4). The saturation magnetization, M_s (see next section) does not vary strongly as a function of stratigraphic position, and therefore the concentration of ferrimagnetic material is relatively uniform and does not account for the $\chi_0(z)$ pattern. The peak in χ_0 at around 0.80 m corresponds to a χ_0/M_s ratio of about $8\text{x}10^{-5}$ m/A, which indicates a dominant magnetic grain size near the SP-SD boundary at room-temperature (e.g., Hunt et al., 1995a).

Low-temperature (T<400 K) measurements of alternating current (AC) susceptibility have a significant frequency dependence at low temperatures, and a unique AC susceptibility signature for each stratigraphic level (Figure 2.4). Sample numbers TC04-255 and lower (z=2.55 m) have pronounced frequency dependence over a limited temperature spectrum, the range of which varies according to sample position. The temperature range of frequency dependence shifts to higher temperatures with increasing stratigraphic height, and the frequency dependence becomes negligible over the measured temperature range at ∼3.25 m (sample TC04-325). For samples with local maxima in low-temperature susceptibility, the location of the peaks represents blocking temperatures at that particular frequency. The highest blocking temperatures are indicated for the highest AC frequencies and they shift to lower temperatures with lower frequencies. Within the temperature range of observable frequency dependence, an out-of-phase component of susceptibility is also evident for each sample. The room-temperature frequency dependence (300 K, Figure 2.4) is strongest in sample TC04-080 (0.80 m), which coincides with the location of maximum χ_0 in the section.

2.3.2 Remanence and Hysteresis Measurements

χ_{ARM} decreases slightly with stratigraphic height up to 0.75 m (the location of the sharp peak in χ_0), then increases to a peak at 3.25 m, and then decreases above 3.25 m (Figure 2.3a). The maximum in χ_{ARM} is thought to represent the upper limit of stable SD behavior in the section. The samples have continuously varying χ_0 and χ_{ARM} values, therefore we display these data on a bivariate plot using the method of relative magnetic grain size determination described by Banerjee et al. (1981) and King et al. (1982) (Figure 2.5a). In this plot we see three distinct trends corresponding to three magnetic domain states. The lowest samples from the studied section have small values of χ_{ARM} that are typical of SP material and plot along the abscissa. Samples in the SD region are characterized by a smooth progression from a maximum in χ_0 and a minimum in χ_{ARM} at the low end of the SD size range, to lower χ_0 and higher χ_{ARM} with increasing grain volume. Samples above 2.55 m have relatively low χ_0 and decreasing χ_{ARM} (corresponding to increasing stratigraphic height and grain size) and are inferred to exhibit pseudo-single domain (PSD) behavior. Samples from each stratigraphic height cluster tightly in discrete, and largely unique, areas on the plot, which reflects the narrowness of the grain size distribution at each stratigraphic level.

Hysteresis results (Figure 2.3c) for most samples from the lower 1.0 m of the unit are characterized by low ratios of saturation remanence, M_{rs}, to M_s ($M_{rs}/M_s < 0.1$), low coercivity, B_c ($B_c < 10$ mT), and relatively high coercivity of remanence, B_{cr} (Figure 2.3b), which is typical of SP particles with some admixture of larger particles. There is some variation in M_s values, but the variation is not a function of height (Figure 2.3d). The scatter in M_s likely represents heterogeneity in magnetite concentrations due to varying proportions of pumice or lithic fragments on the scale of the specimen size. Within the lowest 0.80 m of the section, there is a small but distinct decrease in both M_{rs}/M_s and B_c, resulting in minimum values that spatially coincide with the peak in χ_0. M_{rs}/M_s and B_c increase with height up to what is probably the location of the upper limit for stable SD behavior in the unit, near the peak in χ_{ARM}, and both values decrease above 4.0 m, as expected for PSD-sized grains. Hysteresis parameters viewed in the form of a M_{rs}/M_s vs. B_{cr}/B_c plot (Day et al., 1977) have considerably more overlap between samples (Figure 2.5b) than in the χ_0 vs. χ_{ARM} plot, as the changes in hysteresis properties are less pronounced than those in χ_0. Additionally, on the M_{rs}/M_s

vs. B_{cr}/B_c plot, several samples from non-adjacent layers occur in similar positions and the boundaries between regions dominated by different magnetic domain states are not as clearly delineated.

2.4 Discussion

It is important to note that for samples inferred to contain grains in the SD region, the general trend with increasing stratigraphic height (and thus increasing grain size) in Figure 2.5a is for the line connecting each point with the origin to have steeper slopes for increasingly coarse grains. The opposite trend was suggested by King et al. (1982) for grains in the SD to MD range, where steeper slopes are associated with increasingly fine grains. King et al. (1982) also cautioned that narrow size distributions of SP and MD grains would look similar on this plot, and could be a source of ambiguity in determining relative grain size if both grain size fractions were present in a set of samples. Another complicating factor noted by King et al. (1982) is that both χ_0 and χ_{ARM} are affected by grain-shape anisotropy, where increasing shape anisotropy shifts χ_0 to lower values and χ_{ARM} to higher values (Stacey & Banerjee, 1974). The aspect ratios measured by Schlinger et al. (1991) (Figure 2.1b) and observed in this study indicate increasing particle elongation with particle volume, and therefore the trends with stratigraphic height in Figure 2.5a may be slightly different for particles with constant shape anisotropy, or with less elongation.

Magnetic properties of samples in the current study are compared with previously reported values for various sized magnetites in Figure 2.6. The mean magnetite concentration in our samples was approximated by taking the average M_s value for all measured samples and assuming a saturation magnetization value of 80 Am^2/kg for magnetite with a TM10 composition (Hunt et al., 1995b), which results in an estimated mean concentration of 0.28 wt% magnetite for all samples. This value was used to normalize bulk magnetic susceptibility and χ_{ARM} values for comparison with values for pure magnetite samples. Because the magnetic particles in the Tiva Canyon Tuff are variably elongated while most studies of synthetic magnetite involve cubic or equant particles, magnetic properties are plotted as a function of grain volume.

The lower SD grain volume threshold delineated by a peak in χ_0 occurs at a

slightly lower grain volume in the Tiva Canyon samples than in the synthetic magnetites measured by Maher (1988) (Figure 2.6a). This is in agreement with calculations by Butler & Banerjee (1975) and Muxworthy & Williams (2009), which predict magnetic blocking volumes for magnetite with aspect ratios of 0.3-0.4 to be slightly lower than for equidimensional magnetite. Bulk magnetic susceptibility in our samples is also notably higher than reported values for synthetic magnetites over the lowest size range, presumably due to interaction effects in incompletely dispersed synthetic samples. This was also suggested by Worm & Jackson (1999), who noted that the χ_0 values measured by Maher (1988) were well below the theoretically predicted values. Data for B_c and B_{cr} are more scattered (Figure 2.6c,d), although our data appear to be roughly consistent with the pattern of size-dependence seen in several synthetic sample sets.

χ_{ARM} reaches a maximum at slightly higher particle volumes than most synthetic magnetites shown in Figure 2.6b, although the χ_{ARM} reported for whole cells of magnetotactic bacteria containing elongate chains of SD magnetite by Moskowitz et al. (1988) is slightly higher than for any of our samples. As with χ_0, the higher χ_{ARM} values in our samples may be attributed to the absence of interactions effects, although the rough normalization performed on the data may also account for some of the discrepancy.

Model calculations indicate that the SD size range is extended to larger volumes with higher particle elongation, which predicts an upper SD size limit at particle lengths over 1 μm for an aspect ratio of 0.1 (Butler & Banerjee, 1975; Muxworthy & Williams, 2009). However, while the peak in χ_{ARM} almost certainly marks the upper limit of SD behavior in the section studied here, it is unclear whether this change in domain state is due to a particle volume threshold in independent elongated grains, or whether it simply marks a transition to inhomogeneous nucleation of magnetite grains in the studied section (Figure 2.2). Intergrowths of magnetite that produce larger effective particle volumes may cease to exhibit SD behavior. The decreases in M_{rs}/M_s and B_c above 3.25 m also suggest PSD or metastable SD behavior. Since ARM is known to be especially sensitive to even weak interactions (Egli, 2006), the clustered and intergrown magnetite observed here (Figure 2.2) and by Schlinger et al. (1991) in the upper part of the section suggest that the sharp drop in χ_{ARM} may reflect the presence of magnetostatic interactions.

If we conversely assume that the non-SD characteristics in samples above 3.25

m are attributed to isolated magnetite particles, the transition in magnetic properties at that height might indicate that transdomain or local energy minima (LEM) domain states become dominant in individual particles in the upper part of the section. Micromagnetic modeling by Fabian et al. (1996) indicates that LEM states exist in elongated magnetite at smaller particle lengths than those predicted as the upper SD limit by the Butler & Banerjee (1975) model. Dunlop et al. (1994) also predicted multiple possible domain states, including LEM states, between grain lengths of 140 and 500 nm for magnetite with an aspect ratio of 0.67 at room temperature, although neither of the models mentioned above include grains with elongations as extreme as those in our uppermost samples. To our knowledge, there are not sufficient data on highly elongated magnetite covering a broad range of sizes or volumes to know precisely where the limit of stable SD behavior lies in elongated grains.

2.5 Conclusions

The data presented here demonstrate the degree of variation in rock magnetic properties for populations of dispersed, non-interacting magnetic particles with uniaxial anisotropy and narrow grain-size distributions covering the span of SP and small SD domain ranges. Magnetic particle volumes increase progressively upward above the base of the unit. In the lowermost 2.5 m of the unit, mean particle volumes increase exponentially with height from $\sim$500 nm^3 to $\sim$100,000 nm^3. Particle size continues to increase upward over the lowermost 5 m of the unit, with magnetic properties indicating a SP-SD threshold at about 0.8 m and a transition away from stable SD behavior at 3.25 m. For these samples, plotting χ_0 vs. χ_{ARM} provides a clear indication of relative magnetic grain size, while domain regions and differences in grain size are less easily distinguished on a plot of hysteresis parameter ratios. The samples studied here afford unique insight into the size-dependent behavior of fine magnetic particle assemblages.

Table 2.1: Sampling information for the studied specimens.

Sample	Height above base (m)	Magnetic particle length (nm)[a]	Aspect ratio[a]	Magnetic particle volume (nm^3)	Sample type	Number of samples
TC04-005	0.05	15	0.36	$4.4x10^2$	Drill cores	4
TC04-012	0.12	18	0.28	$4.6x10^2$	Drill cores	5
TC04-030	0.3	-	-	-	Drill cores	3
TC04-050	0.5	37	0.2	$2.0x10^3$	Drill cores	8
TC04-075a	0.75	-	-	-	Drill cores	10
TC04-075b	0.75	-	-	-	Drill cores	52
TC04-080	0.8	-	-	-	Drill cores	2
TC04-110	1.1	50	0.17	$3.6x10^3$	Drill cores	3
TC04-140	1.4	85	0.11	$7.4x10^3$	Drill cores	2
TC04-170	1.7	-	-	-	Hand sample	1
TC04-175	1.75	100	0.13	$1.7x10^4$	Hand sample	1
TC04-255	2.55	250	0.1	$1.6x10^5$	Hand sample	1
TC04-325	3.25	-	-	-	Drill cores	2
TC04-395	3.95	$\sim$500	-	-	Drill cores	2
TC04-455	4.55	-	-	-	Drill cores	2
TC04-502	5.02	$\sim$1000	-	-	Hand sample	1

[a]Magnetic particle dimensions are from TEM measurements by Schlinger et al. (1991).

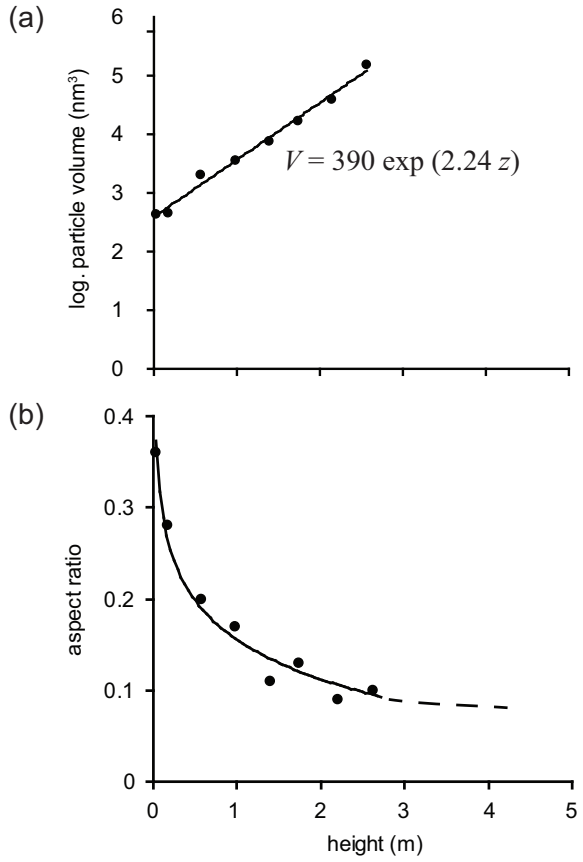

Figure 2.1: Changes in magnetic particle size and shape as a function of height as reported by Schlinger et al. (1991). (a) Calculated grain volumes for magnetic microcrystals from TEM measurements, which have a nearly logarithmic growth trend. (b) Changes in magnetic particle aspect ratio (length/width) with sample height.

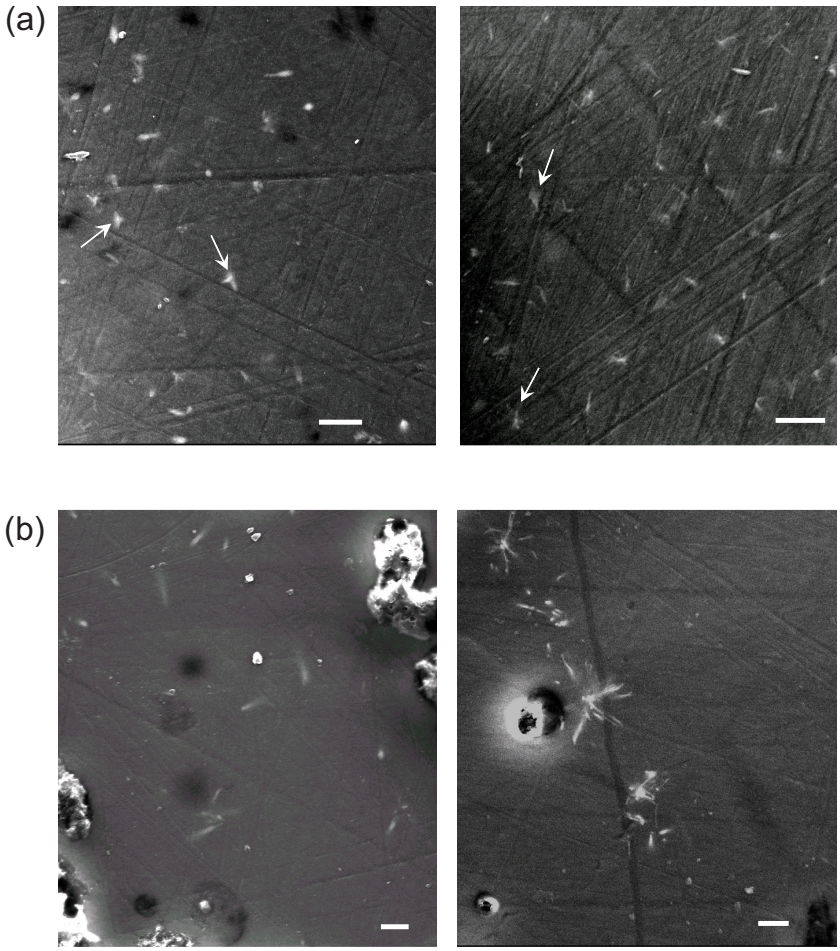

Figure 2.2: Scanning electron microscope images of Fe-oxides (elongated bright phases) in glass in samples from near the top of the sampled section, showing continuation of the growth trend indicated by Schlinger et al. (1991). White scale bars represent 1 μm in each image. (a) Sample TC04-395 has mostly dispersed elongated magnetite grains with an average length around 0.5 μm, with occasionally intersecting grains (arrows). (b) Sample TC04-502 contains magnetite grains around 1 μm in length, some of which occur as dispersed particles (left), but most of which occur in tangles of intergrown particles (right).

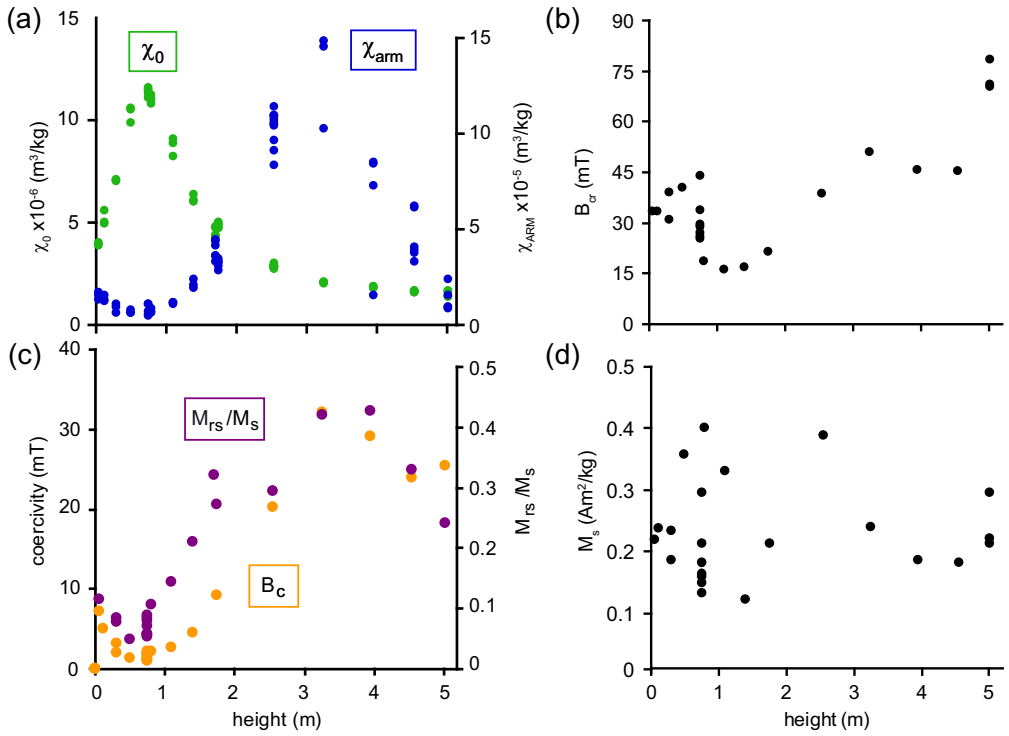

Figure 2.3: Variation in magnetic properties with sample height. (a) Variation in bulk and anhysteretic susceptibilities throughout the sampled section, (b) coercivity of remanence, B_{cr}, (c) variation in remanence ratio, M_{rs}/M_s, and coercivity, B_c, for representative samples, and (d) variation in saturation magnetization, M_s.

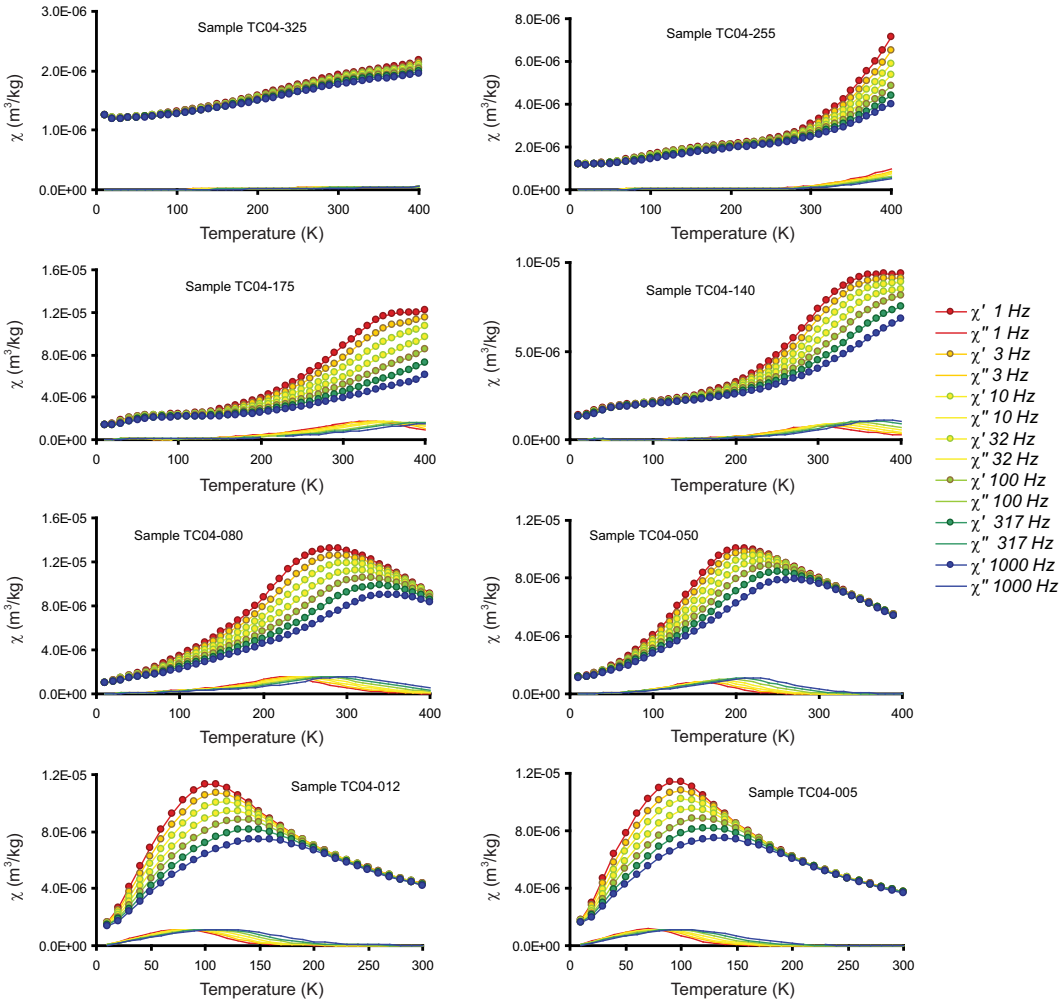

Figure 2.4: Low-temperature frequency-dependence of AC susceptibility for selected samples. Out-of-phase (quadrature) susceptibility is indicated with plain solid lines with colors corresponding to the frequencies indicated in the legend. Note the shorter temperature scale in the two lowermost plots.

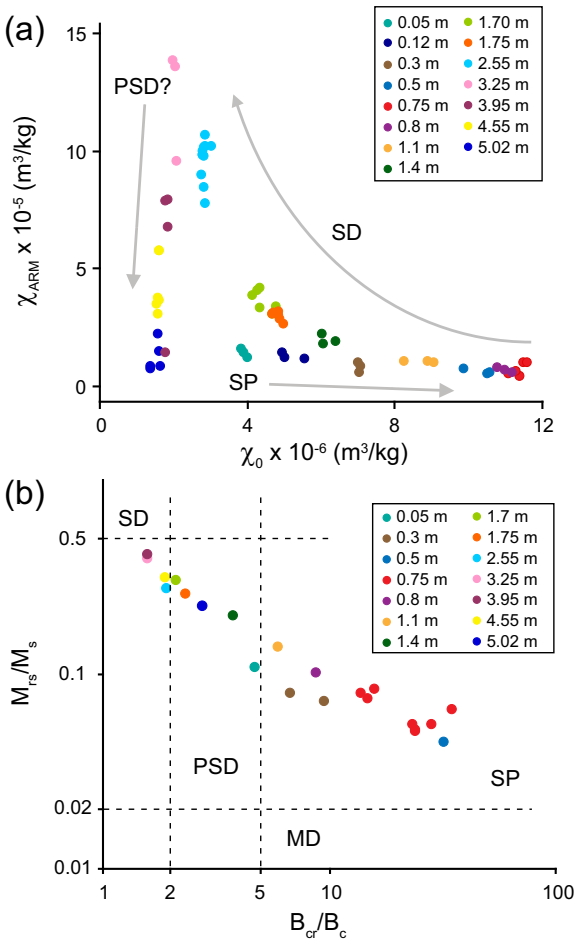

Figure 2.5: Comparison of bivariate plots for determination of relative magnetic grain size. (a) χ_0 vs. χ_{ARM} after King et al. (1982). Distinct peaks occur along each axis at domain state thresholds. (b) Hysteresis parameters plotted after Day et al. (1977) have variable hysteresis properties, but some overlap occurs between samples with dissimilar magnetic grain size. Boundaries between different domain state regions are drawn after Dunlop (2002).

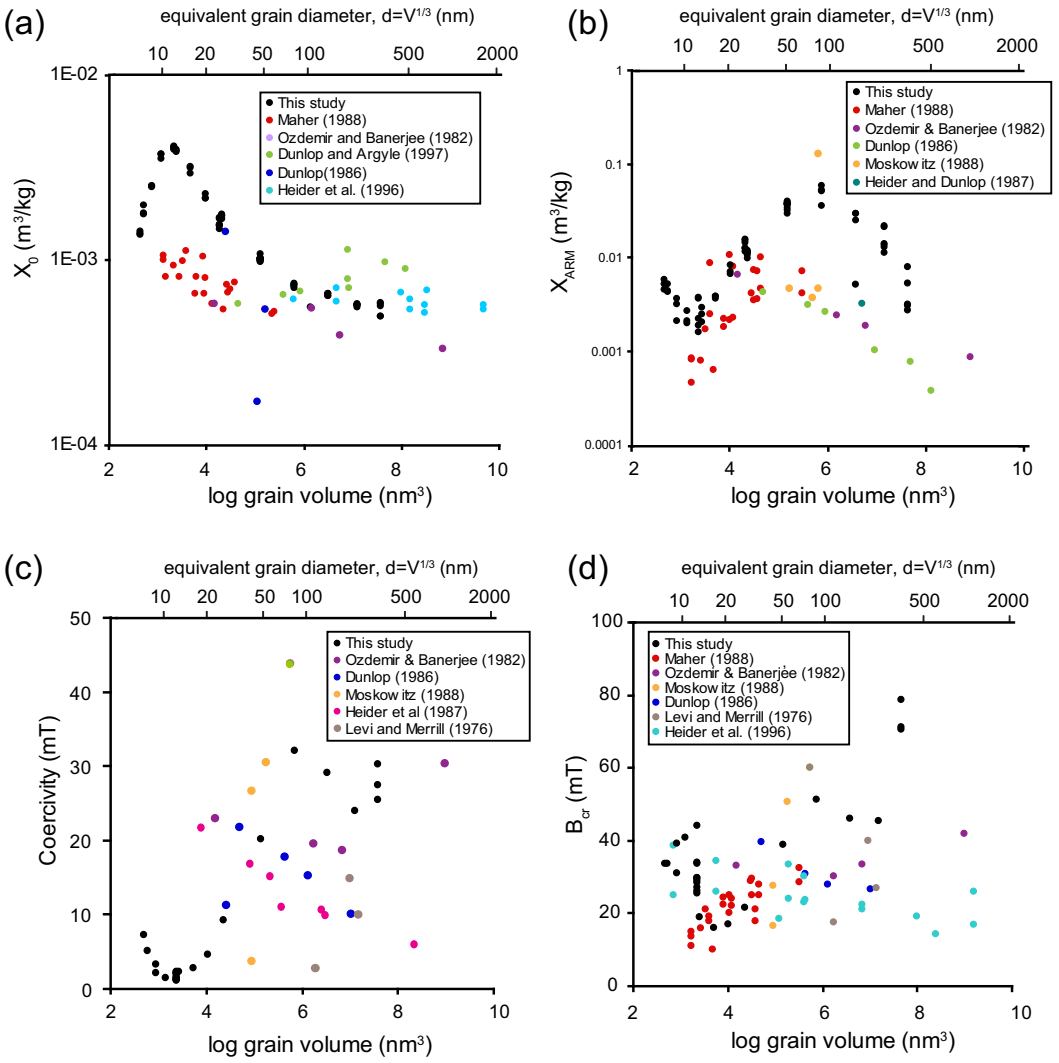

Figure 2.6: A comparison of fundamental magnetic properties as a function of inferred grain volume for the Tiva Canyon Tuff and reported values for magnetites of known size from Levi & Merrill (1976); Özdemir & Banerjee (1982); Dunlop (1986); Maher (1988); Moskowitz et al. (1988); Heider et al. (1987); Heider & Dunlop (1987); Heider et al. (1996), and Dunlop & Argyle (1997). Grain volumes for samples in the current study were interpolated using the equation shown in Figure 2.1a.

Chapter 3

Fe Diffusion in Plagioclase and Time Scales of Fe-oxide Exsolution

The chemical diffusion of Fe in natural single crystals of intermediate plagioclase has been measured at temperatures between 900 and 1200°C at controlled oxygen fugacity. Thin films of metallic Fe on oriented crystal surfaces were annealed for durations between 4 h and 4 days, and the resulting diffusion profiles were analyzed with Rutherford backscattering spectrometry. The analysis indicates that Fe diffusion follows an Arrhenius relation in the form:

$$D = 3.12x10^{-5}exp(-356.3kJ/mol/RT)m^2/s$$

for oxygen fugacities at the quartz-fayalite-magnetite buffer and

$$D = 5.51x10^{-6}exp(-350.6kJ/mol/RT)m^2/s$$

for heating in air. Diffusion rates measured over a range of oxygen fugacities show a negative dependence of D on f_{O_2}. A comparison of diffusivities parallel to [100], [010], and [001] directions indicate no diffusional anisotropy of Fe in plagioclase. Plagioclase samples that were pre-annealed for 24 h in air prior to thin film deposition systematically show slightly lower diffusivities than samples that received no pre-treatment. Water-enhanced diffusivity may be responsible for faster rates and a lower apparent activation

energy in samples that were not pre-annealed. Fe diffusion in the samples is accompanied by interdiffusion of Al and Ca. Previous measurements of Fe self-diffusion in plagioclase are over an order of magnitude faster than our measured diffusivities. Part of this difference may be explained if Fe chemical diffusion is rate-limited by interdiffusion of slow-moving tetrahedral Al.

These diffusivities have been used to calculate theoretical time scales of diffusion-limited growth of microscopic Fe-oxide needles during exsolution from plagioclase. Time scales of particle growth depend strongly on cooling rates, with growth of sub-micron magnetite needles occurring over approximately 20 kyr for cooling rates near 10 °C/kyr, 200 kyr at rates near 1 °C/kyr, and over 1 My for cooling rates slower than 0.2 °C/kyr. The calculated exsolution rates also indicate that growth of fine magnetite particles is sufficiently rapid as to ensure the paleomagnetic reliability of such particles if nucleation occurs at high temperatures and relatively fast cooling rates, but acquisition of chemical remanence due to sub-Curie temperature growth and domain state transitions could be significant at lower nucleation temperatures and slower cooling rates.

3.1 Introduction

Studies of the earth's ancient magnetic field depend on the availability of magnetic minerals that have undergone limited or no thermal or chemical alteration since formation. Magnetic inclusions in silicate minerals are frequently found in mafic intrusive rocks and are typically thought to be the result of subsolidus exsolution during cooling based on their regular spacing and high degree of orientation in the silicate matrix. These exsolved magnetic particles are popular for use in paleomagnetic studies (Geissman et al., 1988; Yu & Dunlop, 2001; Tarduno & Cottrell, 2005; Selkin et al., 2008) and have been used to obtain estimates of the earth's earliest paleofield strength (Smirnov et al., 2003; Halls et al., 2004; Tarduno et al., 2007). The inclusions typically have single-domain (SD) magnetic structures and are thus magnetically stable over long time scales. In addition, the silicate matrix can effectively shield exsolved particles from weathering and chemical alteration processes that would degrade the paleomagnetic signal (Renne et al., 2002). It has also been suggested that exsolved Fe-oxides in plagioclase are the

dominant remanence carriers in oceanic gabbros, and these may be responsible for significant contributions of the lower oceanic crust to marine magnetic anomalies (Davis, 1981; Gee & Kent, 2007).

Despite the paleomagnetic significance of exsolved Fe-oxide particles in plagioclase, the conditions of exsolution and durations of particle growth are poorly known and virtually no experimental chemical data exist on the low-T solubility of Fe in plagioclase. Nonetheless, paleomagnetic studies typically assume that such inclusions form well above the Curie temperature of magnetite (T=580°C). However, if exsolution occurs at lower temperatures than are usually assumed (T>700°C) or if the time scale of Fe-oxide growth is long relative to changes in the earth's magnetic field, then the remanent magnetization recorded by the inclusions is not simply acquired from cooling in the earth's field at a specific moment in time and the paleomagnetic interpretation is necessarily more complex.

With further study, the presence and character of exsolved Fe-oxides that give plagioclase a "dusty" or dark-clouded appearance has potential to be used as an important petrologic indicator if a trace-element geothermometer can be established as it has been for other mineral systems (Kohler & Brey, 1990; Zack et al., 2004; Wark & Watson, 2006; Hayden et al., 2008). In addition, careful calibration of exsolution textures in other silicates have formed the basis of geospeedometers from which cooling-rates may be derived (Yund & Davidson, 1978; Grove, 1982; Abart et al., 2009). In order to potentially derive information about thermal history and cooling rates from oxide exsolution features in plagioclase, the growth kinetics must be well-characterized. As this growth is rate-limited by lattice diffusion, measurements of Fe diffusivity in plagioclase are necessary for a first-order determination of exsolution time scales.

We present results from a series of experiments designed to study chemical diffusion of Fe in plagioclase. These data have been used to calculate time scales of growth for theoretical needle-shaped particles during continuous cooling with the goal of placing constraints on the time and temperature conditions required for growth of Fe-oxide during exsolution in plagioclase. The model results illustrate the amount of magnetite growth possible over various time-temperature paths to highlight conditions likely to produce magnetic particles that faithfully record paleomagnetic information.

3.2 Background

Fe can be present in plagioclase as both Fe^{2+} and Fe^{3+}. While some Fe^{2+} is thought to replace Ca in M-sites in the general chemical formula for plagioclase MT_4O_8, most Fe^{2+} and all Fe^{3+} substitute for Al in tetrahedral T-sites (Longhi et al., 1976). In lunar and meteoritic rocks where all Fe in plagioclase is present in ferrous form, Fe^{2+} predominately occupies T-sites via the substitution mechanism: $Fe^{2+} + Si^{4+} \leftrightarrow 2Al^{3+}$ (Sclar & Kastelic, 1979; Beaty & Albee, 1980). Typical Fe contents in feldspar are between 0.2 and 1 wt% Fe_2O_3, although values as high as 4 wt% have been reported in natural rocks, and volcanic plagioclase typically contains about twice as much Fe as plagioclase in plutonic rocks (Smith & Brown, 1988). This may be related to the observation of Grove & Bence (1979) that plagioclase incorporates higher amounts of trace elements at faster cooling rates. Mg and Ti also occupy plagioclase T-sites in smaller quantities. Sclar & Kastelic (1979) synthesized a complete solid solution between anorthite and the Fe-rich endmember $CaFeSi_3O_8$. Partitioning of Fe^{3+} between plagioclase and silicate melts is about 20 times higher than for Fe^{2+}, implying a strong dependency of Fe content on magmatic oxygen fugacity (Wilke & Behrens, 1999; Sugawara, 2001; Lundgaard & Tegner, 2004). The strong preference for Fe^{3+} in plagioclase has led to the use of variations in Fe content as an indicator of magma chemistry and redox conditions in plutonic rocks (Lundgaard & Tegner, 2004). Although Fe contents show a wide variation as a function of plagioclase compositions, within zoned crystals the more calcic compositions are sometimes associated with higher Fe contents (Bryan, 1974), presumably because anorthite has a higher availability of sites for Fe substitution (Hofmeister & Rossman, 1984; Tegner, 1997).

The conditions that prompt Fe exsolution from feldspar are still unresolved. An idealized binary phase diagram (Figure 3.1) would indicate that plagioclase with higher Fe contents is more likely to intersect the solvus during cooling from high temperature than material with a lower initial Fe concentration. However, some studies have observed that the bulk chemistry of clouded plagioclase, including total Fe contents, is nearly identical to unclouded plagioclase in the same geologic settings (Armbrustmacher & Banks, 1974). These observations hint at the possibility that Fe miscibility depends on more than just temperature and Fe concentration. A number of older studies have

suggested that high water contents are associated with exsolved Fe-oxides in plagioclase (Poldervaart & Gilkey, 1954; Burns, 1966; Bridgwater & Harry, 1968; Boone, 1969) and alkali feldspar (Putnis et al., 2007) based on associated hydrous minerals and correlations of bulk rock water content with clouding intensity. Bridgwater & Harry (1968) inferred the presence of almost 0.25 wt% H_2O in clouded plagioclase by thermogravimetric measurements that showed loss of mass after heating to moderate temperatures. However, Smith & Brown (1988) point out that exsolved Fe-rich phases also occur in plagioclase in meteorites and lunar anorthosites in the absence of water. Halls et al. (2007) theorized that reducing CO_2-rich fluids were responsible for the formation of clouded plagioclase in meta dolerite dykes. The presence of exsolved metallic Fe in lunar and meteoritic plagioclase also requires the reduction of Fe^{2+} (Sclar, 1979; Harlow & Klimentidis, 1980). Plagioclase that has experienced high-grade metamorphism and recrystallization tends to be unclouded with low Fe content (Burns, 1966).

3.3 Experimental Methods

3.3.1 Sample Preparation

Several large single crystals of plagioclase feldspar from Ethiopia, each approximately 15 mm in diameter, were used for the diffusion experiments. The composition of this plagioclase was determined quantitatively with electron microprobe analysis (Table 6.1), and has an anorthite composition of An_{57} and a starting Fe content of nearly 0.4 wt%. These grains are optically transparent and are slightly yellow in color. Electron backscatter diffraction (EBSD) was used to orient the crystals so that they could be cut along surfaces perpendicular to the [100], [010] and [001] crystallographic directions. After oriented surfaces were produced, several parallel slices approximately 1 mm thick were made and polished on one side with progressively finer grades of diamond lapping films and given a final polish with a colloidal silica suspension. The slight chemical etching effect of the colloidal silica is effective at removing residual mechanical stresses on the sample surface introduced by polishing. Profiles of sample surfaces made using an atomic force microscope indicate that the surface roughness of these samples is less than 2 nm. After polishing, EBSD point analyses were performed again on each sample to check that the orientation was maintained during polishing, which was within 5° of the

principal crystallographic directions. EBSD maps over a large sample area were made on a subset of samples, and the maps indicate that the sample orientations are uniform, and that twinning and other microstructures are absent in the single crystals.

Thin films of metallic Fe of thickness 12.5 nm were deposited on the surface of polished plagioclase slabs. The thin films were synthesized either by sputtering or by physical vapor deposition in the NanoFabrication Center at the University of Minnesota. To ensure a good contact between the thin film and the substrate, the slabs of feldspar prepared for thin film vapor deposition were pre-annealed in air for 24 hours at 1200°C after polishing, which helped to further remove any surface damage from the polishing process by annealing. Feldspar samples used with sputtering received no pre-treatment prior to thin film deposition because the high energy with which Fe particles are deposited during the sputtering process produces a very robust contact between the two phases. Fe films are presumed to be polycrystalline and to have no epitaxial relationship with the plagioclase.

3.3.2 Experiment Procedures

Diffusion anneals were performed at temperatures between 900-1200°C for durations ranging from several hours to several days in a horizontal gas-mixing tube furnace. Samples were placed in porous ceramic crucibles in the furnace. Two series of experiments were performed over this range of temperatures either in air or at a controlled oxygen fugacity of one log-unit above the quartz-fayalite-magnetite (QFM) buffer, produced by an atmosphere of flowing CO-CO_2 which was mixed in precise proportions using digitally-controlled gas flow meters. Samples oriented for diffusion along [100], [010] and [001] were annealed in the same heating runs to determine if any diffusional anisotropy exists for Fe. Additionally, a series of experiments was conducted over a range of oxygen fugacities between QFM+0.5 and QFM+2 (log f_{O_2} between -11 and -9) at 1000°C on samples oriented for diffusion parallel to [010] to investigate the f_{O_2}-dependence of Fe diffusion.

Post-annealing composition profiles as a function of depth were obtained using Rutherford backscatter spectrometry (RBS) on the ion beam analysis system located in the Characterization Facility at the University of Minnesota. RBS is a quantitative near-surface analysis technique whereby a sample is bombarded with He^+ ions which, when

backscattered, produce a spectrum with energies characteristic of both the mass and the depth of the scattering atoms in a sample. Small changes in energy in the spectrum correspond to energy loss of incident ions with increasing depth into the sample, while large differences in energy are due to atomic number contrast (Figure 3.2), which can be combined to determine composition as a function of depth up to 1-2 microns below the sample surface. All RBS work for this study was performed on a NEC MAS 1700 pelletron tandem ion accelerator (5SDH). This system has a nominal detector energy resolution of 12 keV. Incident ion beam energies of 2.0 MeV were used, with a total collected charge of 60 microcoulombs for each sample.

3.3.3 RBS Analysis

Example RBS spectra are shown in Figure 3.2a for an Fe thin film on a plagioclase substrate before annealing, and two samples after annealing at different temperatures. Steep edges in the spectra correspond to the maximum backscattering energies for each constituent element at the sample surface. The height of the Fe peak is proportional to the concentration of Fe at the sample surface and the sloping back edge of the Fe peak is related to the gradient in Fe concentration with depth into the sample.

The resulting post-annealing RBS spectra were analyzed with the RUMP software (Doolittle, 1985). The Fe peaks in the measured spectra were compared with a simulated spectrum based on a theoretical composition *vs.* depth model. This model composition was varied by an automatic routine to find the depth distribution of Fe that provided the statistical best fit to the measured data. This solution was then refined by adjusting the composition of individual depth layers to achieve a better fit between the simulated and the measured spectrum. It is assumed that the Fe layer immediately dissolves into the substrate, that diffusion occurs perpendicular to the sample surface and that diffusion is independent of Fe concentration. For diffusion in 1-dimension, the Fe concentration as a function of time and depth is given by the solution to the diffusion equation (Crank, 1975) for a thin film:

$$C(x) = \frac{M}{\sqrt{\pi Dt}} exp(\frac{-x^2}{4Dt}) \tag{3.1}$$

where M is the total amount of diffusant initially present in the thin layer, $C(x)$ is the concentration of Fe with depth x below the sample surface, D is the Fe diffusivity, and

t is annealing time. This equation describes the concentration gradient of the solute as a function of annealing time and distance below the sample surface. The data were plotted in the form of a ln$C$ *vs.* x^2 plot, which produces a line with slope $-1/(4Dt)$, from which D may be easily obtained.

3.4 Diffusion Results

An example of a typical post-annealing depth profile of Fe concentration is shown in Figure 3.3a alongside a plot of the same data inverted through Equation 3.1 (Figure 3.3b). Measured diffusivities for all experiments are listed in Table 3.2. Diffusion profile lengths typically fall in the range of 100-600 nm.

Diffusion coefficients are obtained from a plot of log D versus $10^4/T$, in which the data define an Arrhenius relation of the form $D = D_0 exp(-E_a/kT)$ where k is the Boltzmann constant. Diffusion coefficients for Fe in samples annealed in air give an activation energy E_a of 350.6 kJ/mol and a pre-exponential term, D_0 = 5.51x10^{-6} m^2/s. However, some systematic discrepancies in this series of experiments were noted, as described below. Diffusion in experiments at QFM+1 is somewhat faster than in air, and follows an Arrhenius relation with E_a=356.3 kJ/mol and D_0=3.12x10^{-5} m^2/s (Figure 3.4a).

No dependence on crystallographic direction is seen in the data, indicating little evidence for diffusional anisotropy of Fe (Figure 3.4b). Although, because variations in diffusion rates due to anisotropy are typically less than an order of magnitude, the anisotropy may be less than the resolution of our experiments. Upon close comparison of post-annealing RBS spectra with a pre-annealing spectrum for plagioclase, it can be seen that the near-surface edges of both Ca and Al become less sharp, indicating concentration gradients that have developed in response to the interdiffusion of both of these elements with Fe (Figure 3.2b). Since no diffusional anisotropy is detectible from the experiments, the scatter in data points for each annealing run may be taken as a rough measure of experimental error. However, future work is planned to calculate quantitative errors as a function of particle yields and depth uncertainly directly from the RBS data.

3.4.1 Comparison with Previous Studies

A clear but weak negative dependence on f_{O_2} is seen in experiments with varied oxygen fugacities (Figure 3.4c). The variation in D is less than half an order of magnitude over the studied f_{O_2} range. Behrens et al. (1990) measured tracer diffusion of Fe isotopes in An_{62} labradorite as a function of oxygen fugacity at 1200°C. Although no rate law was determined in these experiments, the wide range of f_{O_2} values used in that study provide an indication of the magnitude of difference between Fe^{2+} and Fe^{3+} diffusivities. The range of diffusion values measured by Behrens et al. (1990) are indicated in Figure 3.5. The Fe diffusivities measured in that study at high f_{O_2} and at 1200°C are approximately an order of magnitude faster than our measured diffusion rates for samples heated in air.

Part of this difference may lie in the fact that our experiments measure Fe chemical diffusion, which involves a net change in concentration of the diffusant in the sample, whereas Behrens et al. (1990) measured tracer diffusion as a proxy for Fe self-diffusion, where a specific isotope of a diffusing element is exchanged for atoms of the same element already present in the sample, with no net change in concentration. Cherniak (2010) reported that measured Sr self-diffusion rates differed significantly from measurements of Sr chemical diffusion in plagioclase. This paper further notes that self-diffusion may be faster than chemical diffusion if interdiffusion of a slow-moving species, such as tetrahedral Al in feldspar, is required for chemical diffusion to take place, which may be the case for Sr diffusion in feldspar, and is almost certainly also true for Fe in our experiments. For the purpose of understanding exsolution processes in plagioclase, the relevant quantity is the chemical diffusivity, since diffusion-limited particle growth is accompanied by local changes in concentration.

3.4.2 Possible Diffusion Enhancement by Water

Samples in a handful of experiments performed in air (D01 through D05) have noticeably higher diffusivities than samples heated in air at the low end of the temperature range and show considerable overlap with samples annealed at lower oxygen fugacities (red symbols in Figure 3.4). The samples from these experiments are distinguished from the others by the fact that the Fe films were synthesized by sputtering and that the samples

received no thermal pre-treatment prior to the diffusion anneals. On an Arrhenius plot, the samples that were not pre-annealed define a line with a lower activation energy, with a rate law in the form $D = 4.59x10^{-10}exp(-240.3kJ/mol/RT)$ m^2/s. A possible explanation for this difference is that the pre-annealing that was performed on all other samples released trace amounts of hydrogen from the plagioclase lattice, and these samples exhibit diffusion in truly dry material. Samples that were not pre-annealed may retain trace amounts of water and thus exhibit enhanced diffusivities due to the presence of hydrogen.

Yund & Snow (1989) observed enhanced rates of CaAl-NaSi interdiffusion under controlled water fugacities compared to dry conditions (Yund, 1986). In addition, a lower activation energy was observed for CaAl-NaSi interdiffusion under hydrothermal conditions. However Na-K interdiffusion experiments in feldspar showed no change in the presence of water (Christoffersen et al., 1983). Cherniak (2010) suggests that the presence of water (here meant to indicate either structural H_20 or OH groups in the feldspar lattice) can enhance diffusion of tetrahedral cations in feldspar, but that it seems to have little effect on alkali cation movement. Since both Fe^{2+} and Fe^{3+} are believed to substitute for Al on tetrahedral sites, diffusion of Fe in plagioclase can reasonably be expected to show a similar enhancement due to the presence of water. Future work will try to detect water in our plagioclase samples by checking for measurable loss of mass on heating.

In a NaSi-CaAl interdiffusion study, Yund & Snow (1989) determined that heating 3.5 mm-wide cores of peristerite feldspar at 800°C for 12 hours at high confining pressure was sufficient to allow an equilibrium concentration of hydrogen to diffuse into the samples. It is probable then that the pre-annealing treatment performed before our diffusion anneals would allow sufficient time for residual hydrogen to diffuse out of the samples if it was present. Alternatively, other volatile impurities such as F^- have been shown to enhance rates and lower the activation energy of alkali interdiffusion in feldspar (Snow & Kidman, 1991). The large size of the single plagioclase crystals used in the experiments and the lack of zoning or other chemical or physical microstructure suggests a pegmatite origin, which has been associated with high concentrations of hydrous species in feldspar (Smith & Brown, 1988; Johnson, 2006).

3.5 Exsolution Model

Cherniak et al. (2007) used measured diffusivities of Ti in quartz combined with data on solubility of Ti in quartz as a function of temperature to model the growth of rutile needles in quartz over various time-temperature paths. Fe diffusion data can be applied similarly in plagioclase with some limitations. Data for Fe solubility in plagioclase as a systematic function of temperature are not presently available. However we may make simple assumptions about the range of likely nucleation temperatures and initial Fe contents in plagioclase prior to exsolution to calculate time scales of Fe-oxide exsolution and particle growth rates. Since magnetite is typically observed in the form of dispersed, oriented needles in plagioclase (Feinberg et al., 2005), we used a modified version of the model described in Cherniak et al. (2007), kindly provided by Prof. Bruce Watson. This model calculates the growth of a magnetite needle of arbitrary length due to two-dimensional radial diffusion of Fe in plagioclase during continuous cooling.

The calculations use a numerical finite difference solution to Fick's 1st law which describes the rate of flux of a solute (Fe) in response to a concentration gradient:

$$J = -D\frac{\delta C}{\delta x} \tag{3.2}$$

where J is the flux of Fe per unit area per unit time, D is the Fe diffusivity, and C is Fe concentration in the matrix per unit volume which varies over a distance x. The plagioclase matrix surrounding a "seed" particle of 1 nm-wide magnetite is divided into concentric cylindrical rings through which flux is calculated for each timestep, and the Fe concentration in each ring is incrementally decreased according to the steepness of the concentration gradient. As the needle diameter increases, the interface between the particle and matrix moves outward, the boundaries between the imaginary cylinders are repositioned and the diffusion profile is adjusted to account for the moving boundary. Given the strong suggestions that water is frequently associated with dark-clouded plagioclase, the scaled diffusion rates for samples interpreted as showing water-enhanced behavior were considered more appropriate for the model and the rate law with the lower activation energy was used.

Currently, no quantitative constraints on magnetite nucleation temperatures in plagioclase exist, although Armbrustmacher & Banks (1974) estimated that exsolution of Fe-oxides in plagioclase in metadolerite dikes took place below 475°C. The presence

of Fe-Ti oxide needles in some plagioclase that have further exsolved into finer lamellae of magnetite and ulvospinel (Feinberg et al., 2005) constrains oxide nucleation in those rocks to temperatures above the magnetite-ulvospinel solvus, which is probably located between 500° and 600°C (Lindsley, 1991). Here we have considered nucleation temperatures between 550 and 750 °C. Calculations of particle growth with nucleation temperatures below 550°C resulted in particles less than 20 nm wide for cooling rates as low as 0.1 °C/ky. Particles of arbitrary length with widths less than 20 nm may exist in a superparamagnetic state at room temperature and will not necessarily hold a stable remanence, so nucleation temperatures below 550°C are not considered here. Nucleation temperatures are represented by color in Figures 3.6 and 3.7. Needles were assumed to nucleate with an arbitrary length of 1 μm. In all model scenarios, particle growth effectively ceases at approximately 450°C during cooling. Particle growth paths as a function of temperature are shown for various nucleation temperatures and cooling rates in Figure 3.8a.

Measured Fe contents in plagioclase can vary substantially, and some studies have indicated that plagioclase containing exsolved Fe-oxides can contain equal or lesser amounts of Fe than plagioclase grains with no exsolution. The effect of initial Fe content when varied from 0.4-1.0 wt% on exsolved particle size is shown in Figure 3.6b. The low-temperature solubility of Fe is assumed to be 0.2 wt%. Most calculations used a starting Fe content of 0.8 wt% ($\approx$1 wt% FeO). Particle growth for plagioclase containing 0.4 wt% Fe is roughly half of that calculated for an Fe content of 0.8 wt% under the same cooling conditions.

Calculated time scales for the growth of magnetite needles are overwhelmingly dominated by the cooling rate (Figure 3.7a). Here we have considered cooling rates in the range 0.1-10 °C/ky. Time scales of growth vary from as little as 20 ky at the highest cooling rates, to over 1000 ky for the slowest rates. Cooling rate estimates for lower crustal gabbros in the Oman ophiolite by Coogan et al. (2002) based on geospeedometry are between 0.1°/ky and 1000 °/ky, depending on input dataset, with slower cooling rates at greater crustal depths. The modeled cooling rates considered here cover most of this range and should be applicable to the exsolution of magnetite in oceanic gabbros if the cooling rates determined for ophiolitic gabbros by geospeedometry applies equally to the lower oceanic crust. However, continental plutons may cool even more slowly, at

rates on the order of 1°C/My, and for such rocks the final size of magnetite particles may exceed what is shown here for a given temperature. For the above range of cooling rates, magnetite particle sizes are shown in Figure 3.6a.

A characteristic diffusion length L_D was determined for various nucleation temperatures and cooling rates using the relation:

$$L_D = \sqrt{4Dt} \tag{3.3}$$

where D is the diffusivity of Fe at the temperature of nucleation and t is the characteristic time for exsolution, which is taken as the total time for particle growth and is primarily a function of cooling rate (Figure 3.7c). If nucleating particles are in diffusive communication at the time of formation, the average spacing between nucleating particles should correspond to approximately twice the characteristic diffusion length at the nucleation temperature. The calculated characteristic diffusion lengths in Figure 3.7a correspond very well to the lengths of the modeled diffusion profiles around theoretical Fe-oxide needles, examples of which are shown in Figure 3.8b. A comparison between final particle width and characteristic diffusion lengths (Figure 3.7b) shows that L_D is consistently about 30 times the particle width, d. This means that a particle growing along a particular time-temperature path does not have a unique set of L_D and d values. Thus, the size and spacing of exsolved particles in a natural rock could only provide information about nucleation temperatures *or* cooling rates if one of these quantities is already known. The potential development of a geospeedometer from dark-clouded plagioclase then relies on the future establishment of a robust solution model for Fe in plagioclase.

3.6 Discussion

Fe diffusivity is slow compared to monovalent and divalent cations in labradorite, but fast with respect to Si. Although no data are available for Al diffusion in plagioclase, Cherniak (2003) reports that NaSi-CaAl interdiffusion rates are slower than Si self diffusion in labradorite, but faster than Si in anorthite, indicating that Al^{3+} is likely to be slow in the intermediate composition studied here, and is likely to be the rate-limiting species for diffusive processes involving chemical diffusion of Fe. Despite some indication

that the majority of both Fe^{2+} and Fe^{3+} ions sit on tetrahedral Al sites, (Longhi et al., 1976; Sclar, 1979), RBS spectra from our experiments show replacement of both Al and Ca, indicating at least partial Ca-site occupancy by Fe^{2+}. We note that during exsolution, the removal of Fe from the plagioclase lattice requires the formation of a silica-rich phase to maintain stoichiometry, for example in the Fe-rich end-member equivalent of anorthite:

$$(Fe^{2+})(Fe^{3+})_2Si_2O_8 \rightarrow Fe_3O_4 + 2SiO_2$$

If Ti substitutes for Si, exsolution of Fe-Ti-oxide can occur without formation of an additional phase. If Fe^{2+} does primarily occupy Al sites, then Fe-oxide exsolution requires the formation of a Ca-silicate phase. Sclar (1979) observed exsolved Ca-Fe-aluminosilicates in conjunction with exsolved Fe inclusions in lunar plagioclase, but no systematic study has been made of accompanying exsolved phases in terrestrial plagioclase. Identification of such phases is challenging with scanning electron microscopy methods since submicron silica-rich phases would be too small for reliable elemental analysis and would have low chemical and optical contrast with the host plagioclase.

The time scales for particle growth modeled here are applicable to exsolution occurring due to lattice diffusion by homogeneous nucleation. An exsolution mechanism involving heterogeneous nucleation on defect sites such as dislocations, subgrain boundaries, twin planes, or microfractures can take place at lower temperatures and/or shorter time scales than those shown here. Additionally, the long-term chemical stability of heterogeneously-nucleated magnetic particles cannot be assumed, since the defect sites associated with them provide potential pathways for alteration by oxidation or fluids. If water is not present in the plagioclase lattice during Fe exsolution as we have modeled it, then diffusion in dry plagioclase would shift the conditions of Fe-oxide growth to higher temperatures. As several studies have noted a connection between the presence of dark-clouded plagioclase and the presence of water, either in the source magma or as metamorphic fluids (Burns, 1966; Bridgwater & Harry, 1968), the possibility of an exsolution mechanism involving water deserves attention in future studies.

3.6.1 Implications for Paleomagnetic Studies

3.6.2 Potential for TCRM Acquisition

The most significant pitfall in choosing suitable samples for paleomagnetic studies is the lack of knowledge about the chemical and thermal history over which the magnetic particles formed. A number of physical and chemical processes can take place below the Curie temperature, T_C (=580°C for magnetite), that have the potential to alter a pure thermal remanent magnetization (TRM) into a thermo-chemical remanent magnetization (TCRM) (McClelland, 1996). Since TCRM is a less efficient recorder of field strength than TRM, paleointensity studies are most affected by this problem. Additionally, various types of TCRM can either under- or overestimate paleofield strength without producing any deviation from linearity on a paleointensity Arai plot (Draeger et al., 2006; Fabian, 2009), thus making a TCRM indistinguishable from a true TRM.

During subsolidus exsolution of Fe-oxides from plagioclase, a TCRM may in theory be acquired when superparamagnetic (SP) particles grow through a threshold volume where the magnetization of the grain becomes blocked to a stable single domain (SD) state, which would cause paleointensity determinations to be underestimated (McClelland, 1996; Fabian, 2009). The modeled growth paths shown in Figure 3.8 are for particles of arbitrary length, however, the SP blocking volume for particles of varying aspect ratios q and for relaxation times of 100 s are overlain on the particle growth curves in the figure. The upper threshold length for SP particles of aspect ratio q is given by:

$$l_{sp} = \left[\frac{12q^2kT\ln(\tau f_0)}{\mu_0 \Delta N M_s^2 \pi}\right]^{1/3} \tag{3.4}$$

where k is the Boltzmann constant, τ is the relaxation time in seconds, f_0 is the frequency factor, μ_0 is the permeability of free space, ΔN is the difference in demagnetizing factors along the short and long axes of the grain, and M_s is the saturation magnetization.

For particles with aspect ratios of 10 or higher, the SP threshold is reached rapidly during particle growth and thus acquisition of TCRM in this manner will be negligible. For nearly equidimensional particles nucleating below 600°C, the blocking contour is crossed after a substantial amount of particle growth has already taken place, and a grain growth TCRM (Fabian, 2009) will be acquired. Modeled magnetite growth paths

(Figure 3.8) show that particles nucleating at 700°C or above accomplish nearly all growth before cooling through T_C, regardless of cooling rate. Additional growth at lower temperatures will be limited by the shallow diffusion profiles surrounding these particles. Particles nucleated at sufficiently high temperatures are therefore exempt from the possibility of TCRM during exsolution.

Small SD grains that nucleate above T_C and undergo additional growth below T_C will maintain a remanence identical to the TRM acquired instantaneously upon cooling through the blocking temperature. Both the field direction and intensity recorded at the time of blocking will be retained if the particle stays within the SD size-range limits, because the new grain material should be magnetically coupled to the original grain material. Such particles probably inherit the remanence and field information of the nucleus particle. This may be the case for particles nucleating at temperatures moderately higher (600-650°C) than T_C of magnetite. SD grains that nucleate and grow below T_C have a high potential for acquiring TCRM, since the magnetization may not be acquired over the full range of the blocking temperature spectrum. This type of TCRM tends to overestimate paleointensity, although Draeger et al. (2006) found that a TCRM acquired in this manner resulted in only a minor paleointensity overestimate and that this type of TCRM was practically equivalent to a TRM. Significant growth below T_c, as low as 550°C, is possible only at slow cooling rates on the order of 0.1 °C/ky.

Magnetic Microstructure

A final mechanism of TCRM acquisition occurs when growth of SD grains below T_C crosses the maximum SD size threshold into a pseudo-single domain state (Dunlop et al., 1994; Fabian et al., 1996) through changes in grain shape and/or volume. At the point of domain wall formation or development of incoherent modes of magnetization rotation, such as fanning or vortex states, intensity information will be compromised although it is possible for directional information to be retained. This may occur for particles nucleating at moderate temperatures (600-650°C)that are capable of significant growth below T_c, restricted to relatively slow cooling rates (0.1-1°C/ky).

However, the upper size limit for pure SD behavior is poorly defined for highly

elongated magnetite particles, making it difficult to assess the potential for the trans-domain type of TCRM to occur, and thus for paleointensity information to be biased. Magnetic force microscopy work by Frandsen et al. (2004) and Feinberg et al. (2005) showed that exsolved magnetite needles with high aspect ratios and widths between 300-1000 nm in clinopyroxene contained distinct multiple domains, indicating that even highly elongated inclusions are likely to be PSD-structured at needle lengths greater than a few microns and/or needle widths of several hundred nanometers. Frandsen et al. (2004) postulated that wedge-shaped domains are energetically more favorable in needle-shaped grains than domains parallel to particle long axes due to the reduction in domain wall energy. However, there has been no systematic study of the upper SD size thresholds for highly elongated particles of more than a few microns in length. Such a study of magnetic microstructure as a function of particle dimension for exsolved Fe-oxides would greatly improve the ability of paleomagnetic studies to identify potential TCRM signatures.

Another important question related to the problem of TCRM acquisition is whether particles are more likely to grow with a constant length, in which case the aspect ratio continuously decreases, or whether particles are more likely to grow with a constant aspect ratio. Observations by Putnis (1978) of Fe-rich precipitates in rutile that maintain their aspect ratio during coarsening suggests that the latter growth mode may be more likely. Particles growing with constant length will cross the SD-PSD threshold sooner than particles growing with a constant aspect ratio. A TEM analysis of magnetite grain shape and size distribution in plagioclase by Morgan & Smith (1981) determined that grain axial ratio varied from 0.3 to 1 (equidimensional) with grain lengths between 0.08-0.48. More than half of these fall above the maximum SD threshold and in the PSD range for magnetite on a Butler-Banerjee plot (Butler & Banerjee, 1975), although the temperatures at which these grains crossed the SD-PSD transition is unknown. Magnetite needles growing with a constant aspect ratio by radial diffusion would follow a similar time-temperature path as the type of particles modeled here, but would experience slightly less growth due to slower migration of the particle-matrix interface and slightly less steep diffusion profiles. However, equidimensional particles growing with a constant aspect ratio will need to be described by a three-dimensional

diffusion geometry. Systematic mineralogical investigation of the Fe-oxide growth process during exsolution is needed to refine our calculations of growth time scales.

3.7 Summary

Fe diffusion has been measured in intermediate plagioclase and is found to be slow relative to non-tetrahedral cations. A subset of experiments indicating faster Fe diffusion may exhibit water-enhanced diffusivity, which is consistent with a significant portion of Fe having tetrahedral coordination in the plagioclase lattice. Fe diffusion data have been used to calculate first-order theoretical growth time scales of Fe-oxide needles during exsolution from a plagioclase matrix. Total growth durations are strongly controlled by cooling rates, and vary from 10 ky to 1000 ky over the range of cooling rates estimated for lower oceanic crust. Nucleation temperatures between 550°C and 750°C produce particle sizes consistent with those previously observed for naturally exsolved magnetite needles in feldspar. Experimental determinations of Fe solubility in plagioclase at subsolidus temperatures are needed to better understand the conditions that produce exsolution and to refine the time-temperature paths over which Fe-oxide particles grow. Growth of oxide particles below the Curie temperature of magnetite is possible for some cooling scenarios, but further work is needed in order to identify rocks which may contain potential chemical remanences carried by exsolved magnetite in plagioclase.

Table 3.1: Quantitative composition of plagioclase single crystals from electron microprobe measurements in wt% oxides.

oxide	wt %	atoms/8 oxygen
Na_2O	4.559	0.397
CaO	11.833	0.571
SiO_2	53.349	2.401
TiO_2	0.075	0.003
FeO[1]	0.393	0.015
MgO	0.071	0.005
K_2O	0.259	0.025
Al_2O_3	30.107	1.594
Total	100.645	5.011
An = 100 Ca/(Ca+Na+K)		57.45

[1]Total iron as FeO.

Table 3.2: Diffusion results

Run	Surface normal	Temp °C	Time (s)	D (cm^2/s)	log D	f_{O_2}	Pre-anneal
D00a	random	1100	64800	3.2787E-15	-14.48	air	no
D01	[001]	1000	108000	2.63E-16	-15.58	air	no
D02	[010]	1000	195000	9.93E-16	-15.00	air	no
	[001]	1000	195000	2.63E-16	-15.58	air	no
D03	[010]	1100	64800	3.28E-15	-14.48	air	no
D04	[100]	900	259000	9.65E-17	-16.02	air	no
	[010]	900	259000	1.35E-16	-15.87	air	no
	[001]	900	259000	9.81E-17	-16.01	air	no
D05	[100]	1200	32400	1.54E-14	-13.81	air	no
	[010]	1200	32400	1.73E-14	-13.76	air	no
D06	[100]	950	288000	900e-17	-16.05	air	yes
	[010]	950	288000	5.00e-17	-16.30	air	yes
	[001]	950	288000	7.00e-17	-16.15	air	yes
D07	[100]	1050	86400	5.79E-16	-15.24	air	yes
	[010]	1050	86400	6.43E-16	-15.19	air	yes
	[001]	1050	86400	4.91E-16	-15.31	air	yes
D08	[010]	1150	49500	8.29E-15	-14.08	air	yes
	[100]	1150	49500	7.22E-15	-14.14	air	yes
	[001]	1150	49500	1.17E-14	-13.93	air	yes
D10	[100]	900	180000	9.14E-17	-16.04	QFM+1	yes
	[010]	900	180000	8.79E-17	-16.06	QFM+1	yes
	[001]	900	180000	3.55E-17	-16.45	QFM+1	yes
D11	[010]	1050	44100	2.48E-15	-14.61	QFM+1	yes
	[001]	1050	44100	3.24E-15	-14.49	QFM+1	yes
D12	[010]	1000	86400	3.31E-16	-15.48	QFM+2	yes
D13	[100]	1200	14400	1.51E-13	-12.82	QFM+1	yes
	[010]	1200	14400	2.5E-13	-12.60	QFM+1	yes
	[001]	1200	14400	1.08E-14	-13.97	QFM+1	yes
D14	[010]	1000	72900	3.96E-16	-15.40	QFM+1.5	yes
D15	[010]	1000	54000	7.72E-16	-15.11	QFM+0.5	yes
D16	[100]	1000	64800	8.33E-16	-15.08	QFM+1	yes
	[010]	1000	64800	5.14E-16	-15.29	QFM+1	yes
	[001]	1000	64800	8.93E-16	-15.05	QFM+1	yes
D18	[100]	1150	28800	3.16E-14	-13.50	QFM+1	yes
	[010]	1150	28800	2.226E-14	-13.65	QFM+1	yes
	[001]	1150	28800	3.36E-14	-13.47	QFM+1	yes
D19	[100]	950	108000	1.52E-16	-15.82	QFM+1	yes
	[010]	950	108000	1.47E-16	-15.83	QFM+1	yes
	[001]	950	108000	5.92E-17	-16.23	QFM+1	yes

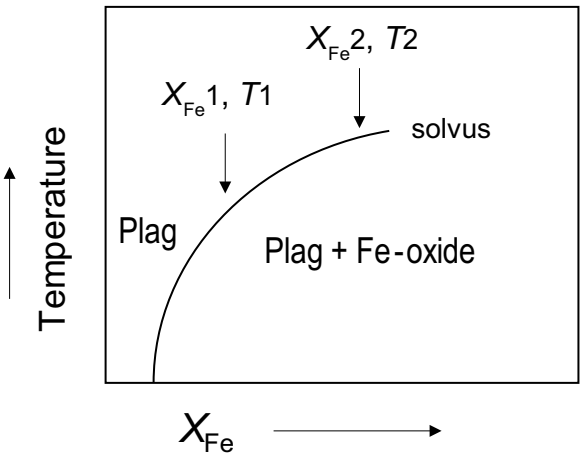

Figure 3.1: Generalized conceptual phase diagram for a binary solid solution illustrating the tendency for higher solvus temperatures with higher solute concentrations.

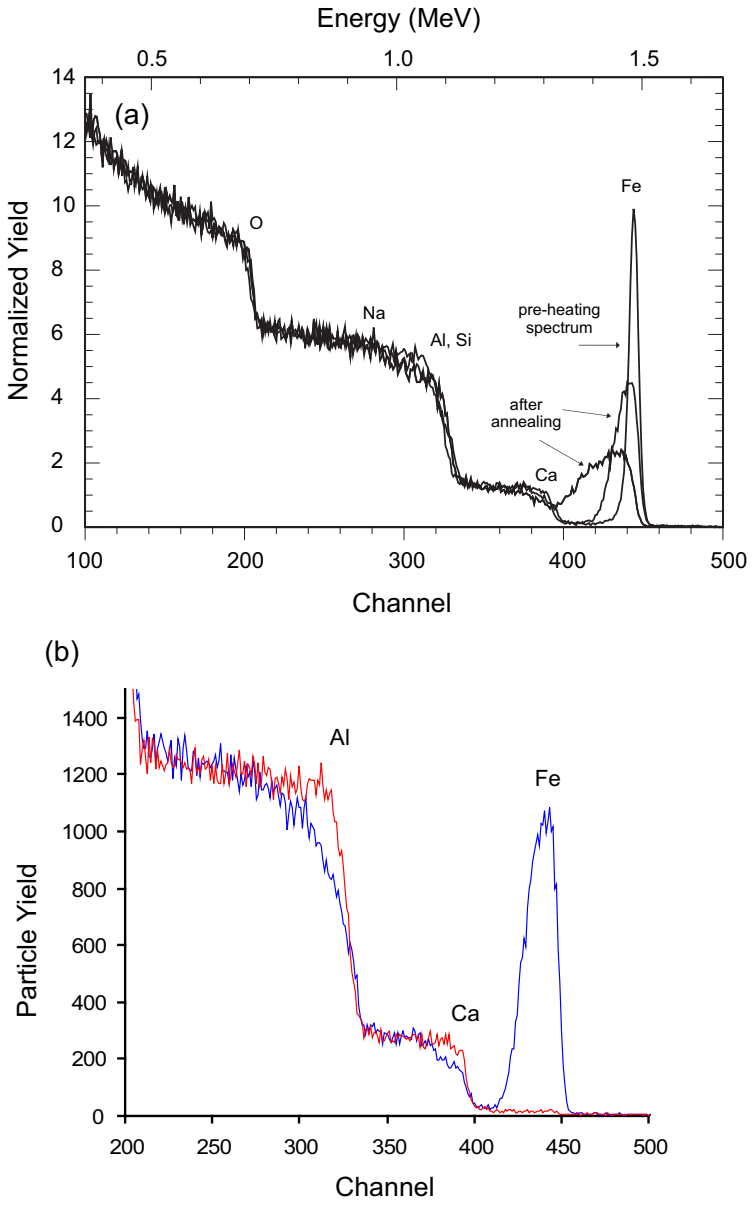

Figure 3.2: (a) Example RBS spectrum for an Fe film on plagioclase before annealing compared with post-annealing spectra at different temperatures. (b) Detailed plot of Al and Ca edges in the RBS spectrum from a polished plagioclase slab (in red) before Fe deposition compared with a spectrum from experiment D07 (in blue) showing the depletion of Al and Ca near the surface after diffusion annealing.

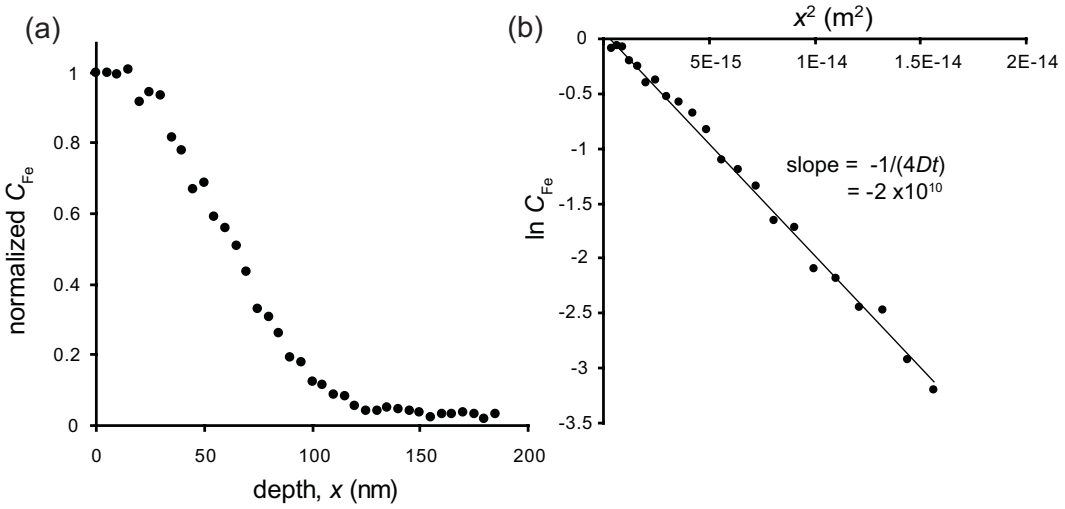

Figure 3.3: Examples of a) a post-annealing depth profile of Fe concentration and b) inversion of the concentration profile through the thin film solution to the diffusion equation for a sample annealed at 1000°C in air (Run D02).

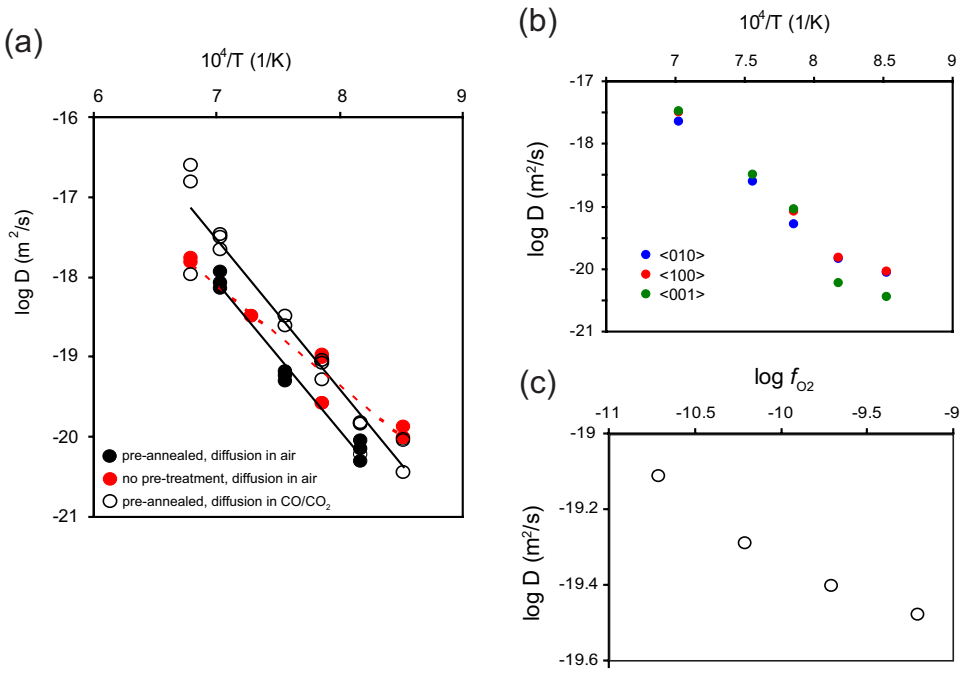

Figure 3.4: a) Arrhenius diagram of Fe diffusion results for sampled annealed in air (solid symbols) and at an oxygen fugacity of QFM+1 (open symbols). Solid red symbols received no pretreatment prior to diffusion anneals, all other samples were heated at 1200°C for 24 hours. b) Diffusional anisotropy for samples annealed at QFM+1. c) Results of Fe diffusion experiments measured as a function of oxygen fugacity.

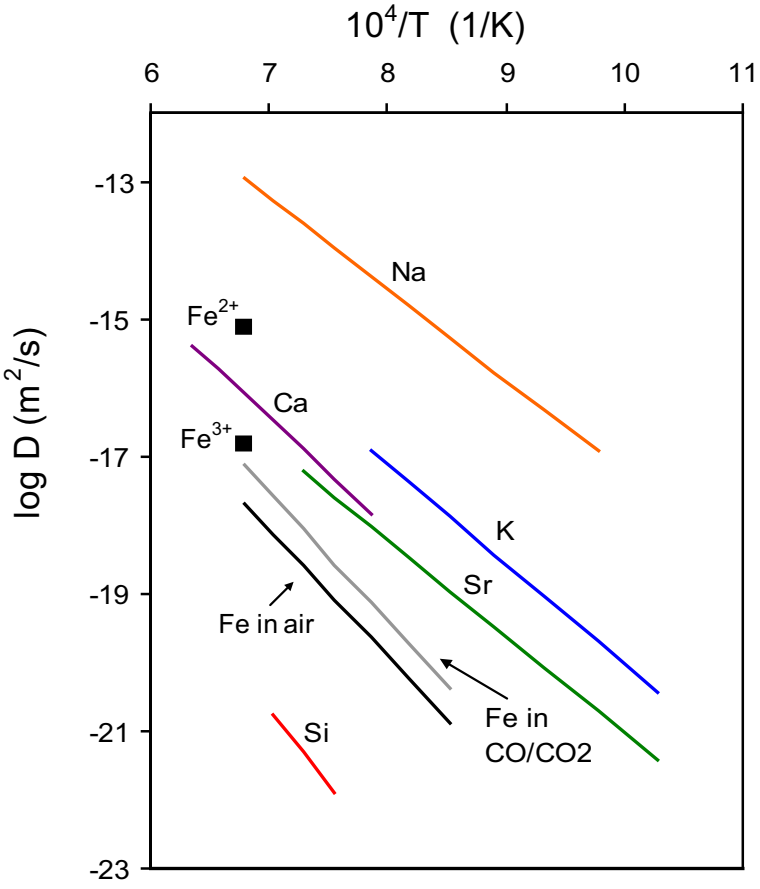

Figure 3.5: Summary of previous data on cation diffusion in plagioclase of intermediate composition. Fe tracer diffusion results of Behrens et al. (1990) measured as a function of f_{O_2} are marked as discrete points. Data from the current study are solid black and grey lines. Sources of data for other cations in plagioclase are as follows: Na and Ca, Behrens et al. (1990); K, Giletti & Shanahan (1997); Sr, Cherniak & Watson (1994); Si, Cherniak (2003)

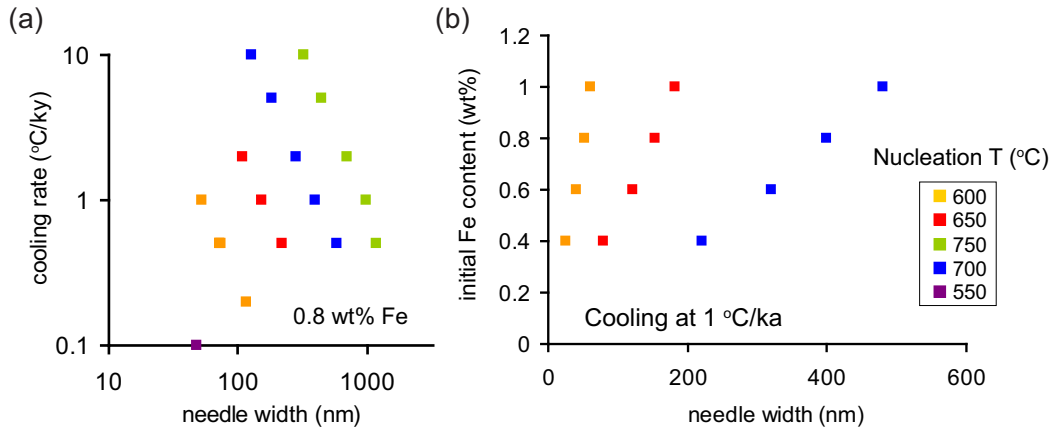

Figure 3.6: a) Model results for growth of magnetite needles for various temperatures of nucleation and cooling rates. b) Variation in magnetite particle growth as a function of initial Fe content in plagioclase in at.wt%.

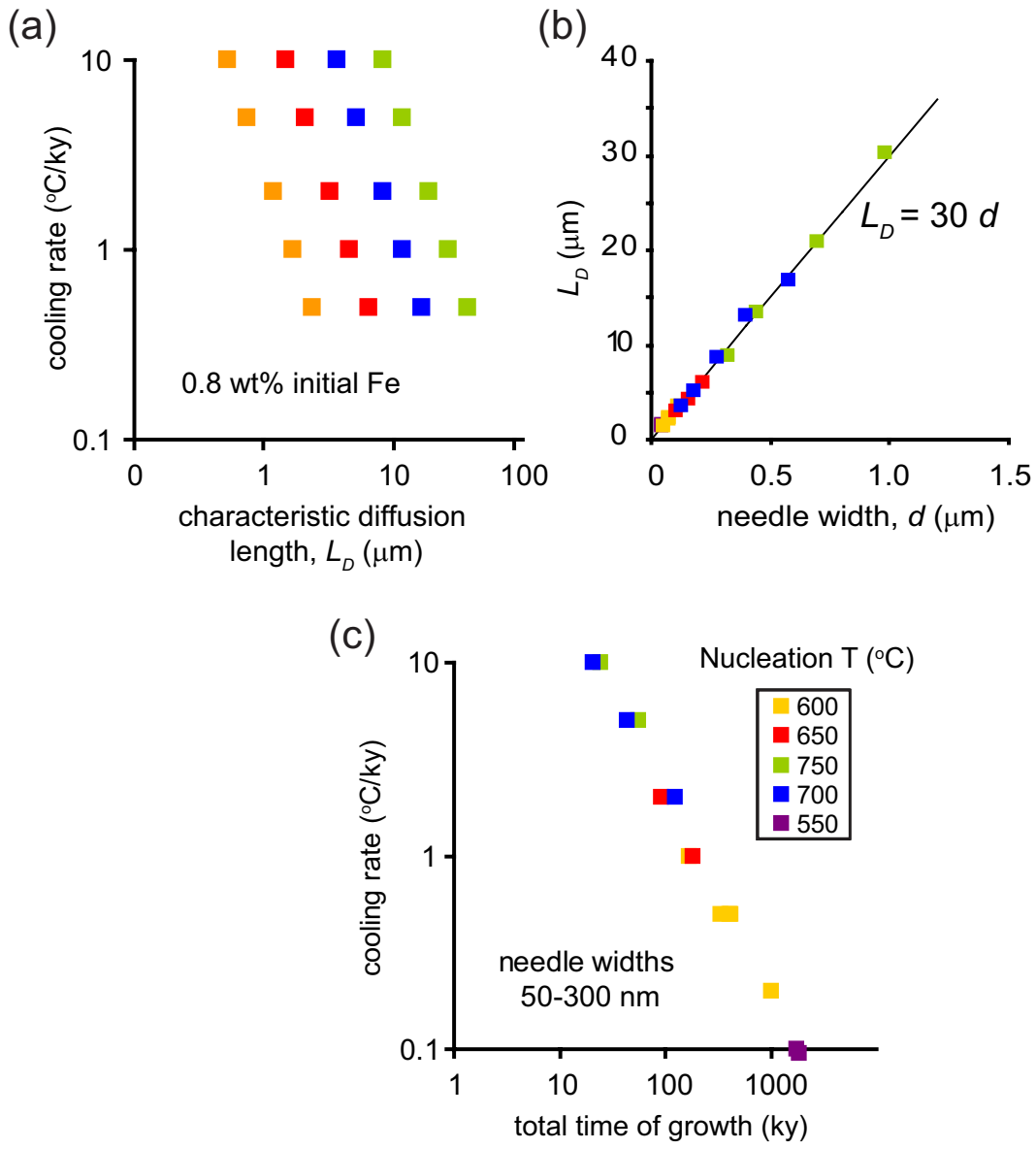

Figure 3.7: a) Characteristic diffusion length scales for magnetite particle exsolution as a function of nucleation temperature and cooling rate. b) Correlation between modeled final magnetite needle width and characteristic diffusion length. c) Time scales for growth of magnetite needles to widths of 50-300 nm for a range of cooling rates.

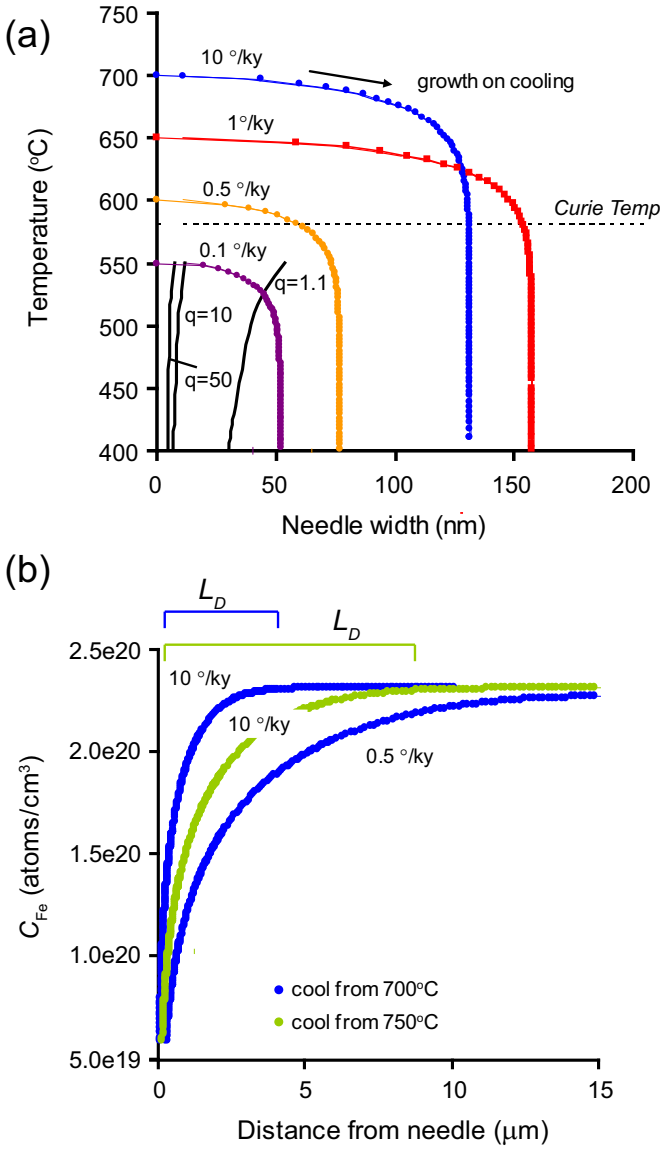

Figure 3.8: a) Growth curves for magnetite needles in plagioclase with an initial Fe content of 0.8 wt.%. T_C of magnetite is indicated with a dashed line. Solid black curves represent blocking contours for magnetite particles with different aspect ratios (q). b) Theoretical Fe concentration profiles in plagioclase adjacent to exsolved magnetite needles. Length of calculated characteristic diffusion length, L_D, is indicated for each profile.

Chapter 4

Remanence Stability and Magnetic Fabric Development in Synthetic Shear Zones Deformed at 500°C

[1] Shear experiments were performed on magnetite-bearing calcite aggregates to examine magnetic fabric development and remanence stability in a deforming system using elevated temperature and pressure to encourage deformation by crystal-plastic processes. Samples composed of 1 wt% pseudo-single domain magnetite (1-2 μm) in a calcite matrix were created with either strong or weak initial fabrics and deformed in coaxial simple shear to strains up to $\gamma = 1.5$ at constant strain rates between 6x10^{-5}-1x10^{-4} s^{-1} at 500°C and confining pressure of 300 MPa. Samples were given weak-field thermal remanent magnetizations prior to deformation. Demagnetization of post-deformation remanence reveals that a primary remanent magnetization can withstand deformation at pressures and temperatures approximately equivalent to greenschist-facies metamorphic

[1] Reproduced by permission of American Geophysical Union. Till, J., Jackson, M., Moskowitz, B., Remanence stability and magnetic fabric development in synthetic shear zones deformed at 500°C. *Geochemistry, Geophysics, Geosystems*, 11(12), Q12Z21, 2010.

conditions on laboratory time scales, but this stability is found to depend on the character of the pre-deformation fabric. The origin of secondary remanence components acquired during deformation is uncertain but is likely to partially result from thermal viscous remagnetization. Complete post-deformation remagnetization in initially anisotropic samples appears to involve a stress-softening or piezoremanent magnetization mechanism. Post-deformation anisotropy measurements show progressive changes in magnetic fabric strength with strain. In the absence of a strong initial magnetic anisotropy, magnetic fabric intensity increases linearly as a function of strain; however, deformation that overprinted an existing fabric results in an apparent decrease of the initial anisotropy at low strains followed by rapid increases in magnetic fabric strength with increasing strain. Our results underscore the important role that initial fabric can play in determining the character of deformation fabrics.

4.1 Introduction

Magnetic fabric measurements are a popular tool for rapidly determining qualitative information about petrofabric orientation and relative strain (Tarling & Hrouda, 1993; Borradaile & Jackson, 2004). In particular, anisotropy of magnetic susceptibility (AMS) measurements are frequently used to map changes in rock textures over broad regions. However, it is difficult to consistently obtain useful quantitative data from magnetic fabrics such as strain, paleostresses, and other deformation history information. Interpretation of magnetic fabrics is complicated because bulk magnetic properties always average signals from different mineral phases, grain size fractions and subfabrics (Borradaile, 1988). Additionally, results from magnetic fabric analysis and standard microstructure analysis reflect the collective strain history of a rock and thus may fail to provide straightforward information about any particular stage of deformation.

Complicating factors that prevent extraction of quantitative data from magnetic fabrics in rocks include strain partitioning and inhomogeneous strain between phases in a rock, lack of information about pre-deformational rock textures, difficulty in interpreting the effects of multiple deformation stages (Evans et al., 2003) and magnetochemical alteration. Despite the necessary caveats involved with detailed interpretation of magnetic fabrics, AMS in bulk samples is still a valuable tool as a rapidly obtained textural

indicator. Magnetic anisotropy studies are commonly used in structural and tectonic research; therefore, a comprehensive quantitative understanding of how magnetic properties reflect deformation history is needed to maximize the information obtained.

Since the work of Graham (1966), who recognized a pattern between AMS directions and finite strain, a number of studies have succeeded in formulating correlations between magnitudes of magnetic anisotropy and strain for naturally deformed rocks where strain estimates are available (Kneen, 1976; Kligfield et al., 1983; Cogné & Perroud, 1988). However, these have sometimes been invalidated by subsequent work (Nakamura & Borradaile, 2001) and most determined relationships are only valid for a particular locality and will not necessarily hold for different lithologies or deformation regimes. Previous experimental magnetic fabric studies have deformed rocks or rock-analogs at room-temperature (Borradaile & Alford, 1988; Hrouda, 1993; Jackson et al., 1993). Such studies usually involve quasi-brittle deformation regimes or large changes in sample volume that are not necessarily representative of natural modes of deformation or AMS development. We present experimental observations of changes in magnetic anisotropy and remanence in material deformed under simulated metamorphic conditions. The goal of this study is to examine the effects of elevated temperatures and pressures that facilitate plastic deformation on AMS development while additionally examining the extent of post-deformation remanence stability for potential paleomagnetic application.

4.2 Sample Preparation

Synthetic samples were composed of 1.0 wt% synthetic Wright 3006 (W3006) magnetite dispersed in a calcite matrix. This magnetite has a nominal grain size of 2-3 μm, placing it in the pseudo-single domain (PSD) grain size range for magnetite. Yu et al. (2002) determined an estimated mean grain size of 1.06$\pm$0.71 μm and an average axial ratio of 1.62 for W3006, and Özdemir & Banerjee (1982) noted a grain size range from 0.2 - 3.8 μm. The magnetite powder used in all samples was annealed in a reducing CO-CO_2 atmosphere at 700°C for 15 hours to remove any pre-existing partial oxidation before mixing. Magnetite stoichiometry was verified through saturation magnetization (M_s) values and Mössbauer spectroscopy. The studied calcite powder was obtained

from single crystals of Iceland spar crushed to an average grain size of 50 μm. Samples were thoroughly mixed until it was visually determined that the magnetite was well distributed (to reduce magnetic interaction effects). Although hand-mixing appears to be effective at dispersing most of the magnetite, we acknowledge the general inability to uniformly distribute magnetite grains without some degree of clustering. In the photomicrographs in Figure 4.1, the magnetite grains are generally well-dispersed, although some clustering is evident, especially along boundaries of large calcite grains.

Test samples of W3006 magnetite in a matrix of high-temperature cement were created to test the thermal stability of thermoremanent magnetization (TRM). A TRM was given to the test samples in a field of 100 μT at 600°C and was subsequently subjected to stepwise thermal demagnetization in air (Figure 4.2b). These measurements indicate that the W3006 magnetite has a median blocking temperature T_b of 530°C, a Curie temperature, T_c of 577°C (Figure 4.2a), and retains approximately 60% of the original TRM intensity at 500°C. This was considered sufficiently stable for the purpose of our experiments.

Two methods of sample preparation were used during the first synthesis step. A hydraulic-oil-medium isostatic pressure vessel was used to cold-press pellets of sample powders under a hydrostatic pressure of 135 MPa to create approximately isotropic samples with weak fabrics that were then shaped and fitted into Ni canisters. These are hereafter referred to as isostatically-prepared material (IPM) samples. To create samples containing strong initial fabrics, the magnetite-calcite powders were cold-pressed directly into a Ni canister under an axial load of approximately 140 MPa, referred to as uniaxially-prepared material (UPM). Cold-pressed sample canisters were placed in a hot isostatic press (HIP) in a gas-medium pressure vessel at 500°C for 5 hours at a confining pressure of 300 MPa. HIP and deformation temperatures were constrained to 500°C to avoid the formation of siderite from magnetite due to decarbonation of calcite which was observed during trial HIP runs at higher temperatures. The color of the starting powders was a pale gray, which darkened to a medium gray after HIP, reflecting densification of the material. During HIP and deformation experiments, oxygen fugacity was maintained within the stability field of magnetite near the Ni-NiO buffer by the Ni canister (Frost, 1991).

No significant changes in critical transition temperatures occurred after hot-pressing, although moderate changes in hysteresis parameters were observed. These values are included in Table 4.1 for comparison with post-deformation values. The rise in coercivity, H_c, and small drop in M_s and the slight rise in T_C after HIP may indicate a small degree of oxidation, however, Borradaile & Jackson (1993) demonstrated that room-temperature hydrostatic compression of magnetite-calcite-cement aggregates at 200 MPa resulted in permanent increases in both coercivity and ratio of remanent magnetization, M_r to M_s, as well as permanent changes to the shape of coercivity spectra. Therefore, it is unclear whether changes in hysteresis parameters seen after HIP represent chemical changes to the magnetic mineralogy. Additionally, the Verwey transition temperature (T_v) is remarkably constant before and after HIP as is the sharpness of the transition (Figure 4.2c). This transition temperature has been shown to be sensitive to small changes in magnetite oxidation state and impurity content (Aragòn et al., 1985; Özdemir et al., 1993), and is therefore a good indication that changes in magnetite chemistry during HIP were minor. The T_v transition temperature at or near 108 K measured for our samples is lower than the T_v=121 K value for ideal, stoichiometric magnetite, but is identical to the value measured for W3006 magnetite by Kosterov (2003). The lower T_v value for W3006 is possibly due to minor impurity levels in the original material that affects T_v but not T_c. There is no evidence for growth of a secondary magnetic phase during HIP.

Microscopic examination of the hot-pressed material revealed dispersed magnetite grains and the presence of abundant, randomly oriented calcite twins that likely originated during crushing (Figure 4.1). No shape-preferred orientation was observed for calcite grains after HIP. Although no overall change in calcite grain size was detected, it is likely that some grain growth occurs in the fine-grained calcite fraction during HIP, as demonstrated by Schmidt et al. (2008). Several samples were cut from each batch of HIP material in the shape of elliptical discs with major and minor axes of 9 mm and 6 mm, respectively. Sample thickness was kept to approximately 1 mm in order to minimize the pure shear component of deformation.

4.3 Experimental Methods

After initial characterization, samples were given a weak-field TRM perpendicular to the disc plane (the shear plane in subsequent deformation experiments) by heating to 600°C and cooling in an applied field of 0.1 mT in an atmosphere of flowing Ar. One sample was left unmagnetized before deformation. Test samples that were heated to 600°C showed minor changes in saturation magnetization and low temperature remanence (Table 4.1, Figure 4.2c), which indicates that thermal alteration of magnetite during TRM acquisition results in slight oxidation.

Sample discs were placed between pistons of alumina rod cut at 45° angles and then fitted into a nickel sheath and encased in an Fe jacket between larger ceramic pistons. Experiments were performed at 500°C with a confining pressure of 300 MPa in a gas-medium pressure vessel designed for triaxial deformation (Paterson, 1990). Figure 4.3 is a simplified diagram of the sample orientation in the deformation vessel. More details about the apparatus and a complete schematic diagram of a similar sample assembly can be found in Hustoft & Kohlstedt (2006). Simple shear experiments were performed at constant piston displacement rate, corresponding to constant shear strain rates between $6\text{x}10^{-5}$ s^{-1} and $1\text{x}10^{-4}$ s^{-1}. The applied load on the pistons was increased as necessary to maintain the strain rate. Differential stress was therefore not constant throughout the experiment and the maximum differential stresses varied according to the total strain (Table 4.2). Experiment times ranged from 1.5 to 6 hours. At the end of each experiment, differential loads on the samples were removed and samples were quenched to room temperature at an average rate of about 50°/min.

Rutter (1974) noted that brittle behavior is suppressed by a confining pressure of 150 MPa in experimental deformation of calcite rocks at 300°C and above. The larger confining pressure and temperature used in our experiments both strongly favor calcite deformation by crystal-plastic processes. Furthermore, several previous studies have documented plastic deformation of calcite at identical or similar conditions (Turner et al., 1954; Rutter, 1974; Walker et al., 1990; de Bresser & Spiers, 1993; Barnhoorn et al., 2004). Although magnetite is not expected to deform plastically at our chosen conditions (Atkinson, 1977), the bulk sample deformation behavior is controlled by calcite rheology and is likely to be deforming in the ductile regime.

To correct for the strength of the Ni sheath in our experiments, a deformation run was performed on a Ni sheath containing only a thin Ni foil between angled ceramic pistons under the same conditions used in the experiments. We attempted to subtract the resulting stress-strain curve from that of each sample to estimate the maximum applied stress on each sample. However, the Ni strength was found to account for a significant proportion of the total applied load (about 60% for most experiments) and both the Ni and the sample experiments exhibited strain-hardening behavior. Therefore, there is large uncertainty associated with the Ni correction, and the maximum stresses shown in Table 4.2 should only be taken as upper limits.

It is important to note that the furnace heating coils in the deformation vessel produce a significant magnetic field when the vessel is at temperature. This field was calculated to be approximately 4 mT in the region of the samples using the known coil geometry and average current loads for operation at 500°C from furnace calibrations. The current is turned off during sample cooling and the field strength in the vessel at room temperature was measured to have a similar order of magnitude as the earth's field with an upward inclination.

To distinguish remagnetization effects due to partial reheating in an applied field from possible effects of deformation and applied stress, acquisition of partial TRM (pTRM) was measured on undeformed samples from both IPM and UPM samples. First, pTRMs were given at 500°C in a 0.1 mT field at high angles (90° or 45°) to an original total TRM given in the same field. This was intended to determine the amount of remagnetization that can be attributed to simple reheating to the experimental temperatures. In IPM samples, the original total TRM was given in an upward direction, perpendicular to the sample plane. To test the effect of initial fabrics on pTRM acquisition, total TRMs were given to two UPM samples in directions parallel and perpendicular to K_{min}. Additionally, one sample was given a total TRM and then reheated in the pressure vessel for 30 minutes at experimental conditions with no applied stress in order to observe pTRM acquisition resulting from the field of the furnace heating coils.

After deformation, samples were recovered by grinding away the metal jacket material. Samples were progressively demagnetized in an alternating field (AF) demagnetizer up to 200 mT to obtain demagnetization spectra and directional remanence

components. AMS and anisotropy of anhysteretic remanent magnetization (AARM) measurements were used to characterize magnetic deformation fabrics, and anisotropy of isothermal remanent magnetization (AIRM) was also measured on deformed IPM samples. Hysteresis and low-temperature remanence measurements were made again after deformation to monitor changes in magnetic composition and coercivity. First-order reversal curve (FORC) measurements were also made on selected samples to observe changes in coercivity distributions and interaction field (Pike et al., 1999; Roberts et al., 2000). FORC data were processed with the FORCinel software program (Harrison & Feinberg, 2008).

AMS measurements were performed in a KLY-2 Kappabridge susceptibility meter with a 15-position measurement scheme. Remanence anisotropy was determined by imparting an ARM in a maximum AF of 100 mT with a 0.1 mT bias field and a 9-position measurement scheme measured on a 2-G Enterprises superconducting rock magnetometer. Anisotropy of partial ARM (ApARM) was measured on IPM samples using a maximum AF of 100 mT with a bias field applied in AF windows of 100-10 mT ("hard" fabric) or 10-0 mT ("soft" fabric). AIRM was measured with a 36-position measurement scheme on a Princeton Measurements Corporation vibrating sample magnetometer (VSM) using a saturating field of 1.0 T. Magnetic fabric ellipsoid shapes are described in terms of magnetic lineations ($L = K_{max}/K_{int}$), magnetic foliations ($F = K_{int}/K_{min}$) and the shape parameter T of Jelinek (1981), where K_{max}, K_{int}, and K_{min} are the maximum, intermediate and minimum susceptibilities. The degree of anisotropy was determined by the parameter P ($P = K_{max}/K_{min}$) of Nagata (1961). Hysteresis measurements were made on a VSM with a maximum field of 1.0 T. Low-temperature remanence measurements included field-cooled and zero-field-cooled warming curves of a 2.5 T saturation isothermal remanent magnetization (SIRM) that was imparted at 20 K along with room temperature SIRM cooling and warming curves from 20 to 300 K in a Magnetic Properties Measurement System (MPMS) by Quantum Designs. In all figures containing magnetic orientation data, sample coordinates are chosen such that the shear plane contains the north and east directions, where east is up-dip and north is along strike, and the shear sense when looking at a cross-section of the shear plane is top to the west, or down-dip.

4.4 Results

4.4.1 Initial Fabrics

IPM samples were found to lack a distinct initial magnetic fabric, as indicated by P values of 2-4% anisotropy from AMS measurements (Table 4.3). Principal directions of AMS ellipsoids among IPM samples lack a consistent orientation (Figure 4.4a). Additionally, AMS measurements for several samples were characterized by large angular uncertainties and therefore have no meaningful principal directions. Samples from uniaxially-prepared material (UPM) were characterized by well-defined magnetic foliation fabrics (Figure 4.4b) perpendicular to the compression axis during synthesis, with P values ranging between 9 and 12% and comparatively small angular uncertainties about the K_{min} axis (Table 4.3). UPM samples were cut and oriented so that the initial foliation was perpendicular to the shear plane in order to maximize the observable effects of fabric overprinting. AARM principal directions have small but measurable differences from AMS principal directions in both sets of samples.

4.4.2 Acquisition of pTRM

For both IPM and UPM samples, pTRM acquisition experiments (Figure 4.5a,b) resulted in acquisition of soft components that are well-aligned with the direction of the cooling field. The newly acquired component is generally demagnetized in AFs around 12 mT. The direction of the sample fabric with respect to pTRM acquisition had a small, but observable, effect (Figure 4.5a,b). The sample that was given a total TRM in the plane of the magnetic foliation (TRM$\perp K_{min}$) acquired a slightly larger pTRM in the direction perpendicular to the foliation (pTRM$\| K_{min}$) than the sample that was magnetized with a total TRM out of the foliation plane, with an in-plane pTRM. The reheating experiment performed in the pressure vessel without deformation of the sample (Figure 4.5c) was designed to measure *in-situ* pTRM acquisition resulting from the field in the furnace. AF demagnetization revealed multiple overlapping components of remanence, including a stable component oriented parallel to the original total TRM. The soft components acquired during this reheating experiment are removed by demagnetizing fields of 25 mT.

4.4.3 Demagnetization of Post-Deformation NRM

Orthogonal vector component plots (Zijderveld, 1967) of AF demagnetization results for all samples after deformation are displayed in Figure 4.6. Two distinct patterns of remagnetization are observed. IPM samples (Figure 4.6a) typically have multiple remanence components, including a nearly vertical, high-coercivity component (removed in fields >20 mT) oriented parallel or sub-parallel to the pre-deformation TRM. The low-coercivity components (removed in fields <20 mT) in IPM samples do not have a systematic orientation, and they have variable inclinations, with directions that are not uniformly consistent with a vector rotation relative to the sense of shearing. One IPM sample, Iso07-04, was not magnetized prior to deformation and contained a single, low-coercivity component with shallow inclination. The SuperIAPD software was used to perform principal component analysis on the demagnetization data (Figure 4.7a); these results are listed in Table 4.4. Although we have only identified soft and hard components of remanence for IPM samples, there is curvature from overlapping coercivity spectra that makes it difficult to rule out the existence of additional components. The proportion of remanence represented by weak-field pTRMs in test samples is small compared to the proportion of remanence represented by the remagnetized portion in deformed IPM samples. Similarly, the coercivities of remagnetized components observed in IPM samples are larger on average than the coercivity of the remagnetized components in weak-field pTRM tests, but are nearly identical to that of the pTRM acquired during reheating in the pressure vessel.

Demagnetization of several UPM samples revealed a single remanence component that is not aligned with the original TRM, and that is distinctly different than the pattern seen in IPM samples. However, samples An07-09 and An07-08 (Figure 4.6b) have more complex "NRM" patterns. Additionally, one UPM deformation experiment (sample An07-04) failed to provide a reliable strain measurement and was considered unsuitable for magnetic fabric analysis; however, demagnetization of this sample also revealed a single remanence component so it is included in Figure 4.6 for comparison. Nearly all post-deformation "NRM" intensities are higher than the pre-deformation TRM (Figure 4.8c).

4.4.4 Changes in Rock Magnetic Properties

No correlation is observed between median destructive field (MDF) of "NRM" and strain in either set of deformed samples (Figure 4.2d, 4.8d) although it is generally lower than before deformation. MDF values of around 30 mT for both the HIP material and starting magnetite powders are similar to MDFs measured by AF demagnetization of ARM in W3006 magnetite by Yu et al. (2002) and Özdemir & Banerjee (1982). The remanence intensity (J_{NRM}) of our samples typically increased after deformation with respect to the pre-deformation TRM intensity (J_0) but did not vary consistently with strain (Figure 4.8c). Although Borradaile (1994) found that remanence intensity was reduced at small strains in triaxial deformation, our observed increase likely originates from the presence of a stronger field during experiments compared to that applied during TRM acquisition. Likewise, variation in the J_{NRM}/J_0 ratio among deformed samples may result from differences in vertical position of the sample within the furnace between experiments or from small field variations due to differences in the amount of current applied to the furnace heating coils to maintain experimental temperatures.

M_r/M_s ratios vary slightly among deformed samples and are elevated relative to the pre-deformation ratio. Table 4.1 indicates a drop in M_s for deformed samples, however, considering the small volume of our samples we note that these values are susceptible to mass normalization errors due to small amounts of mass loss during repeated sample handling. The consistency of diagnostic transition temperatures in Table 4.1 suggests that lowered post-deformation M_s may not reflect a real change in magnetite stoichiometry. Nonetheless, if limited magnetite oxidation does occur during deformation, its effect on magnetic anisotropy development will be minimal and it is unlikely to have a significant impact on remanence stability. Bulk H_c increased significantly after deformation for all experiments. Published flow laws for magnetite (Atkinson, 1977) indicate that magnetite would not accumulate an appreciable amount of plastic strain at the experimental conditions, but the rise in coercivity indicates that the deformation process has increased the internal stress state in the magnetite grains (Heider et al., 1987), as was determined for room-temperature deformation by Jackson et al. (1993). Similarly, gradients of IRM acquisition curves from FORC measurements show a single coercivity component that shifts from low to moderate coercivities after HIP and deformation (Figure 4.8f). FORC diagrams (Figure 4.9) have closed-contour structures with

no difference in interaction fields between the starting HIP material and deformed samples, and are comparable to FORCs measured on similarly-sized synthetic PSD Wright magnetites by Muxworthy & Dunlop (2002). The small sample size necessitated the use of large smoothing factors during FORC processing. Although some degree of magnetostatic interaction is indicated by the FORC diagrams, it is not possible to determine how much of the interaction field is attributable to domain interactions within single grains or to interactions between grains, or how much the distribution is smeared by the high smoothing factor (SF) values (cf. Roberts et al., 2000).

Bulk susceptibility, κ, was calculated as the mean of AMS measurements and decreased in all samples after deformation by 10-35% (Figure 4.8e). This observed drop in mean susceptibility is somewhat larger than the 10% decrease in κ observed in previous room-temperature studies (Jackson et al., 1993; Borradaile, 1996) for samples exposed to comparable stresses ($\sim$100 MPa). Jackson et al. (1993) identified two mechanisms by which a drop in bulk susceptibility may result after deformation. An increase in H_c resulting from higher defect densities that inhibit domain wall motion can lower the intrinsic susceptibility, or an increase in the demagnetizing factor, N, can result in lower observed κ. Although we see no evidence for changes in magnetic grain shape anisotropy after the experiments, N has been found to depend on the domain structure of grains (Merrill, 1977) and domain wall displacement from minimum energy positions can produce large changes in N for small MD grains (Dunlop, 1983). Therefore, domain wall pinning by increased defect concentrations could potentially raise N and lower κ by enough to account for the observed changes in our samples. The larger magnitude of susceptibility decrease in our study compared to earlier studies may be explained by the smaller magnetic grain size used in our experiments (1 μm compared with 40 μm) because Dunlop (1983) calculated that the largest potential for increase in N by domain wall pinning occurs at the small end of the MD grain size spectrum.

4.4.5 Changes in Magnetic Fabric Character

Magnetic fabrics of deformed samples are largely characterized by a flattened anisotropy ellipsoid, or a magnetic foliation. Table 4.5 contains a summary of magnetic fabric measurements for all deformed samples. The degree of anisotropy in IPM samples increases in a progressive linear pattern with increasing shear strain for both AMS and

AARM measurements (Figure 4.10a). The shape parameter T (Figure 4.11a) indicates that the anisotropy ellipsoid becomes oblate at low strains and maintains this shape with increasing degree of anisotropy at higher strains. Although the degree of anisotropy for remanence fabrics measured by both AIRM and AARM is slightly higher than that measured by AMS, both remanence fabrics exhibit the same trend with changing strain intensity and also generally show the same changes in fabric shape displayed by AMS measurements. ApARM for IPM samples reveals distinct remanence fabrics carried by high- and low-coercivity grain sub-populations (Figure 4.12). K_{min} inclinations for the lower coercivity fractions are generally shallower than those for total AARM measurements but are clustered around the same orientations. The higher coercivity ApARM axes are more scattered, possibly reflecting a different rotational response to deformation by different grain size fractions.

In UPM samples deformed to small shear strains, the deformation fabrics resemble the initial fabric but are slightly weaker and less oblate. At higher strains, the pre-deformation fabric is overprinted and the shape of the anisotropy ellipsoid changes sharply. As the initial foliation is overprinted, a magnetic lineation develops at the intersection of the shear plane and the initial foliation plane (Figure 4.11b), and the fabric shape returns to a foliation around a shear strain of $\gamma = 1$ as the deformation fabric becomes more pronounced. This results in an initial apparent decrease in the degree of anisotropy at small strains followed by a rapid increase after the initial fabric becomes overprinted. As in IPM samples, the remanence anisotropy in UPM samples follows the same pattern of changes in intensity and fabric shape seen with AMS.

4.4.6 Fabric Orientation

The magnetic foliation of deformed IPM samples is sub-parallel to the shear plane and dips shallowly for all strains (Figure 4.4c). Changes in orientation of the fabric ellipsoid are best defined by K_{min} axes, or poles to magnetic foliation. The inclination of K_{min} undergoes only small changes from low to high strain, and does not consistently rotate in the direction of shearing (Figure 4.10b). AARM fabric orientations tend to be distinct from those of the AMS ellipsoid, with the largest directional differences seen at low strains ($\gamma < 1$). Neither the AMS nor AARM fabric is well-aligned with the minimum stretching axis of the bulk strain ellipsoid, but rather they remain sub-parallel to the

orientation of the strain ellipsoid. The rate of rotation for both remanence and AMS minimum axes is slower than that of the theoretical minimum stretching axis. AIRM fabric orientations were nearly identical to those of the AARM fabric in all samples. Borradaile & Alford (1987) also reported rotation of AMS principal axes that does not match the rate expected for lines rotating in homogeneous strain in their deformation experiments.

UPM samples deformed to small strains have a foliation oriented perpendicular to the shear plane, which mimics the pre-deformation fabric (Figure 4.4d). With progressive strain, K_{min} axes remain in or near the shear plane up to strains of $\gamma = 1$, and rotate rapidly to become steeply inclined with the shear plane at high strains (Figure 4.10b). After the initial fabric is effectively overprinted, K_{min} axes rotate much more rapidly than the minimum stretching axis of the strain ellipsoid over the higher-strain interval. These samples were also characterized by significant differences between AMS and AARM orientations. Rotation of AARM minimum axes is relatively smooth and progressive and is also more rapid than that of the minimum stretching axis. The net rotations of magnetic fabric ellipsoids are consistent with shear direction in UPM samples. Also, the deflection of remanence vectors toward the shear plane in UPM samples closely mirrors the rotation of UPM minimum AMS directions toward the axis of maximum compression but is only loosely correlated with the rotation of AARM minimum directions (Figure 4.7b).

4.5 Discussion

4.5.1 Remagnetization During Deformation

Post-deformation remanence patterns of IPM samples (Figure 4.6a) are in most cases essentially indistinguishable from a pTRM acquired by reheating in the deformation vessel (Figure 4.5c), which would result in partial overprinting of the original TRM. Neither the univectorial UPM magnetizations nor the low-coercivity IPM components are consistently oriented away from the maximum stress direction, so there is insufficient evidence to suggest that strain-induced grain rotation is the primary mechanism that determines post-deformation remanence directions. Vector rotation produced by shearing would be expected to result in remanence directions upward out-of-plane and

in the dip-direction of the shear zone since the shear sense is top moving down-dip, and should also result in similar remanence intensities before and after deformation. Any remanence produced by an axial field in the deformation vessel should be up-dip and upward out-of-plane in sample coordinates, reflecting the 45° up-dip inclination of the furnace field to the shear plane (Figure 4.3). Neither of these expected direction patterns is observed consistently in either set of samples, although Borradaile & Mothersill (1989, 1991) also observed non-systematic and unexpected rotation of NRM directions during room-temperature experimental deformation. On the basis of pTRM experiments on test samples and generally higher post-deformation remanence intensities, it is likely that the remagnetization in IPM samples is a pTRM; however, it is difficult to determine what factor is controlling the direction of the remagnetized components. The high coercivity ChRM components are interpreted simply as those portions of the original total TRM that have withstood deformation.

Most UPM samples lack a stable component that could be identified as part of a pre-deformation TRM, which suggests that most samples have been completely remagnetized. Also, the different demagnetization patterns in IPM and UPM samples suggest that the presence of a strong pre-deformation fabric has somehow facilitated remagnetization of UPM samples. This is possible if a piezoremanent magnetization (PRM) mechanism contributes to remagnetization during experiments. Initial fabrics in UPM samples are oriented such that the average direction of maximum remanence susceptibility is near that of the maximum compressive stress direction. This alignment of magnetite grains results in a higher potential for stress-demagnetization than the nearly random grain orientation distributions in IPM samples. It has been noted in previous studies of syn-strain PRM acquisition (e.g., Borradaile, 1994, 1996) that magnetic softening from differential stresses has a stronger effect than strain-induced grain rotation, and that the direction of the PRM acquired is typically independent of the stress direction and is controlled by the direction of the ambient field. Although we do not observe systematic field control over the remanence directions, a PRM remagnetization mechanism in the presence of a field, or equivalently, a pTRM facilitated by stress-softening are possible explanations for different remagnetization patterns between IPM and UPM samples.

Like the IPM samples, the “NRM” directions for UPM samples do not all lie in the

quadrant expected if the furnace field controlled the remanence direction, so again the main factor controlling the direction of post-deformation remanence cannot be determined. However, when the experiment geometry is considered, where the compressive stress axis is coaxial with the field during experiments, this may not be a surprising result. The net effect of the applied stress is to reorient the remanence away from the axis of compression, while the field exerts a force to reorient the remanence toward the same axis. If the two competing forces largely cancel, the resulting remanence directions may be predictably non-systematic. Also important to note is that although we have tried to show progressive changes by using different strain increments for different samples, repeated experiments on a single sample greatly reduce the effects of heterogeneity between samples when possible.

Large uncertainties associated with our estimated experimental stresses make it impossible to discuss the extent or character of remagnetization in terms of differential stress. In addition, these results cannot be directly compared to natural stress-assisted remagnetization processes in part because fields of the same order of magnitude used in our experiments are exceedingly rare in nature. However, viscous remagnetization effects on geologic time scales could effectively induce remagnetization comparable to that observed in experiments. Although a viscous remagnetization mechanism in our samples is possible given the relative proximity of our experiment temperatures to the sample blocking temperatures, it would be difficult to isolate its effect from other remagnetization processes. If a viscous process was dominant, one would expect it to operate identically in both sets of samples and any effect should be dependent on experiment duration, which is not clearly the case for our samples. Further analysis would benefit from development of a theoretical treatment incorporating the combined effects of stress-reorientation, temperature, field, and time to calculate the threshold conditions for complete remagnetization in PSD magnetite.

4.5.2 Fabric Character

The changes in principal directions of the magnetic fabric in IPM samples are not large enough to be reliably used as shear sense indicators. The net change in orientation of the AMS ellipsoid from small to large strain indicates a shear sense opposite to that imposed (Figure 4.4b). Rathore & Becke (1980) also noted conflicting senses of

shear movement indicated by magnetic fabrics along different sections of a natural shear zone, suggesting that interpretation of shear sense from AMS directions is not always straightforward. Net rotation of the AARM ellipsoid in IPM samples provides a better, and correct, indication of shear sense (Figure 4.10b). However, the systematic and progressive increase in degree of anisotropy with shear strain means that both magnetic fabric measurement methods provide an excellent representation of relative strain in IPM samples, even though determination of principal stress directions from magnetic ellipsoid axes is less straightforward in this case.

The behavior of UPM magnetic fabrics can be easily understood in terms of overprinting an initial fabric with a deformation fabric. Previous studies have noted that when simple shear strains are superimposed on pure shear strains, the strain ellipsoid may change shape in an undulating fashion, and the two strains may partially cancel each other, returning the strain ellipsoid to a more spherical shape before becoming ellipsoidal once again (Ramberg, 1975; Means et al., 1980; Ramsay & Huber, 1983). Similarly, Ruf et al. (1988) observed that magnetic fabrics in a mylonitic zone became weaker with increasing strain compared to the well-developed anisotropy in the granite protolith and Borradaile & Alford (1987) noted decreasing eccentricity of AMS fabric in early stages of deformation experiments for samples with initial fabrics at high angles to the shortening direction. Deformed UPM magnetic fabrics mimic this type of behavior at small strains with an apparent decrease in anisotropy as the pre-deformation fabric is overprinted, which is observed as a single undulation of the fabric ellipsoid shape (Figure 4.11a). A similar pattern of magnetic fabric shape change has been observed previously in weakly deformed mudrocks (e.g., Kligfield et al., 1981; Pares, 2004), where a deformation-induced cleavage overprints a primary bedding fabric, producing fabric shape changes from oblate to prolate and back to oblate. The direction of the net rotation of fabric axes in UPM samples is consistent with the direction of shearing. AARM ellipsoids change more progressively in orientation than AMS ellipsoids, and therefore provide a clearer indication of shear sense. However, the apparent decrease in anisotropy at low strains means that relative deformation intensity is not accurately indicated by comparing fabric intensities among UPM samples.

4.5.3 Potential for Complex Fabrics

The stable (non-rotated) ChRM components of post-deformation remanence in IPM samples suggests the presence of a non-rotating fraction of grains during deformation, while the progressive increase in the degree of anisotropy with strain clearly suggests that a fraction of rotating grains is becoming aligned by the deformation process. Thus, we can infer that separate magnetic sub-fabrics are carried by these distinct grain fractions, and that IPM samples really carry a composite magnetic fabric. We also note that because the stable ChRM is carried by the higher coercivity component, the non-rotating fraction is likely to be composed of smaller or higher aspect-ratio grains that were aligned in stable or metastable positions prior to deformation (possibly in or near the shear plane) that inhibited rotation. Figure 4.13 is a conceptual model in which deformation of a theoretical rock containing two distinct subsets of rotating and non-rotating grains results in a composite fabric with a magnetic foliation that is more shallowly dipping than that of the strain ellipsoid. This model also produces a smaller net rotation of principal fabric axes than the strain ellipsoid. We propose that the deformation behavior of IPM samples is similar to this model, and is responsible for the small changes in orientation and the subparallel alignment of the magnetic fabric with the strain ellipsoid. Results from ApARM measurements support this idea since the fabric carried by the "soft" fraction undergoes a larger net rotation and has generally more steeply dipping foliation planes than total ARM fabric (Figure 4.12). However, the pARM fabrics are not clear enough to elucidate the behavior of all magnetic grains in the sample. There is no evidence from remanence measurements to suggest that the deformation fabrics in UPM samples are composite in nature, or that different grain fractions have exhibited different deformation responses as in IPM samples. However, orientation differences between AMS and AARM principal directions in both sets of samples suggest some degree of fabric complexity.

4.5.4 Origin of AMS/AARM Discrepancies

Inverse Fabrics

The observations of Özdemir & Banerjee (1982) suggest that the synthetic magnetite used in our experiments has a broad grain size distribution, and there potentially exists a

small fraction of single-domain (SD) or SD-like material in our samples. The measured deformation fabrics are clearly not pure inverse fabrics as expected for SD particles, however, a fraction of fine-grained magnetic material could produce an inverse fabric component that would result in small differences between AMS and AARM principal direction orientations (Rochette, 1988; Rochette et al., 1992). Since the misorientation between AMS and AARM directions varies among samples, this explanation would require high variability in the quantity of fine-grained material among samples. This seems unlikely if one considers that the theoretical average number of magnetite grains per sample is on the order of 10^8 for the magnetite grain size and concentration used in our synthesis. Nevertheless, some heterogeneity among samples is possible. Although it would be possible to choose some configuration of SD-like grains for each sample that would reproduce our fabric orientation results when combined with a normal fabric component, there is not enough evidence to show that such inverse fabric components exist in our samples. The analysis is further complicated by the fact that rotation behavior during deformation can vary among grain-size fractions as described above for IPM samples.

Interaction Effects

Alternatively, interaction effects could contribute to discrepancies between magnetic fabric measurement methods. Due to the difficult nature of dispersing magnetic grains, it is generally not possible to produce synthetic samples with uniformly distributed particles, especially with fine grained material, such as that used here. A possible effect of magnetic particle clumping or clustering during initial mixing of sample materials is the creation of distribution anisotropy (Hargraves et al., 1991). Since it is known that interactions among fine-grained magnetic particles affect ARM acquisition, even at concentrations as low as 0.01% (Sugiura, 1979; Egli, 2006), it is conceivable that interactions caused by distribution anisotropy can give rise to discrepancies between AMS and AARM fabric directions. Interactions tend to have opposite effects on ARM and AMS acquisition (Muxworthy & Williams, 2004; Egli, 2006); therefore, certain distribution geometries may achieve an inverse fabric similar to that carried by SD particles. Although most work on interactions in magnetite refers only to SD particles, the relatively high concentration of PSD magnetite used in our experiments could produce

non-negligible interaction effects. Further work on magnetic interactions in grain sizes larger than SD could help to assess their significance in this study, but ultimately, without knowing the geometry of grain distribution in our samples it is difficult to predict how distribution anisotropy would affect our measured magnetic fabrics.

4.6 Conclusions

High-coercivity remanence components present after deformation in IPM samples are interpreted as ChRMs, and demonstrate the ability of a primary thermal magnetization to survive deformation at pressure and temperature conditions approximately equivalent to upper greenschist-facies metamorphism on laboratory time scales. However, this remanence stability may be highly dependent on the presence (or absence) and character of a pre-deformational fabric, as pre-existing anisotropy could either stabilize a remanence or facilitate overprinting. The post-deformational remanence displayed by UPM samples probably represents a complete remagnetization by a combination of stress, field, and temperature and appears to be independent of grain rotation effects. PRM acquisition and stress-softening mechanisms likely contribute to complete remagnetization during our deformation experiments but were not sufficient to remove a primary magnetization in IPM samples. We also note that viscous remagnetization processes are not considered in our experiments, and remanence stability in natural systems will depend on the duration of exposure to heat and stress associated with a metamorphic event.

Progressive changes in anisotropy intensity for material with weak initial fabric suggests that magnetic fabric strength is a good indicator of relative strain for these samples, but a relatively poor kinematic indicator. Conversely, in samples with strong initial fabric, magnetic fabric strength is a poor indicator of relative strain due to superposition of deformation fabrics with a pre-existing anisotropy, but sense of shearing is more clearly demonstrated than in IPM samples. Distinct differences in orientations of AMS and AARM principal axes are attributed to a combination of fine-grained material and magnetic interaction effects. The presence of a pre-deformation fabric in our experiments has been shown to have significant effects on both remanence stability and magnetic fabric development in deformed samples.

Table 4.1: Changes in magnetic properties after HIP, TRM acquisition, and deformation.

	T_V (K)	T_C (°C)	M_s (Am^2/kg)	M_r (Am^2/kg)	M_r/M_s	H_c (mT)
Mixed sample powders	108	577	0.812	0.048	0.059	6.9
HIP material	108	585	0.771	0.065	0.084	9.6
Post-TRM Acquisition	108	–	0.752	0.072	0.095	11.0
Deformed IPM samples	107	576	0.677	0.080	0.118	13.7
Deformed UPM samples	108	582	0.680	0.086	0.123	14.6

Table 4.2: Conditions for individual deformation runs.

Sample	Shear strain	Strain rate (s^{-1})	Estimated max. stress (MPa)	Experiment length (hrs)
		IPM samples		
Iso07-11	0.3	6E-05	68	1.17
Iso07-12	0.6	8E-05	79	2
Iso07-04	1	8E-05	81	3.25
Iso07-05	1	8E-05	88	3.4
Iso07-10	1.5	1E-04	150	5
		UPM samples		
An07-01	0.3	6E-05	71	1.17
An07-05	0.6	8E-05	103	2
An07-09	1	8E-05	98	3.25
An07-07	1.3	1E-04	96	4.25
An07-08	1.5	1E-04	118	5.5

Table 4.3: Pre-deformation magnetic fabric intensity, shape, and orientation for synthesized samples.

Sample	L	F	T	P_0	Dec. K_{max}	Inc. K_{max}	Dec. K_{min}	Inc. K_{min}	e12[a]	e23	e31	$\chi \times 10^{-6}$ m^3/kg
						AMS						
Iso07-04	1.018	1.019	0.027	1.037	216	22	58	66	49.68	48.65	30.05	5.80
Iso07-05	1.016	1.004	-0.561	1.040	244	44	137	16	63.89	82.23	57.93	5.60
Iso07-10	1.007	1.003	-0.402	1.011	262	67	152	8	10.65	23.90	7.52	5.38
Iso07-11	1.005	1.015	0.524	1.020	76	33	187	29	14.03	4.51	3.43	5.30
Iso07-12	1.011	1.007	-0.182	1.018	311	77	157	11	8.99	12.99	5.36	5.58
An07-01	1.007	1.095	0.865	1.102	318	76	87	8	19.44	1.49	1.39	5.35
An07-05	1.012	1.091	0.761	1.103	357	1	87	4	10.03	1.45	1.27	5.31
An07-07	1.013	1.099	0.758	1.113	185	7	270	1	9.91	1.46	1.27	5.33
An07-08	1.012	1.078	0.725	1.091	173	2	263	9	9.54	1.69	1.43	5.31
An07-09	1.012	1.107	0.797	1.119	186	4	96	1	12.03	1.43	1.28	5.23
						AARM						
Iso07-04	1.019	1.035	0.306	1.055	282	12	179	45	70.57	57.12	45.02	-
Iso07-05	1.061	1.017	-0.545	1.079	151	7	58	21	41.03	71.96	34.14	-
Iso07-10	1.048	1.019	-0.413	1.068	171	59	81	0	39.55	64.05	30.50	-
Iso07-11	1.032	1.010	-0.527	1.042	72	32	178	24	59.09	79.71	52.03	-
Iso07-12	1.053	1.030	-0.273	1.084	2	68	213	19	38.08	55.00	26.84	-
An07-01	1.076	1.154	0.324	1.241	153	61	259	9	48.81	32.98	22.48	-
An07-05	1.073	1.167	0.372	1.252	354	60	87	2	35.14	19.80	13.40	-
An07-07	1.047	1.244	0.653	1.303	353	47	86	3	55.18	18.96	15.50	-
An07-08	1.037	1.289	0.750	1.337	3	45	272	0	66.55	20.81	18.07	-
An07-09	1.001	1.203	0.984	1.205	340	47	93	20	87.94	13.74	13.63	-

[a] eXX values are angular uncertainties for orientations of ellipsoid principal axes.

Table 4.4: Post-deformation remanence component orientations determined by principal component analysis.

Sample	Strain	Dec.	Inc.	Dec.	Inc.
			Soft	*Hard*	
Iso07-04	1	45	-14		
Iso07-05	1	105	-63	252	-88
Iso07-10	1.5	38	-24	6	-72
Iso07-11	0.3	74	-54	277	-80
Iso07-12	0.6	311	-55	36	-78
		main component			
An07-01	0.3	56	-79		
An07-04	1	238	-46		
An07-05	0.6	248	-77		
An07-07	1.3	156	-57		
An07-08	1.5	162	-38		
An07-09	1	178	-80		

Table 4.5: Magnetic fabric parameters, changes in anisotropy, and orientations of ellipsoid principal axes for deformed samples.

Sample	strain	F	T	P_0	P_f	ΔP	T	Dec. K_{max}	Inc. K_{max}	Dec. K_{min}	Inc. K_{min}
					AMS						
Iso07-11	0.3	1.029	1.006	1.02	1.035	0.015	0.674	55	6	270	83
Iso07-12	0.6	1.051	1.021	1.018	1.073	0.055	0.396	36	8	248	80
Iso07-04	1	1.077	1.013	1.037	1.091	0.054	0.679	142	16	288	72
Iso07-05	1	1.046	1.02	1.04	1.067	0.026	0.387	75	31	258	59
Iso07-10	1.5	1.136	1.032	1.011	1.172	0.162	0.604	84	19	269	70
An07-01	0.3	1.051	1.036	1.102	1.093	-0.009	0.121	98	2	101	7
An07-05	0.6	1.029	1.041	1.103	1.071	-0.032	-0.163	171	3	261	6
An07-09	1	1.037	1.048	1.119	1.086	-0.033	-0.124	2	1	272	1
An07-07	1.3	1.114	1.022	1.113	1.139	0.026	0.661	180	12	278	34
An07-08	1.5	1.188	1.06	1.091	1.26	0.168	0.492	9	0	-82	55
					AARM						
Iso07-11	0.3	1.028	1.053	1.055	1.082	0.028	-0.271	23	27	202	60
Iso07-12	0.6	1.168	1.027	1.167	1.199	0.032	0.684	6	10	136	73
Iso07-04	1	1.327	1.042	1.069	1.383	0.314	0.75	89	24	263	66
Iso07-05	1	1.159	1.058	1.042	1.226	0.185	0.448	106	24	244	60
Iso07-10	1.5	1.321	1.275	1.084	1.684	0.6	0.063	90	22	267	68
An07-01	0.3	1.199	1.077	1.241	1.291	0.05	0.39	182	5	91	1
An07-05	0.6	1.139	1.124	1.252	1.275	0.023	0.109	181	10	277	29
An07-09	1	1.101	1.067	1.205	1.175	-0.03	-0.197	161	21	271	42
An07-07	1.3	1.375	1.093	1.303	1.497	0.194	0.572	41	26	275	45
An07-08	1.5	1.913	1.268	–	2.425	–	0.464	6	1	272	56
					AIRM						
Iso07-11	0.3	1.014	1.038	–	1.052	–	-0.451	76	28	230	58
Iso07-12	0.6	1.071	1.031	–	1.104	–	0.386	302	15	54	75
Iso07-05	1	1.093	1.041	–	1.138	–	0.372	84	30	264	60
Iso07-04	1	1.008	1.101	–	1.11	–	-0.851	83	32	269	58
Iso07-10	1.5	1.129	1.129	–	1.275	–	-0.002	86	22	260	68

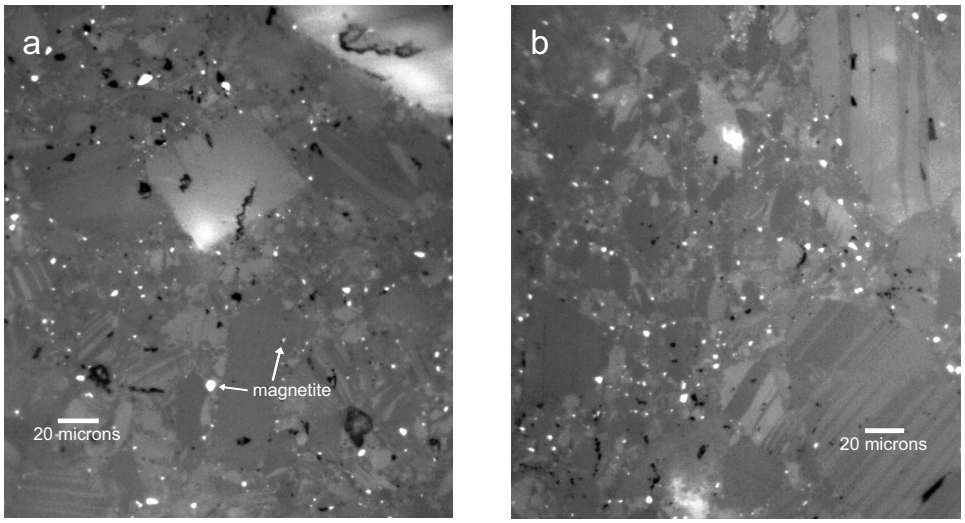

Figure 4.1: Reflected light photomicrograph of the spatial distribution of magnetite grains in the calcite matrix for: a) a typical sample after HIP, and b) a deformed sample. The small dark spots in the image are pits in the sample surface.

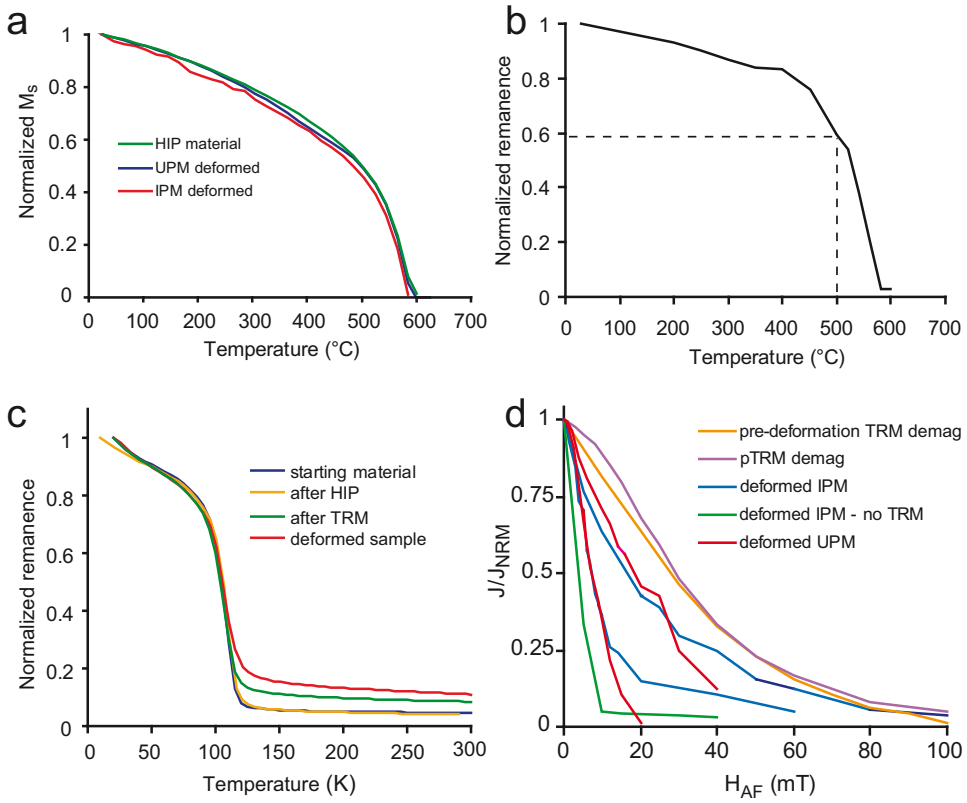

Figure 4.2: Magnetization properties: a) comparison of M_s(T) curves with Curie temperatures for samples after HIP and after deformation; b) stepwise thermal demagnetization of a 0.1 mT TRM given to a test sample of post-HIP material; c) low-temperature warming curves of an SIRM given after field-cooling; and d) AF demagnetization spectra of pre-deformation TRM or post-deformation "NRM" for various samples.

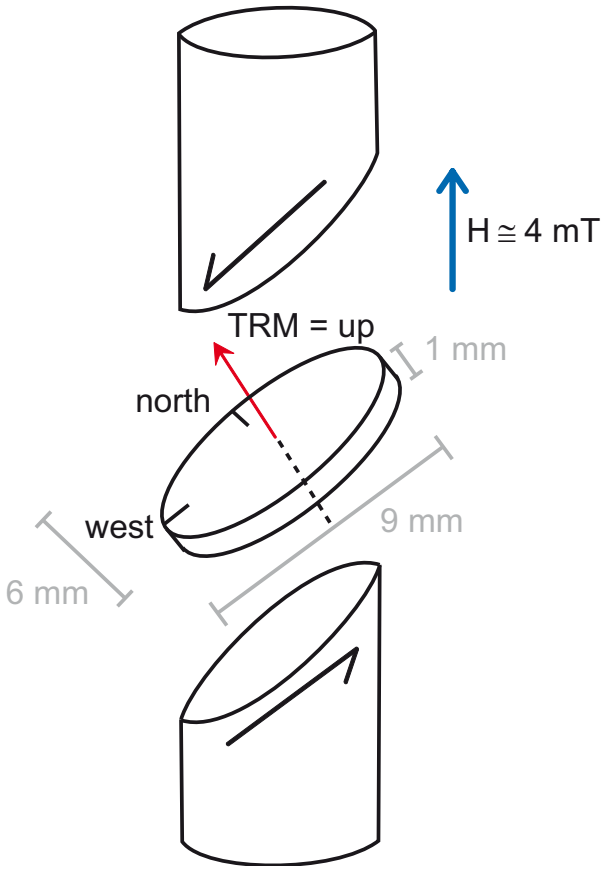

Figure 4.3: Schematic diagram of sample coordinate scheme in relation to shear geometry and field direction from furnace heating coils during experiments.

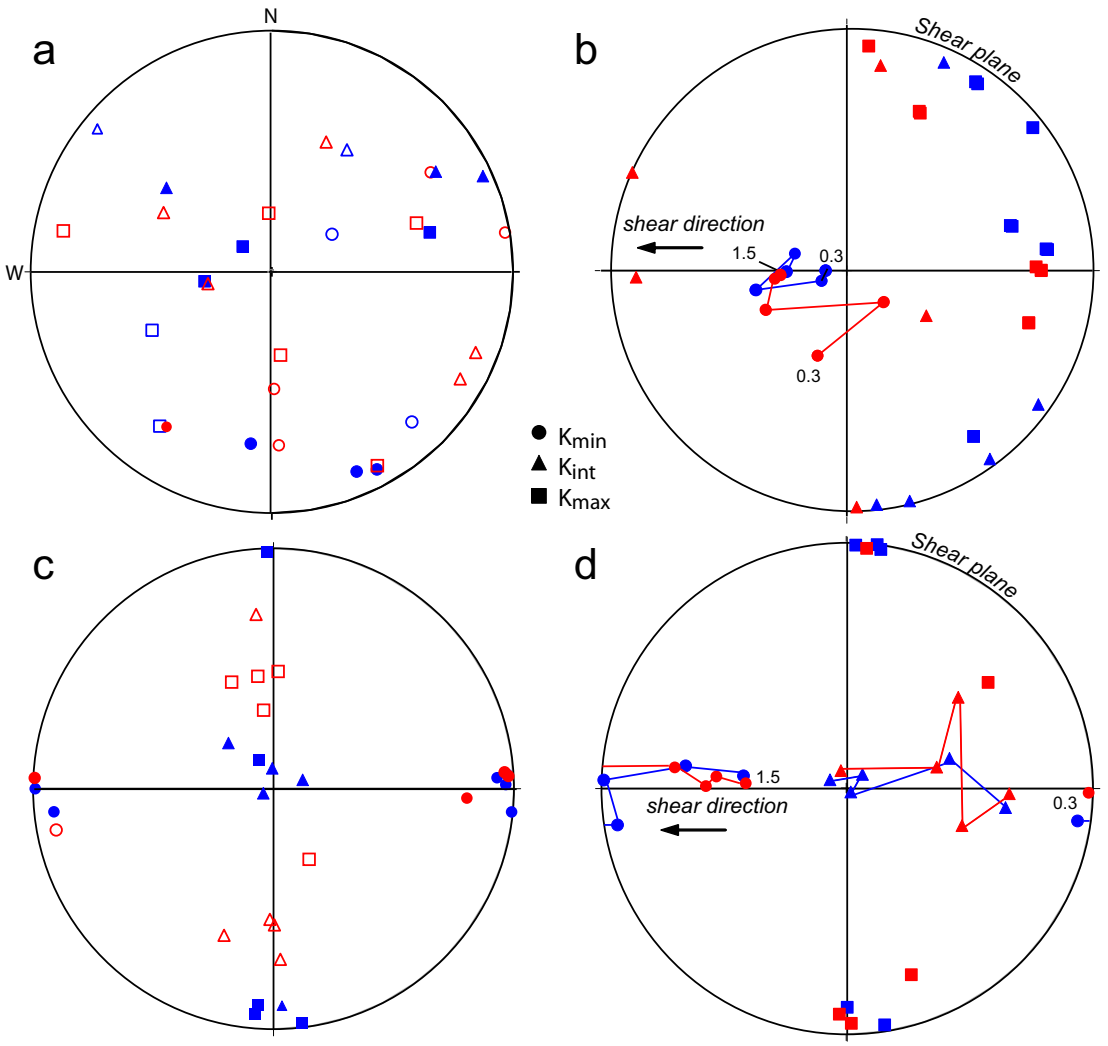

Figure 4.4: Stereographic plots of pre- and post-deformation magnetic fabrics. Principal directions for AMS and AARM are shown in blue and red, respectively. Left-hand figures are pre-deformation fabric for: a) IPM and c) UPM samples. Open symbols represent directions that are not statistically significant. Deformation fabrics are shown in b) and d) for corresponding samples which are labeled with highest and lowest strains. All plots are lower hemisphere equal-area projections; sense of shear for b) and d) is top to the west.

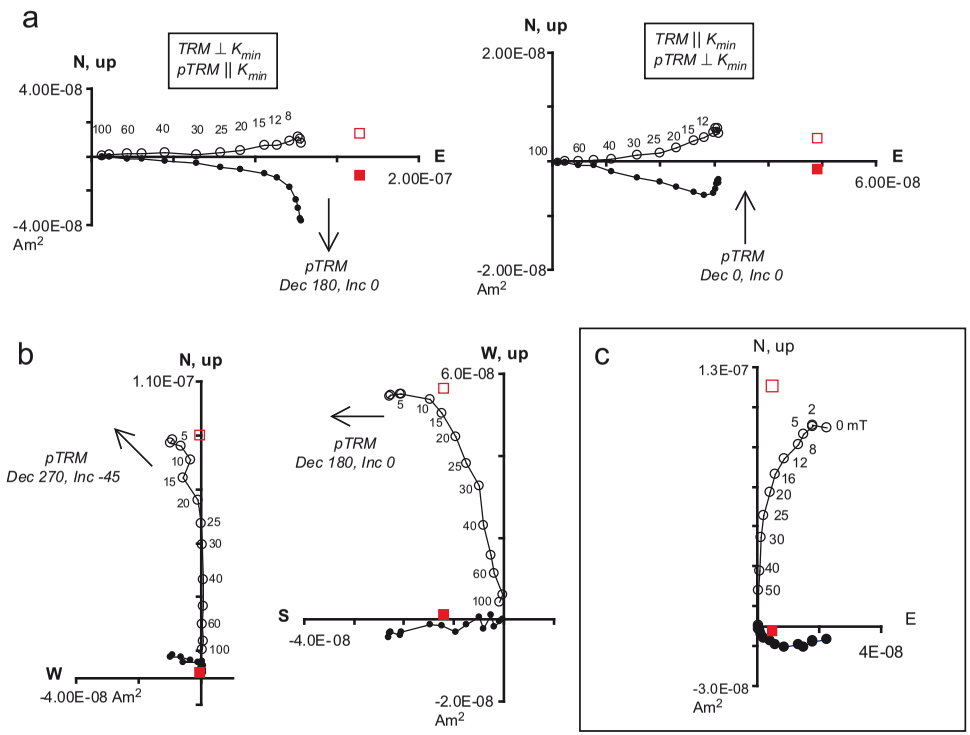

Figure 4.5: Orthogonal vector component Zijderveld (1967) diagrams with results of pTRM acquisition and demagnetization experiments for: a) UPM test samples, b) IPM test samples, and c) remagnetization of a test sample by reheating in the deformation vessel. Open symbols are projections onto the vertical plane, solid symbols are projections onto the horizontal plane, and initial total TRM vectors are shown in red. Points are labeled with peak AF field steps in mT.

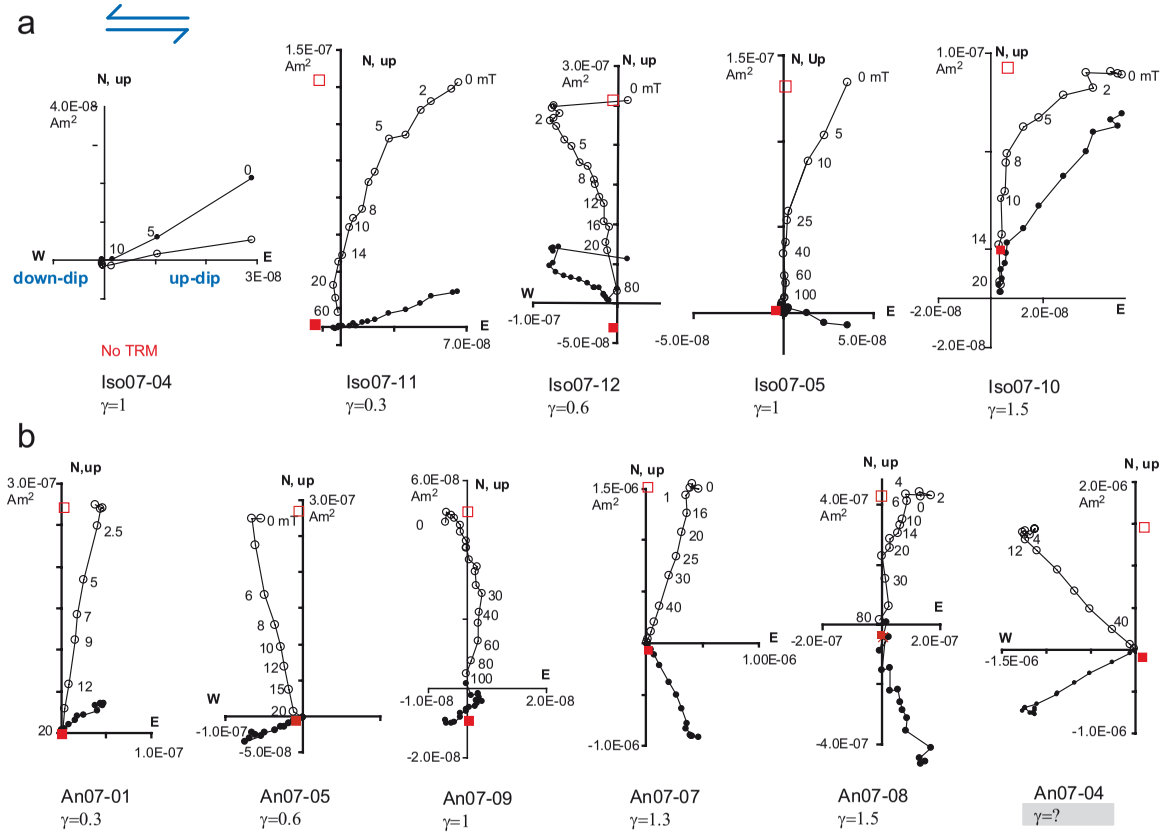

Figure 4.6: Zijderveld (1967) diagrams of remanence behavior during AF demagnetization for: a) deformed IPM, and b) deformed UPM samples. Symbols are the same as in Figure 4.5. Orientations of pre-deformation TRM vectors are shown as red squares and have been normalized to the post-deformation intensity values, therefore relative pre-deformation remanence intensity is not reflected in this figure. Please refer to Figure 4.8c for relative remanence intensity data.

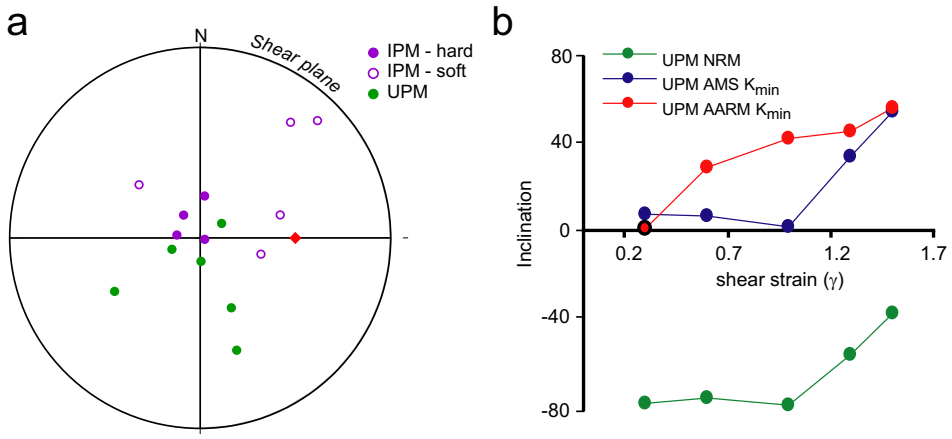

Figure 4.7: a) Upper hemisphere equal-area stereographic projection of orientations of post-deformation "NRM" components determined by principal component analysis (see Table 4.4). The red diamond indicates the orientation of the ambient field during deformation, which is coaxial with the maximum compressive stress direction. b) Comparison of vertical rotation of AMS minimum axes in deformed UPM samples with vertical deflection of remanence directions.

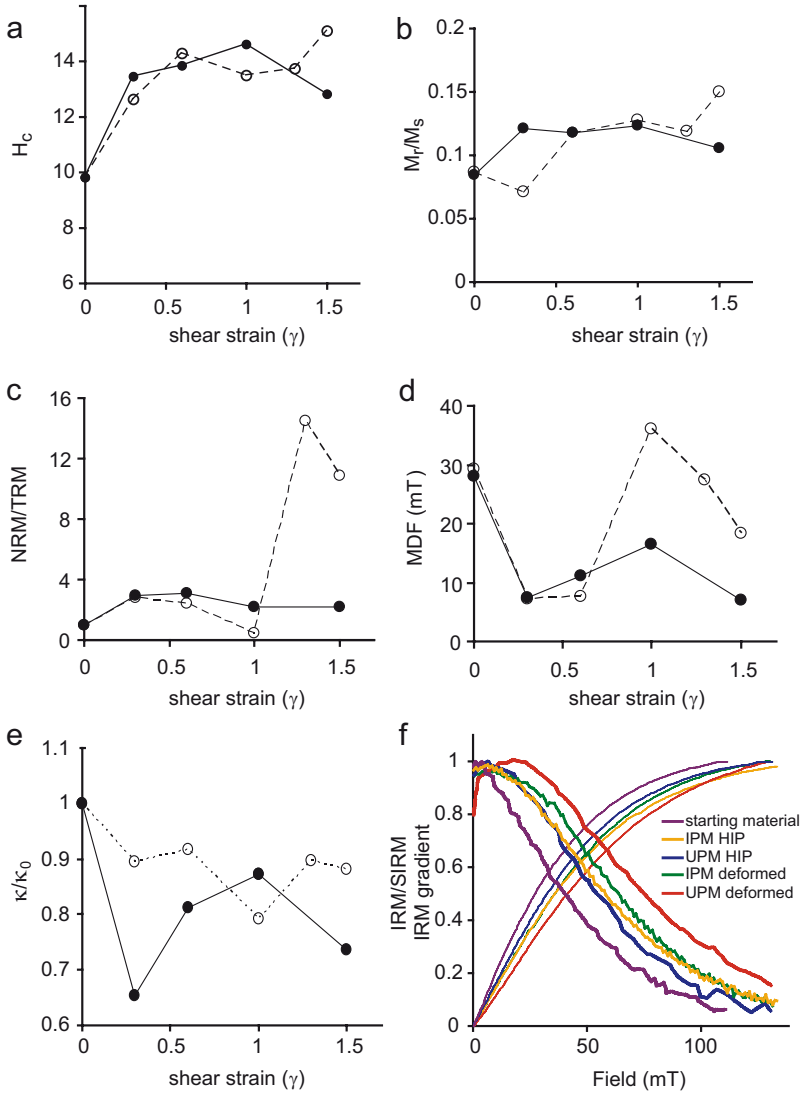

Figure 4.8: a)-d) Changes in hysteresis and remanence properties after deformation relative to pre-deformation values. Solid (open) symbols represent IPM (UPM) samples. e) Changes in bulk susceptibility after deformation. f) Normalized IRM acquisition curves (thin lines) and gradients of acquisition curves (heavy lines) from FORC measurements.

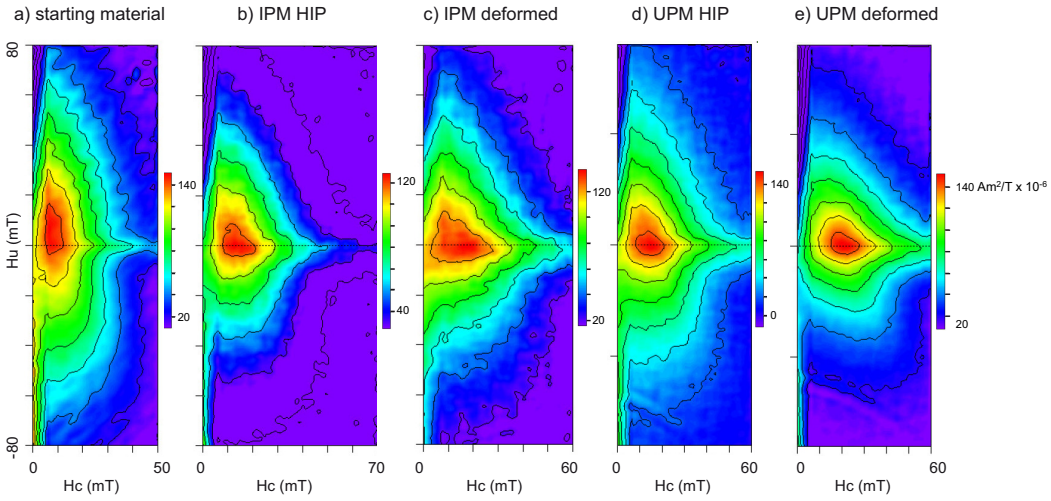

Figure 4.9: Comparison of FORC measurements for starting material, HIP material, and deformed samples. Smoothing factor (SF) = 10 for c) and SF = 8 for a), b), d) and e).

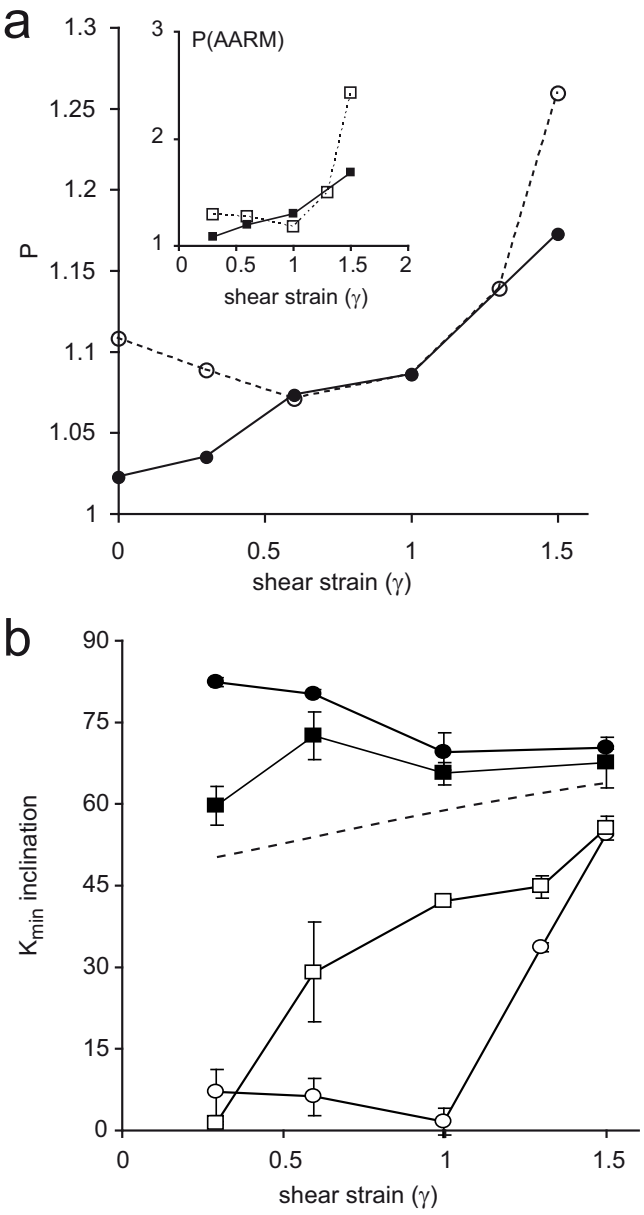

Figure 4.10: Changes in a) degree of anisotropy and b) orientation of poles to magnetic foliation. Data points are averages over several measurements, and error bars are standard deviations. Solid (open) symbols represent data from IPM (UPM) samples and circles (squares) represent AMS (AARM) data. The dashed line in b) represents the rotation of the minimum stretching axis of the theoretical strain ellipsoid.

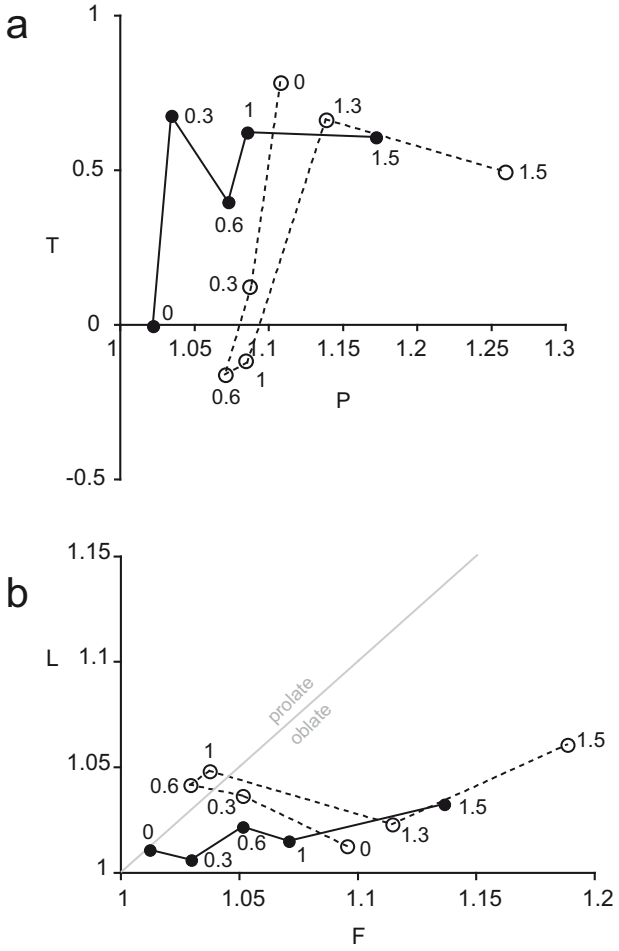

Figure 4.11: Changes in magnetic fabric shape parameters. a) Shape parameter T versus degree of anisotropy P. b) Modified Flinn plot of shape change in magnetic fabric ellipsoid. Solid (open) symbols represent data from IPM (UPM) samples. Points are labeled in increments of shear strain.

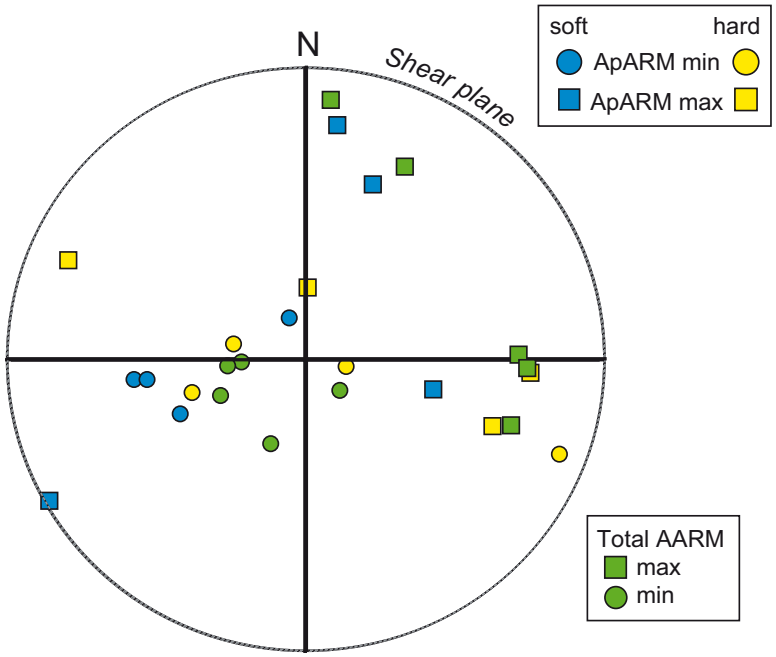

Figure 4.12: Lower hemisphere stereographic projection of maximum and minimum directions of anisotropy of partial ARM imparted to high-coercivity (H_c >10 mT) and low-coercivity (H_c <10 mT) magnetic fractions compared with total ARM fabrics of deformed IPM samples.

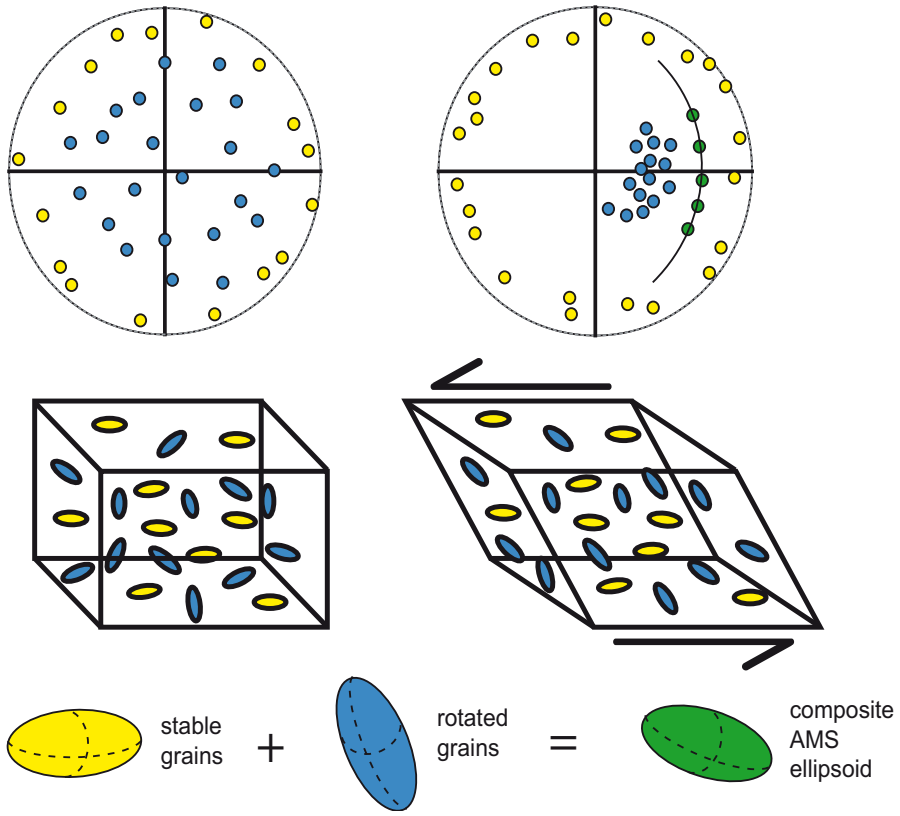

Figure 4.13: Conceptual model of theorized grain rotation behavior in IPM samples, illustrating how a composite magnetic fabric may arise out of complex grain rotation behavior during deformation. The idealized steroplots at top represent K_{max} directions of individual grains.

Chapter 5

High-Temperature Magnetic Fabric in Experimental Shear Zones: Implications for Magnetite Rheology

Magnetic fabric development has been studied in synthetic magnetite-silicate aggregates in a series of high-temperature simple shear deformation experiments. Samples composed of magnetite grains with a nominal size of 20-40 μm dispersed at 3wt% in a matrix of plagioclase were deformed between 1000 and 1200°C with a confining pressure of 300 MPa, differential stresses in the range 10-120 MPa, and shear strains up to γ=3. We determined that both magnetite and plagioclase were deformed plastically at these conditions. An oblate magnetic fabric ellipsoid develops subparallel to the shear plane and the degree of AMS rapidly increases with strain up to a value of 2.5. Theoretical strain response models of magnetic fabric development were applied to the data to obtain estimated magnetite strains. The shape-preferred orientation of magnetite grains after deformation, determined from reflected light image analysis, was used to calculate independent magnetite strain estimates. These results were then compared with strains estimated from theoretical magnetic anisotropy development. Both strain estimation methods indicate strain partitioning between magnetite and the plagioclase matrix and

the results are used to determine approximate viscosity ratios between the two phases at the experimental conditions.

5.1 Introduction

Magnetic anisotropy methods are a valuable microstructural guide in field studies of deformed rocks. Information about relative strain provided by this technique is particularly useful in zones of high strain or extensive metamorphism where physical strain markers are typically absent, including shear zones or zones with very subtle degrees of subsolidus deformation where no macroscopic fabric is visible. Experimental work to understand how magnetic minerals respond to strain in the laboratory is essential in trying to understand how deformation histories may be reflected in magnetic signatures of deformed rocks in nature. If it is possible to determine a laboratory relationship between strain and magnetic properties, particularly magnetic anisotropy, our interpretation of tectonic conditions through the use of magnetic fabric analysis may be vastly improved.

Although models exist to predict the changes in magnetic anisotropy that occur in response to plastic strain in magnetite (Owens, 1974; Hrouda, 1993), these models are seldom applied to field studies of magnetic fabrics in high strain zones. More attention has been given to settings in which magnetite is assumed to deform as a rigid marker, with the focus of study placed on determining active vs passive rotation behavior. Additionally, as an accessory mineral, magnetite exerts little control on bulk rock rheology and its general deformation behavior in field settings is often difficult to determine. Nevertheless, deformed magnetite has been documented in several crustal shear zones (Housen et al., 1995; Mamtani et al., 2007; Barbosa & Lagoeiro, 2010), and its occurrence in locally high concentrations in the oceanic crust is strongly associated with strain localization in oceanic core complexes (Agar & Lloyd, 1997; Natland, 2002). Because rheological behavior of magnetite under both laboratory and natural conditions is somewhat poorly constrained it is difficult to identify the thermotectonic settings in which magnetite is likely to deform in the ductile regime. Controlled laboratory experiments to characterize the magnetic anisotropy signal of plastically deformed magnetite are therefor necessary to interpret Fe-oxide mineral strain responses from

magnetic fabric data in deformed rocks.

We present magnetic fabric results from high-temperature shear experiments on synthetic magnetite-silicate aggregates to study the changes in magnetic anisotropy that result from deformation of magnetite under ductile conditions. This study takes unique advantage of the existing models of theoretical magnetic anisotropy development in deforming rocks and illustrates the potential for extracting semi-quantitative strain data from magnetic fabrics under certain circumstances.

5.2 Experimental Methods

5.2.1 Sample Synthesis

Sample materials consisted of 3 wt% synthetic Wright 41183 magnetite in a matrix of natural labradorite from the Beaver Bay anorthosite with a plagioclase composition of approximately An_{70}. The magnetite used is multi-domain (MD) with a mean grain size around 20 μm and a mean aspect ratio of 1.6 (Yu et al., 2002). This is a typical degree of grain elongation for natural magnetite in igneous rocks (Stacey & Banerjee, 1974). The plagioclase matrix material was sieved to remove the coarse-grained fraction above 64 μm and then washed in HCl to remove traces of metallic Fe impurities. After washing in acid, the starting plagioclase is nearly purely diamagnetic in hysteresis measurements. Sample powders were mixed thoroughly by hand and then magnetically characterized by measuring hysteresis loops and low-temperature remanence curves. Mixed sample powders were cold-pressed at 130 MPa in a hydraulic oil-medium isostatic press and fitted into oxidized Ni canisters. Samples were isostatically hot-pressed in an Ar gas-medium Paterson pressure vessel at 300 MPa and 1200°C. Magnetic properties were measured before and after hot isostatic pressing (HIP), as described below.

During the synthesis of several trial samples, a large extent of reaction occurred between the magnetite and the plagioclase matrix. This was primarily indicated by large drops in saturation magnetization (M_s) and was confirmed by microscopic analysis. One partially-reacted sample was analyzed with Raman spectroscopy, which indicated fayalite as the primary phase in reaction rims surrounding magnetite grains. The occurrence of this reaction was interpreted to result from a failure to maintain the

oxygen fugacity of the sample above the quartz-fayalite-magnetite buffer. This problem was ultimately addressed by oxidizing the Ni canisters prior to hot-pressing and by packing small amounts of hematite (Fe_2O_3) powder in the ends of the capsule between the sample pellet and the canister end-caps. The regions of sample material near the canister ends were avoided when samples were made from the hot-pressed material.

5.2.2 Deformation and Characterization Procedures

After hot-pressing, all metallic material from the Ni canister was removed from the sample by cutting and grinding and the sample material was cut into discs of 1 mm thickness. Rock magnetic analysis was performed on synthesized samples along with quantitative compositional analysis using an electron microprobe. Rock magnetic properties measured before and after deformation on all samples include anisotropy of magnetic susceptibility (AMS), anisotropy of anhysteretic remanence (AARM), hysteresis loops, backfield remanence curves, Curie temperature (T_c) measurements, and low-temperature (T<0°C) saturation remanence curves. AMS and T_c measurements were made on a KLY-2 KappaBridge susceptibility meter. Hysteresis loops and backfield remanence curves were measured on a Princeton Measurements MicroMag vibrating sample magnetometer (VSM) using a saturating field of 1.0 T. Low-temperature measurements were made on a Quantum Designs Magnetic Properties Measurement System (MPMS) and included field-cooled and zero-field-cooled saturation isothermal remanent magnetization (SIRM) warming curves and room-temperature SIRM cooling and warming curves using a saturating field of 2.5 T. AARM was measured on a 2G superconducting rock magnetometer. ARMs for remanence anisotropy were given in a maximum alternating field of 100 mT with a biasing field of 0.1 mT. The shape parameter T ($T = [ln(F) - ln(L)]/[ln(F) + ln(L)]$) and corrected degree of anisotropy P_j of (Jelinek, 1981) were used to describe magnetic fabric shape and intensity, along with the parameters of magnetic lineation L ($L = K_{max}/K_{int}$) and magnetic foliation F ($F = K_{int}/K_{min}$).

Deformation experiment procedures followed those of Till et al. (2010). Sample discs were shaped to fit the elliptical cross-section of a piston formed from alumina rod of diameter 5 mm cut at a 45° angle. The alumina pistons and sample discs were enclosed in an oxidized Ni jacket. The NiO layer on the interior surface of this jacket,

produced by heating the jackets in air for several hours, maintains the oxygen fugacity near the Ni-NiO buffer during deformation. The full sample assembly includes larger alumina and zirconia pistons on either side of the small angled pistons, all of which were enclosed in a thin Fe jacket. See Hustoft & Kohlstedt (2006) for a schematic sample assembly diagram. Experiments were performed in a triaxial gas-medium pressure vessel (Paterson, 1990) using Ar as a pressure medium at temperatures of 1000°, 1100° or 1200°C. Samples were deformed under confining pressure of 300 MPa and at constant piston displacement rate, approximating constant strain rates in the range $1x10^{-4}$ s^{-1} to shear strains in the range γ=1-3. Conditions for individual experiments are shown in Table 6.2.

5.3 Changes in Rock Magnetic Properties

5.3.1 Initial Sample Characteristics

Significant changes in rock magnetic properties occurred in samples after hot-pressing due to chemical exchange between the matrix plagioclase and magnetite grains resulting in large changes in magnetite composition. Electron microprobe analysis of the synthesized samples showed that opaque grains are Fe-oxides containing approximately 5 wt% Al (Figure 5.1). Microprobe analysis also revealed that the oxide grains are surrounded by rims composed of Al-Ca-Na-silicate which are depleted in Al and Ca but enriched in Si and Na relative to the silicate matrix. These rims are not visible in reflected light microscopy and may be plagioclase of a more albite-rich composition (Table 6.1). Electron microprobe analysis on oxide grains in selected samples was repeated after deformation and showed that further compositional changes were minor in most samples, although the Al content of oxide grains deformed at 1200°C is slightly higher than after lower-T experiments.

The post-synthesis changes in magnetic properties are summarized in Table 5.2. The most prominent change is a large drop in M_s after hot-pressing from a starting value of 86 Am^2/kg for the pure magnetite to 36 Am^2/kg for the hot-pressed magnetite. Thermomagnetic susceptibility curves indicate a Curie temperature (T_c) near 500°C and low-temperature saturation remanence curves showed no Verwey transition, suppression of which has been previously noted as an effect of cation-substitution in magnetite (e.g.

Dunlop & Özdemir, 1997, Ch. 3.5). Bulk susceptibility decreased by approximately 50% after HIP. The cation-substituted Fe-oxide lies in the magnetite-hercynite solid solution with a composition around x=0.4 according to the formula $Al_xFe_{3-x}O_4$ where x=0 for pure magnetite and x=2 for hercynite. This composition is close to the value of x=0.35 predicted for a Curie temperature of 500°C based on magnetic property measurements of Al-bearing magnetite by Pickart & Turnock (1959). The decrease in M_s is consistent with that predicted for a composition in the range x=0.4-0.5 for Al^{3+} replacement of Fe^{3+} on B-sites (Pickart & Turnock, 1959). However, this oxide phase will be loosely referred to as magnetite throughout the paper for simplicity.

5.3.2 Rock Magnetic Properties After Deformation

Changes in Curie temperature, hysteresis properties and bulk susceptibility after deformation are varied among samples, reflecting various degrees of the continued cation-exchange reaction between the magnetite and the matrix in each experiment. Post-deformation Curie temperatures decreased slightly in all samples relative to the average value near 500°C in HIP material, but the magnitude of the decrease varied significantly between experiments (Table 5.2). Measurements of low-field susceptibility vs. temperature up to 600°C indicate small amounts of a second phase with a T_c near 355°C after deformation in some samples (Figure 5.2). This corresponds to the T_c of metallic Ni, indicating that traces of material from the Ni jacket were not entirely removed during sample recovery. However, in thermomagnetic measurements of saturation magnetization, M_s, the magnitude of the drop in M_s at 355°C indicates that the Ni contributes no more than 5% of the room temperature M_s and thus the Ni contribution to remanence properties is minor.

Sample hysteresis properties after deformation are significantly varied and complex. M_s is approximately 50% higher in half of deformed samples and is lowered in the rest. Decreases in M_s after deformation in samples 011-06 and 011-08 are thought to represent further cation-exchange between the magnetite and the matrix at 1200°. The lower M_s in sample 011-04 may reflect partial reaction of the type observed in several trial synthesis runs due to failure to maintain oxygen fugacity. Because this experiment had a longer duration than the others, it is possible that the buffer layer was consumed and conditions in the deformation vessel became too reducing for magnetite stability. If

Al content in magnetite in HIPed samples represents a quasi-equilibrium concentration at 1200°C, increases in M_s after deformation at 1000° and 1100°C could indicate lower miscibility of Al in magnetite and reduced Al substitution at these temperatures.

Bulk coercivity is generally higher after deformation and this increase is highest in sample 011-05, which was subjected to the highest differential stress during the deformation and has a coercivity over double that of the undeformed HIP material. Samples 011-02 and 011-03, deformed at 1100 °C, show a significant increase in H_c over the HIP value, while samples deformed at 1200 °C show a more modest increase. Bulk susceptibility, χ_0, is lower in all samples after deformation, in accordance with findings from previous experimental deformation studies (Borradaile, 1996; Jackson et al., 1993; Till et al., 2010). Changes in χ_0 are likely a function of changes in both M_s and H_c.

Measurements of backfield remanence acquisition were made using 100 field steps up to a maximum magnetizing field of 500 mT, and the resulting remanence curves were used to perform a coercivity component unmixing analysis (Heslop et al., 2002). The method and program described in Egli (2003, 2004) was used to produce gradient plots of the remanence curves and to find the coercivity distributions that produced the best fit to the measured data. The results of the unmixing analysis are shown in Figure 5.4. Undeformed HIP samples contain a dominant component with a median destructive field (MDF) around 33 mT, but a higher-coercivity component with a MDF of 135 mT is also present. Samples deformed at 1200°C clearly show this secondary high-coercivity phase, which appears to carry a large proportion of the total remanence compared to the softer component, but it is absent for the sample deformed at 1000°C and only shows up as a minor component in two samples deformed at 1100°C. The MDF of the main component is systematically higher for samples subjected to the highest differential stresses during deformation and significantly lower for samples deformed at 1200°C under relatively low stresses (Table 5.2). The dispersion parameter (DP) describing the width of each component curve, is slightly smaller for deformed samples relative to the HIP material, indicating a slight narrowing of the coercivity distribution for the main magnetic phase.

The lower-coercivity phase is interpreted as the coarse-grained Al-bearing magnetite phase that contributes most of the magnetic signal in the samples. The coercivity of the hard phase is too high to be pure SD magnetite or coarse-grained aluminomagnetite. However, fine-grained Al-substituted titanomagnetites have H_c values between

166 and 185, and H_{cr} values between 204 and 223 (Özdemir & O′Reilly, 1978, 1981) for Al substitution of x=0.1 and 0.2, with higher coercivities corresponding to higher Al content. Additionally, Worm & Markert (1987) measured a coercivity near 100 mT for SD aluminomagnetite with a composition near x=0.2. The MDF values for the high coercivity component unmixed from the remanence curves are consistent with the previously measured values for fine-grained Al-substituted magnetite considering the somewhat higher levels of Al substitution in the samples. A high coercivity component of remanence carried by SD Al-magnetite grains in our samples is also consistent with the observations of a single Curie temperature in most samples. One source of fine-grained material may be the regions of magnetite grain boundaries that are frequently characterized by highly-irregular morphologies, which are apparent in scanning electron images of the magnetite grain boundaries. Grain material in these regions likely behave as SD or PSD subparticles. It is unclear why the high coercivity is more strongly expressed in some samples after deformation than in others. However, the high-coercivity component is unlikely to contribute significantly to the magnetic susceptibility of the sample, both because of a lower intrinsic susceptibility and the volumetrically insignificant quantity of this material, but it would be expected to have a disproportionately strong contribution to sample remanence, as seen in the unmixing results for several samples.

The good agreement between AMS and AARM fabric orientations and intensities for each sample suggests that the high-coercivity phase was deformed in a similar manner to the primary magnetic component and does not significantly bias the magnetic deformation fabrics in any way.

5.4 Magnetic Fabrics of Deformed Samples

Initial magnetic fabric intensities for individual HIPed samples have average AMS P values of 1.074 and the fabric ellipsoids are slightly oblate in shape. Magnetic fabric parameters for all samples before and after deformation are listed in Table 5.3. AARM fabrics show a significantly stronger degree of anisotropy with P values over 40%, probably reflecting some initial orientation of the high-coercivity, finer-grained regions on the edges of larger magnetic grains. Initial fabric ellipsoid principal directions are highly

scattered (Figure 5.3a), indicating that the starting material does not have a clear preferred direction of magnetic anisotropy given that all samples were cut from HIPed material in the same orientation. Additionally, a "site" mean AMS value taken from the averaged directions of all HIPed samples yields an anisotropy intensity of just a few percent. AMS and AARM principal directions are in relatively good agreement in most of the starting material, but some samples show a slight directional discrepancy ($\sim$15-20°), again probably due to the high-coercivity remanence component that has less influence on susceptibility measurements.

Post-deformation magnetic fabric maximum directions cluster near the shear plane in the direction of shearing, and magnetic minimum directions are sub-perpendicular to the shear plane (Figure 5.3a). The fabric orientation does not vary with either shear strain or deformation temperature. Magnetic fabric ellipsoids of deformed samples are generally oblate in shape, although sample 011-04b is triaxial. Magnetic lineations, foliations, and shape parameters are shown in Figure 5.3d. AMS fabric intensity increases monotonically with shear strain, up to P values of 2.5 (Figure 5.3b). Figure 5.3b also contains magnetic fabric data from deformed synthetic magnetite-carbonate aggregates in experiments by Till et al. (2010), which used the same synthesis and deformation procedures as in this study, but were performed at lower temperature (500°C).

Anisotropy development in the samples of Till et al. (2010) resulted from the alignment of rigidly rotating magnetite particles in a ductile matrix. The AMS intensities for deformed samples in the current study exceed those of Till et al. (2010) for equivalent shear strains by a factor of approximately 3. The more rapid development of anisotropy with strain in the current experiments strongly suggests that magnetite deforms plastically during deformation of the bulk samples and that the high degrees of AMS and AARM are due to increasing magnetite grain shape anisotropy with increasing bulk shear strain. Although the magnetic particles used in experiments of Till et al. (2010) were finer-grained (1-2 μm) and purer in composition, we estimate that the intrinsic susceptibilities of the magnetic phases used in these two sets of experiments are similar and therefore the differences in anisotropy development primarily reflect the different responses of magnetic particles to deformation (crystal plastic vs. rigid behavior). Additionally, microstructural examination of magnetite grains after deformation revealed the presence of low-angle subgrain boundaries in several samples, confirming

that plastic deformation mechanisms are active in magnetite during the experiments (Chapter 5).

5.4.1 Temperature Dependence of Anisotropy

Figure 5.3c is a comparison of AMS intensity for three samples deformed to shear strains of γ=1 at different temperatures in which a significant dependence of magnetic fabric strength on temperature is evident. For both AMS and AARM measurements (Table 5.3) a sample deformed at 1200°C has a degree of anisotropy approximately 15% higher than a sample deformed to the same strain at 1000°C. Differences in experimental strain rates between these samples are small and are unlikely to account for the difference in anisotropy strength. However, the difference in applied stresses at each temperature to maintain similar strain rates reflects the changing viscosity of the plagioclase matrix with temperature. The observed temperature dependence of magnetic anisotropy is only possible if magnetite deforms plastically, with higher magnetite strain rates at higher temperatures, but at overall lower strain rates than that of the plagioclase. Magnetite in our experiments therefore does not deform as a perfect passive marker, i.e., as a particle with no viscosity contrast with the matrix.

5.4.2 Comparison to Field Studies

To determine whether the magnetic fabric intensities produced in our experiments are representative of anisotropy values in deformed rocks in nature, we compared our experimental fabrics with previously reported AMS measurements for two high-grade shear zones for which strain estimates were made. AMS P values for samples from the 1100°C experiments are shown in comparison to field study data in Figure 5.5. Housen et al. (1995) documented deformed magnetite in highly strained anorthosites in the Parry Sound Shear Zone (PSSZ), Ontario, and established a correlation between strain and magnetic fabric strength, noting that fabric strength progressively increased from protolith to mylonite to ultramylonite. This study determined that magnetite deformed plastically in the mylonitic zones. Although the main components of the anorthites in the PSSZ are similar in composition to our synthetic samples, the fabric development is much more rapid in experimentally deformed samples. This discrepancy may be partly

due to a higher viscosity contrast and different strain partitioning between magnetite and silicates at the lower temperatures and geologic strain rates of the PSSZ compared to the experimental conditions, resulting in different strain in magnetite grains for samples with the same bulk strain. Alternatively, minor differences in grain size and composition of the magnetite, and thus intrinsic susceptibility, may also control the different rates of anisotropy development between the two sets of samples.

Ruf et al. (1988) also reported AMS intensities associated with estimated strains for a granitoid mylonite in the Santa Catalina Core Complex (SCCC) mylonite zone. Figure 5.5 shows that the degree of AMS for experimentally deformed samples overlaps with the strongest fabrics from the SCCC. However, Ruf et al. (1988) did not conclusively determine that magnetite was plastically deformed in the mylonite and this may account for the scatter in their measured fabric strengths as a function of strain and the overall lower anisotropy. On the basis of this brief comparison with the above field studies, the magnetic anisotropies produced by experimental deformation broadly appear to be reasonable values for high-strain zones in nature.

5.5 Theoretical Models of AMS Development

Theoretical calculations of AMS development as a function of strain are generally categorized into four types of strain response. The passive model as defined by Owens (1974) describes deformation of magnetic grains that have no viscosity contrast with the matrix, whereby magnetic grains undergo internal strain at the same rate as the matrix. Confusingly, descriptions of the rotation of rigid magnetic grains that do not undergo internal strain are sometimes referred to as either passive rotation or active rotation (termed line/plane and viscous models, respectively by Owens (1974)). Hrouda & Lanza (1989) also introduced the ductile model, describing the deformation of magnetic particles undergoing internal strain at a reduced rate with respect to the deforming matrix, due to higher viscosity of the magnetic particles.

Since a strong magnetic fabric is developed quickly with respect to both the lower-temperature experiments of Till et al. (2010) (Figure 5.3b) and to natural shear zones where plastically-deformed magnetite has been documented (Figure 5.5) it is unlikely that the strain-response of magnetite during the experiments is one of rigid

rotation. Calculated development of anisotropy with strain in rigid particle rotation models indicate that alignment of magnetite particles with an initial aspect ratio of 1.5 begins to plateau near shear strains over γ=7, at P values around 1.35 (Hrouda, 1993, Fig. 6a). Since the mean aspect ratio of magnetite in the synthetic samples is close to 1.5, we may reasonably assume that increases in the degree of anisotropy beyond 1.35 must be caused by a change in magnetite grain shape, i.e. plastic deformation of the magnetite.

The strain-partitioning indicated by the temperature-dependence of AMS strength also rules out the passive model as an appropriate description of the strain-response of magnetite in the samples. Since magnetite appears to have been deformed at a lower strain rate than the plagioclase, a version of the ductile model should be able to adequately describe the relationship between the observed anisotropy and magnetite strain in the experiments.

The absence of passive marker behavior in deforming magnetite in our experiments is in accordance with the interpretations of Hrouda (1993), who determined that the calculated magnetic anisotropy arising from passive marker deformation of magnetite was unrealistically high when compared to the range of P values actually measured in typical metamorphic rocks. This observation may be interpreted as suggesting that typical metamorphic conditions are not conducive to high strain rates in magnetite relative to strain in other rock-forming minerals. If the passive marker model represents a relatively uncommon strain response, then strain partitioning between oxides and silicates, and therefore AMS development according to the ductile model, may be the dominant mode of magnetite deformation in high strain zones.

5.5.1 Intrinsic Susceptibility

It is apparent from the calculations of AMS development in Hrouda (1993) that the modeled outcome of AMS intensity is highly sensitive to the value of intrinsic susceptibility, χ_i, chosen for magnetite, with lower values of χ_i resulting in slower anisotropy development (Figure 5.6a). The implication of this is that in inverting the problem, i.e., attempting to estimate a strain value from a particular AMS intensity, strains will be overestimated if the chosen value of χ_i is too low. Intrinsic susceptibility is related to

the measured bulk susceptibility, χ_0, by:

$$\chi_0 = \frac{\chi_i}{(1 + N\chi_i)} \tag{5.1}$$

where N is the demagnetizing factor (Uyeda et al., 1963). This presents a problem in our attempt to apply models of AMS development to our samples, since very few methods exist for measuring χ_i in a bulk specimen. The method of Hodych (1986) to determine χ_i using low-temperature hysteresis properties yielded unsatisfactory results since coercivity increases rather than decreases at lower temperatures for the aluminomagnetite in our samples.

Intrinsic susceptibility in magnetic particles is a function of grain size (Stacey & Banerjee, 1974), composition (O′Reilly, 1984) and probably also depends on the stress state of the grains, since high defect concentrations will lower domain wall mobility and will inhibit the magnetization response to an applied field. In addition, an empirical inverse relationship between H_c and χ_i has been noted (Stacey & Banerjee, 1974).

Hrouda (1993) reported χ_i values from published estimates for MD magnetite between 6 and 21 SI, while Jackson et al. (1998) calculated values as high as 61 SI for large MD grains of nearly pure magnetite. Several studies have suggested that for magnetite χ_i should be inversely proportional to H_c in the form $\chi_i \propto k/H_c$ where k is constant (Stacey & Banerjee, 1974; Dunlop, 1984; Hodych, 1986). Stacey & Banerjee (1974) suggested a proportionality constant of 56.25 SI (45 c.g.s.) if H_c is given in mT. A coercivity near 4 mT for the HIPed samples before deformation gives χ_i near 14. Hodych (1986) argues that k may vary substantially from one rock to another and determined k values between 32.5 and 89.75 for a variety of rocks containing MD magnetite, which for our HIPed samples indicates χ_i approximately in the range 8-22.5 SI. We take χ_i to be 17 for the purpose of applying theoretical AMS models. However, in practice χ_i is not necessarily constant during deformation, especially if stress-induced changes in coercivity occur (Jackson et al., 1993) or as in the case of the present study, if changes in composition occur.

5.5.2 Application of AMS-Strain Models

The degree of anisotropy of magnetic susceptibility in a single grain is given by Uyeda et al. (1963):

$$P = \frac{1 + \chi_i N_b}{1 + \chi_i N_a} \tag{5.2}$$

where N_a and N_b are the demagnetizing factors along the maximum and minimum grain dimensions respectively, which give rise to the strong grain shape-dependence of P. Equations for N values along the principal directions of ellipsoids of any shape are given by Osborn (1945). The magnetic susceptibility anisotropy of an assemblage of homogeneously-strained grains is characterized by the mean magnetic anisotropy of the assemblage which in turn is equivalent to the AMS of a single grain with the same dimensions as the mean grain shape of the assemblage. Equation 5.2 was used to calculate the change in degree of AMS for a single grain with an intrinsic susceptibility of 17 and increasing shape aspect ratio to represent deformation according to the passive model (Figure 5.6). P values were calculated assuming an initially spherical grain so that the theoretical strain was defined by the grain shape. Because AMS fabrics in the deformed samples are predominantly oblate, N values for oblate spheroidal grains were used.

The AMS strength for particles with intrinsic susceptibilities of 6 and 17 SI corresponding to the passive model are plotted as a function of strain ratio, S, in Figure 5.6. S is defined as the ratio of maximum to minimum principal strains and is related to shear strain by the equation:

$$S = \sqrt{\frac{0.5(\gamma^2 + 2 + \gamma\sqrt{\gamma^2 + 4})}{0.5(\gamma^2 + 2 - \gamma\sqrt{\gamma^2 + 4})}} \tag{5.3}$$

(Ramsay & Huber, 1983, Eq. 2.7). It is evident from the temperature-dependence of magnetic fabric strength that magnetite grains do not behave as passive (low viscosity) markers during the deformation experiments, and indeed when AMS values from deformed samples are plotted as a function of bulk sample strain in Figure 5.6, it is clear that the anisotropy development in the experiments is slower than predicted by the passive model. The ductile model presented by Hrouda (1993) calculates the rate of AMS development for an assemblage of magnetic particles deforming in a matrix with

various viscosity contrasts. However, a simpler and more direct approach to determining approximate magnetite strains is to use the passive model to predict the effective magnetite strain that should produce the same degree of AMS as that measured in the deformed samples. For an intrinsic susceptibility of 17, the AMS values of samples deformed at 1100°C correspond to effective magnetite strains equal to approximately 30% of the bulk sample strains.

Because the grain shape of the starting magnetite is slightly elongated, part of the total AMS intensity probably results from alignment and rotation of magnetite particles during deformation, in addition to the contribution from plastic strain and changing grain shape anisotropy (Gay, 1968). The AMS strength resulting from alignment of rigid particles with an aspect ratio of 1.5 and an initially random distribution of orientations according to the line/plane model (Hrouda, 1993) is shown by the dashed line in Figure 5.6a. This type of strain-response alone produces weaker anisotropies than the measured AMS in our samples and it alone does not account for the observed anisotropy. To approximate the effect of rigid rotation on strain estimates made with AMS models, the theoretical degree of anisotropy from the line/plane model for the bulk shear strains in each experiment was subtracted from the measured AMS P values of deformed samples before determining effective magnetite strains from the passive model. The strains indicated by these rotation-corrected anisotropies are shown for comparison in Figure 5.7a. Although the rate of grain rotation depends on particle aspect ratios which change during deformation, we make the simplifying assumption that most of the grain alignment occurs early in the deformation experiment and only consider the rotation and alignment contribution for grains with a constant aspect ratio of 1.5.

5.6 Image Analysis

Reflected light image analysis was used to obtain direct estimates of magnetite strain by determining the change in mean magnetite grain shape and the shape-preferred orientation (SPO). These results were then compared with the magnetite strain estimates from the AMS models. Reflected light images were obtained from sample surfaces parallel to the shear direction and perpendicular to the shear plane to observe the magnetite in the shear zone cross-section, since the AMS fabrics indicate that this surface contains the

direction of maximum grain elongation. Representative photomicrographs at different strains are shown in Figure 5.7c. To compensate for the small sample size and low concentration of magnetite grains, the cross-sectional surfaces were subjected to several iterations of grinding, polishing, and image acquisition to provide an adequate number of magnetite grains for image analysis (at least 200 grains per sample).

The program *SPO* (Launeau & Robin, 1996) was used to calculate a mean grain orientation and a mean grain shape (aspect ratio) which was taken as an estimate of the magnetite strain ratio, S. Because the magnetite grains are well dispersed in the samples and it is therefore easy to isolate individual grain shapes in reflected light images, we used the inertia tensor calculation in the *SPO* program to determine the average magnetite grain shape and orientation for all deformed samples and one undeformed sample. The inertia tensor method has the advantage of weighting individual grains by area. For this reason, Launeau & Cruden (1998) found that the grain shape ellipsoid of the inertia tensor for magnetite grains gave better agreement with AMS data than ellipsoids determined by the intercept method.

SPO intensity increases monotonically as a function of bulk shear strain (Figure 5.7a). The temperature-dependence of AMS intensity is mirrored in the pattern of SPO vs. deformation temperature for samples deformed to identical strains (Figure 5.7b). As with the AMS measurements, the SPO of undeformed HIP material has a weak, but measurable fabric. In all samples, the SPO results give magnetite grain shape anisotropies that are significantly less than the strain ratios of the bulk samples. This is consistent with the interpretation of strain partitioning determined above from analysis of AMS data.

5.7 Discussion

Magnetite strain estimates from SPO data are lower than those made using AMS-strain models assuming plastic deformation without rotation for all samples. Attempting to correct for particle rotation in the AMS models results in magnetite strain estimates that are much lower than the other estimate methods for γ=1, but slightly higher than the SPO estimates for higher strains. Since the development of a magnetite SPO will be affected by particle rotation during strain in the same way as the magnetic fabric,

it qualitatively appears that the rotation correction performed here is not valid at low strains (γ=1). More focused experimental work on the behavior of magnetite during deformation involving strain partitioning with silicates is needed to understand the rotational contribution to shape-preferred orientation of semi-rigid particles.

In comparing the SPO results with the AMS data, a limitation of the image analysis is that the grain population sampled is restricted to a single plane and samples a limited number of grains, while AMS integrates the anisotropy signal from every grain in the sample and provides information in three dimensions. Other causes of discrepancy between the strain estimate methods are that the estimate of 17 SI for χ_i may be too low and it is likely that χ_i varies somewhat from one sample to another, and changes slightly during deformation.

Rheological descriptions of strain partitioning (Handy, 1990; Tullis et al., 1991; Vigneresse & Tikoff, 1999) in two-phase materials typically refer to the end-member behaviors of constant stress and constant strain-rate (Voigt and Reuss bounds, respectively). Given the small volume fraction of magnetite in the samples, magnetite cannot support a greater load than the matrix. Therefore the constant stress assumption is reasonable and strain rate partitioning is the only quantity determining the viscosity contrast between the two phases. Using the assumption of constant stress, we also assume the measured sample viscosity is effectively the viscosity of the matrix plagioclase. Estimated magnetite strain ratios were converted into shear strains to calculate approximate viscosity ratios with the plagioclase. Assuming our various strain estimates are reasonable bounds for the true magnetite strain and the magnetite deformed at an approximately constant rate, we estimate that magnetite has a viscosity between 3.3 and 7.7 times that of plagioclase at 1000°C and between 2.5 and 4.4 at 1200°C for the stresses used in the experiments. Table 5.4 contains the results of viscosity ratio estimates made by each method.

5.8 Conclusions

High-temperature shear deformation of magnetite-silicate aggregates produces strong magnetic anisotropy that rapidly intensifies with progressive strain. Models of AMS

development during strain show that neither a passive marker model nor a rigid rotation model describe the experimental fabric data. Rather, a model involving strain partitioning between magnetite and the plagioclase matrix better predicts the observed AMS. While magnetite grain rotation and alignment probably contributes to the total anisotropy, it is difficult to evaluate the relative importance of this component. Changes in the strength of magnetite shape-preferred orientation obtained with image analysis qualitatively confirms that magnetite is deforming plastically and that changes in magnetite shape anisotropy are responsible for the development of a strong magnetic fabric. Magnetite viscosities are estimated to be higher than that of plagioclase by at least a factor of 2 and as much as 7 at the temperatures and stresses of our experiments. Direct experiments to study the rheological behavior of magnetite and its strain partitioning with silicates will greatly aid the interpretation of magnetic fabrics formed under high-grade conditions in both laboratory and natural environments.

Table 5.1: Deformation conditions.

Specimen	T (°C)	γ	$\dot{\gamma}$ (s^{-1})	σ_{max} (MPa)	σ_{avg} (MPa)	Avg. viscosity (Pa·s)
011-02	1100	1	8.49×10^{-05}	56	47.2	5.56×10^{11}
011-03	1100	2	1.13×10^{-04}	68.5	61.7	5.45×10^{11}
011-04	1100	3	1.56×10^{-04}	44	50.5	3.24×10^{11}
011-05	1000	1	8.49×10^{-05}	127	87.5	1.03×10^{12}
011-06	1200	1	1.13×10^{-04}	19	10.1	8.9×10^{10}
011-08	1200	1.72	1.41×10^{-04}	23	13.4	9.46×10^{10}

Table 5.2: Changes in rock magnetic properties before and after HIPing and deformation.

Sample	M_r/M_s	M_r Am^2/kg	M_s Am^2/kg	B_c mT	T_c $^\circ C$	χ m^3/kg x 10^{-6}	MDF1 mT	MDF2 mT	DP1	DP2
mixed sample powders										
011-00a	0.047	0.111	2.346	5.433	572	20.89				
hot-pressed										
011-01	0.041	0.045	1.089	4.038	499	11.79	33	135	0.62	0.22
deformed										
011-02	0.094	0.148	1.577	9.00	458	12.22	23	170	0.5257	0.19
011-03	0.114	0.168	1.478	8.57	489	12.60	23		0.53	
011-04	0.086	0.076	0.880	5.58	405	9.35	17	151	0.52	0.175
011-05	0.110	0.164	1.487	10.32	478	11.96	30		0.56	
011-06	0.084	0.058	0.692	7.58	470	5.53	15	148	0.56	0.25
011-08	0.057	0.060	1.070	4.86	474	8.80	14	138	0.53	0.287

Table 5.3: Pre- and post-deformation magnetic fabric parameters and orientations.

Specimen	Strain	L	F	P_j	T	D_{max}	I_{max}	D_{min}	I_{min}
				Pre-deformation					
AMS									
"Site mean"	0	1.017	1.018	1.036	0.019	33.1	57.4	302.8	0.2
Specimen average	0	1.025	1.046	1.074	0.318	-	-	-	-
AARM									
"Site mean"	0	1.068	1.304	1.421	0.602	26.9	31.4	289.6	11.8
Specimen average	0	1.066	1.313	1.438	0.470	-	-	-	-
				Post-deformation					
AMS									
011-02	1	1.054	1.254	1.345	0.622	98.2	16.7	272.4	73.2
011-03	2	1.069	1.614	1.813	0.757	87.3	11.4	276.3	78.5
011-04	3	1.515	1.653	2.508	0.095	97.8	0.1	354.6	89.7
011-05	1	1.047	1.197	1.270	0.591	77.8	17.9	287.8	69.5
011-06	1	1.054	1.308	1.411	0.672	86.1	13.8	244.3	75.2
011-08	1.72	1.075	1.515	1.693	0.703	97.3	10.7	267.9	79.2
AARM									
011-02	1	1.133	1.623	1.904	0.591	107.2	17.0	285.0	73.0
011-03	2	1.162	2.305	2.891	0.695	85.1	13.8	277.1	75.9
011-04	3	2.020	2.131	4.307	0.037	100.6	3.6	310.5	85.9
011-05	1	1.187	1.415	1.695	0.340	97.7	17.4	285.6	72.5
011-06	1	1.287	1.489	1.927	0.224	110.9	10.6	298.8	79.3
011-08	1.72	1.142	1.462	1.702	0.481	88.1	18.6	300.6	68.2

Table 5.4: Magnetite/plagioclase viscosity ratios from magnetite strain estimates.

Specimen	T (°C)	γ	AMS model	Rotation-corrected AMS model	Inertia tensor SPO
			Estimated magnetite/plagioclase viscosity ratios		
011-02	1100	1	2.67	4.44	3.13
011-03	1100	2	2.55	3.51	4.76
011-04	1100	3	2.27	2.84	4.41
011-05	1000	1	3.33	7.69	3.57
011-06	1200	1	2.27	3.45	2.67
011-08	1200	1.72	2.50	3.66	4.42

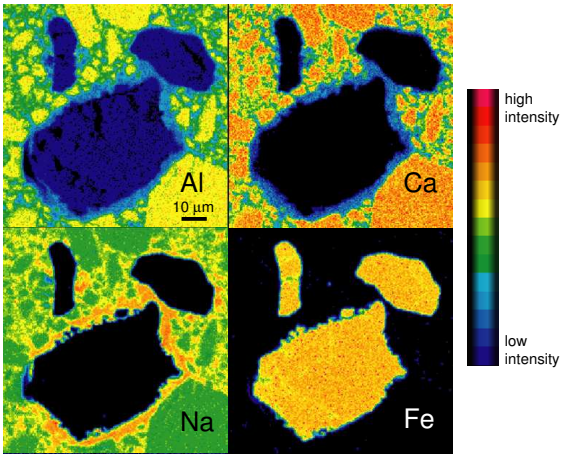

Figure 5.1: Elemental distribution maps from EMPA around oxide grains in hot-pressed sample material.

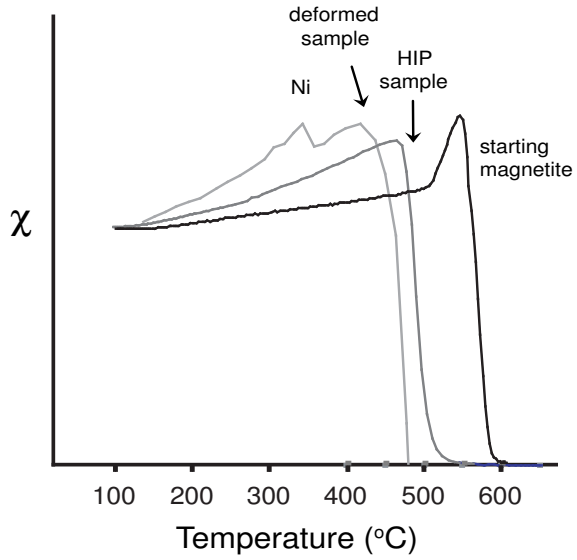

Figure 5.2: Changes in the shape of normalized thermomagnetic susceptibility measurements indicating the typical change in Curie temperature between the mixed sample powder, a HIPed sample, and a deformed sample.

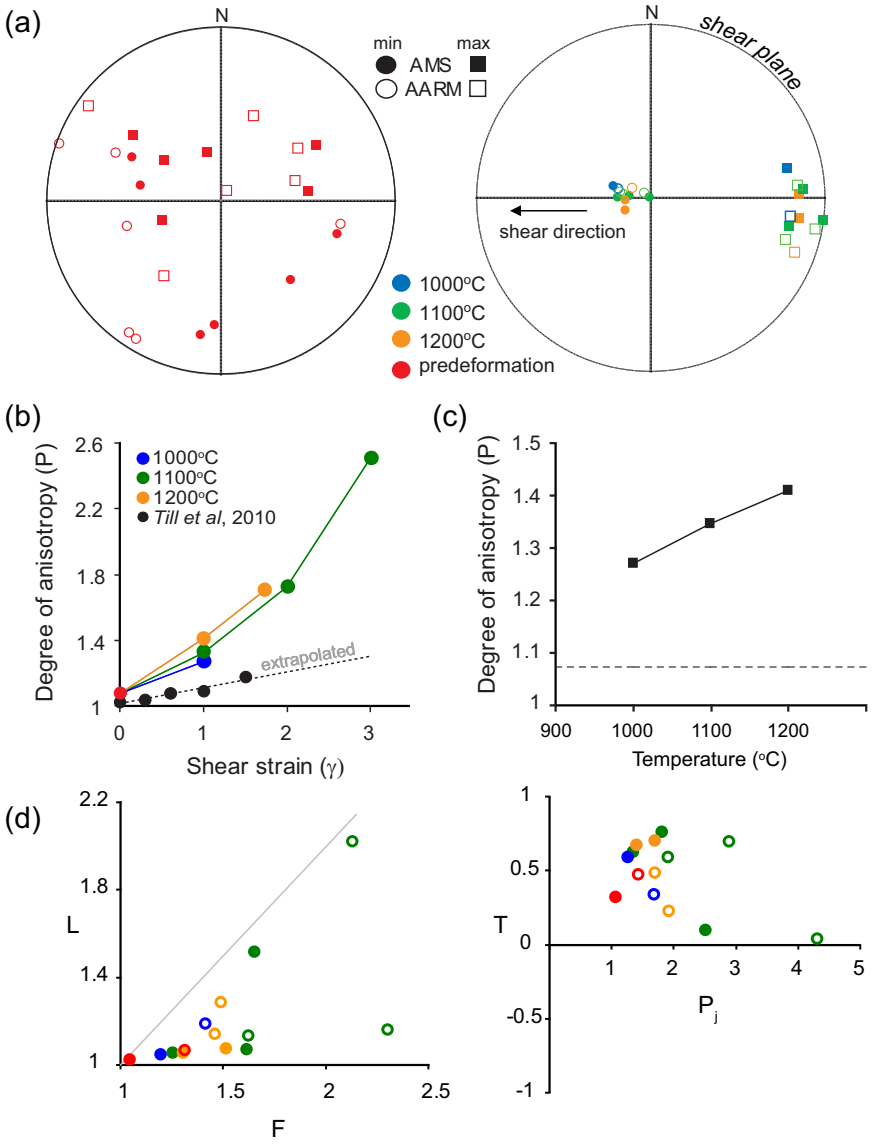

Figure 5.3: Magnetic fabric results for deformed samples. (a) Lower-hemisphere equal-area stereoplots showing orientation of principal magnetic fabric directions for hot-pressed (left) and deformed samples (right). The shear direction is top to the west. (b) Variation in degree of AMS with bulk shear strain. (c) Comparison of AMS P values for samples 011-05, 011-02, and 011-06, each deformed to a shear strain of γ=1, illustrating temperature-dependence of anisotropy. (d) Shape parameters of magnetic fabrics in deformed samples. Solid (open) symbols represent AMS (AARM) data.

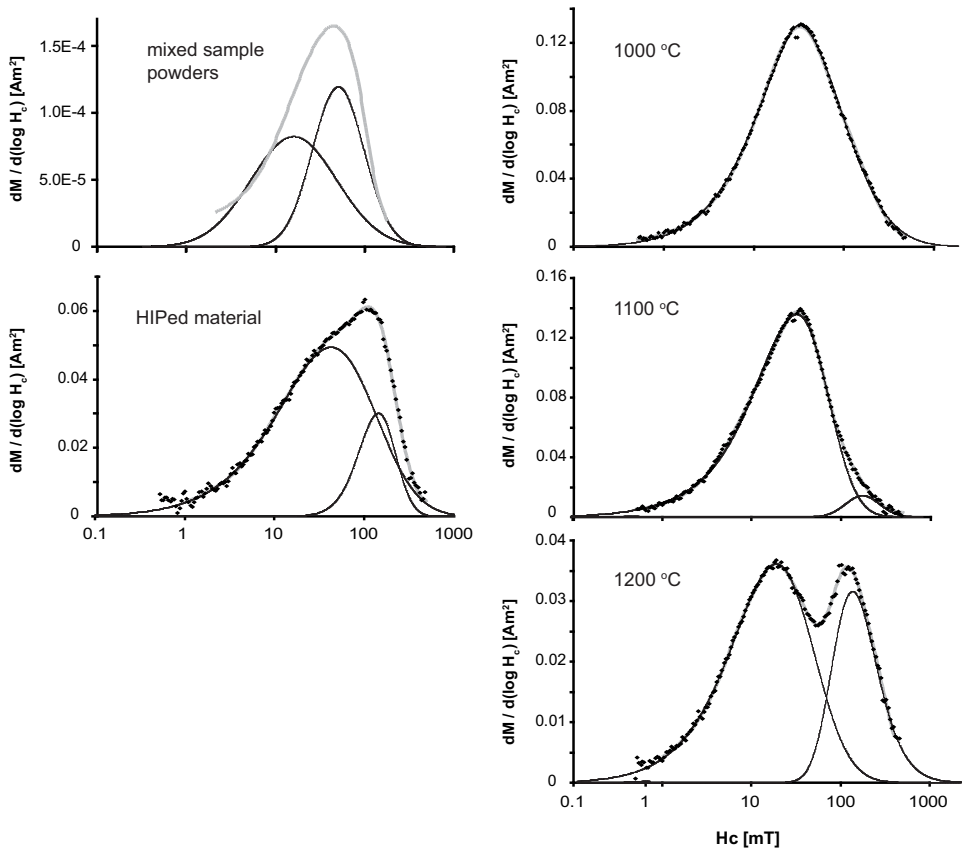

Figure 5.4: Results of IRM unmixing analysis showing the presence of a high-coercivity phase prior to deformation and after deformation at 1200°C. Also evident are small increases in the coercivity of the main, lower-coercivity, component, which are proportional to the differential stress applied during deformation.

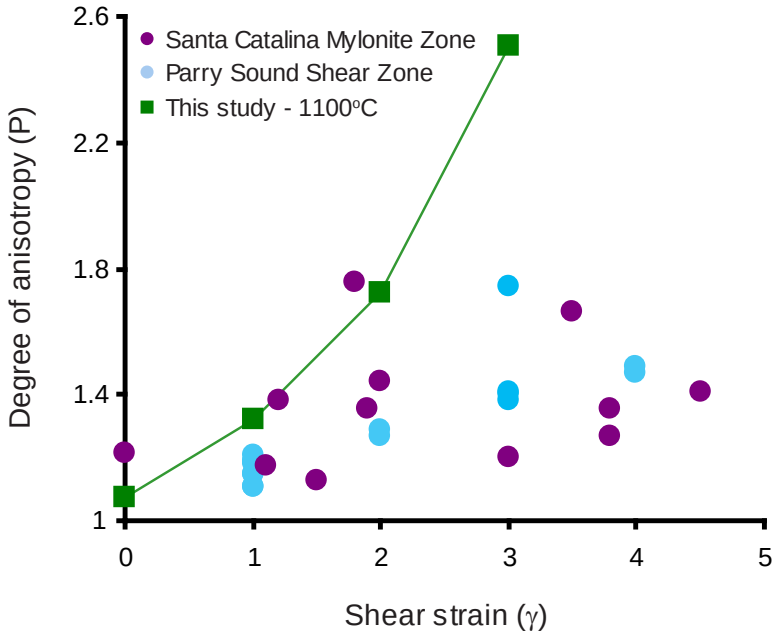

Figure 5.5: AMS measurements from samples deformed at 1100°C compared with AMS data for a natural anorthosite mylonite from Parry Sound, Ontario (Housen et al., 1995), and a granitic mylonite from the Santa Catalina metamorphic core complex, Arizona (Ruf et al., 1988).

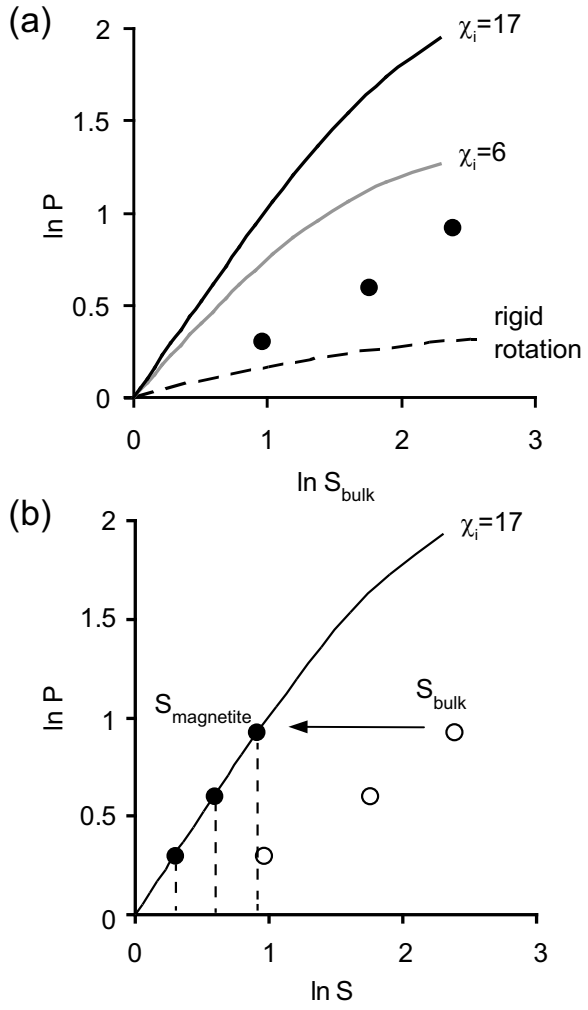

Figure 5.6: a) Degree of AMS for samples deformed at 1100°C (solid black symbols) compared with theoretical models of AMS development according to a rigid rotation and alignment model (dashed line), and a passive marker model for grains with χ_i=6 (solid grey line). The passive model for χ_i=17 is shown for comparison (solid black line). b) The passive model does not describe experimental AMS values when plotted against bulk sample strain, but can be used to estimate the effective mean strain in magnetite grains (solid symbols).

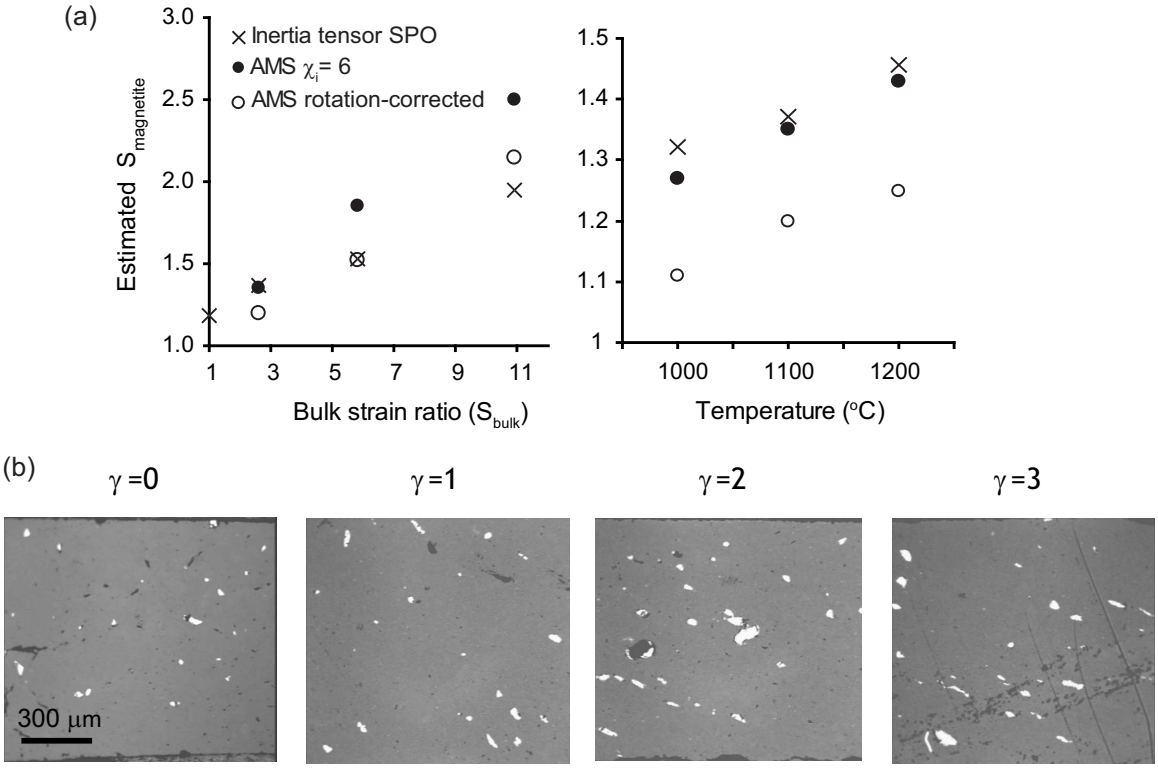

Figure 5.7: a) Strain estimate results from SPO analysis and AMS-strain models as a function of strain (left) and deformation temperature (right). b) Representative reflected light images of samples deformed at 1100°C showing the development of shape-preferred orientation of magnetite as a function of shear strain. Images are taken from surfaces parallel to the shear zone cross-section and the shear sense is top to the left. The bright phase in all images is magnetite and the grey phase is the plagioclase matrix. Dark grey portions of the images are pits or scratches in the sample surface.

Chapter 6

Deformation Microstructures of Magnetite in Synthetic Shear Zones

We present observations of deformation features in magnetite from synthetic magnetite-silicate aggregates deformed between 1000° and 1200°C. Development of shape-preferred orientation and microstructure were observed in plagioclase samples containing 3 wt% magnetite after experimental deformation in coaxial simple shear to shear strains up to γ=3. Electron backscatter diffraction failed to detect a crystallographic preferred orientation in magnetite, however, systematic increases in magnetite grain shape anisotropy with bulk shear strain indicate plastic deformation of magnetite grains. This was confirmed by detailed EBSD maps which revealed progressive changes in orientation across individual magnetite grains that developed after deformation at 1000° and 1100°C. The absence of internal microstructures after deformation at 1200°C suggests that a transition between a dominant diffusive creep mechanism and a dislocation creep mechanism exists below this temperature. Strain partitioning estimates obtained with image analysis were used to determine an approximate viscosity for magnetite at the deformation conditions. Previously published flow laws for magnetite are in poor agreement with the observed magnetite strains, and the theoretical flow laws have thus been re-evaluated. By replacing the rate equations for oxygen diffusion in magnetite with more appropriate

oxygen diffusivity data in the flow laws, the predicted rheological behavior of magnetite agrees better with both our observations and with previous experimental results for deformation of magnetite and similar spinel-structured ferrite phases. New deformation mechanism maps for magnetite have been constructed using the updated and recalculated flow laws, although direct deformation experiments on magnetite are needed to verify the flow laws.

6.1 Introduction

The deformation behavior of oxide minerals in most rocks is often overlooked due to their presence in typically small quantities as accessory phases, and consequently their very minor influence on the bulk strain behavior of most rocks. Accordingly, documentation of magnetite deformation in the literature from field and laboratory studies is sparse. However, magnetite is an important component of many iron formations and iron ore bodies (Morales et al., 2008; Barbosa & Lagoeiro, 2010), and zones rich in Fe-Ti-oxides in oceanic core complexes are systematically associated with significant strain localization (Agar & Lloyd, 1997; Natland, 2002). Interpreting the deformation histories of these and many other rock types requires study of the plastic flow behavior and microstructural features associated with deformation in magnetite but very little data are currently available to aid in such studies (Siemes et al., 1991).

A small number of deformation experiments have previously been performed on magnetite aggregates and single crystals (Muller & Siemes, 1972; Hennig-Michaeli & Siemes, 1975, 1982; Crouch & Robertson, 1990; Gómez-García et al., 2002); however, most of these experiments were conducted over relatively narrow ranges of temperature or stress and are insufficient to describe the general deformation behavior of magnetite over the full range of conditions typical of ductile deformation in the Earth's crust. Siemes et al. (1991) described the need for high-quality experimental data on common ore minerals, including magnetite, in order to create valid deformation mechanism maps. Little additional data have surfaced since this recommendation. Additionally, structural geology studies that use magnetic anisotropy data would greatly benefit from better constraints on magnetite deformation behavior by improving interpretations of magnetic fabrics measured in magnetite-bearing rocks. Naturally deformed magnetite has been

noted in a handful of studies (e.g. Housen et al., 1995; Mamtani et al., 2007; Agar & Lloyd, 1997), but the conditions of paleostresses and strain rates are often difficult to determine in field studies.

We present a study of microstructural features in plastically-deformed magnetite from laboratory shear experiments and have attempted to determine approximate strain partitioning between magnetite and plagioclase at the conditions of our experiments. A short review of experimental work on magnetite deformation is given. Additionally, previously published flow laws for magnetite are re-examined and it is determined that the oxygen diffusion coefficients used previously are not appropriate at high temperatures (T > 0.5 * melting temperature). After modification, the flow laws accord well with the results of the current and previous experiments and are used to construct new deformation mechanism maps for magnetite.

6.2 Experimental Procedures

6.2.1 Sample Synthesis

Samples for deformation were created by mixing synthetic magnetite powder (Wright Industries 041183) and powdered Beaver Bay anorthosite with a plagioclase composition of approximately An_{70} (Table 6.1). The magnetite has a mean grain size of 18.3 $\pm$12 μm (Yu et al., 2002) and was dispersed at 3 wt% in the plagioclase matrix material. The plagioclase was sieved to remove the coarse-grained fraction above 64 μm. After thorough mixing, sample powders were isostatically cold-pressed under a hydrostatic pressure of 130 MPa in an oil-medium pressure vessel to avoid imparting any strong initial fabric to the samples prior to deformation. This cold-pressing step resulted in a solid pellet that was shaped and fitted into an oxidized Ni canister which served as an f_{O_2} buffer. Sample-filled Ni canisters were isostatically hot-pressed in an Ar gas-medium Paterson pressure vessel at 1200 °C with a confining pressure of 300 MPa for 3 hours.

Moderate chemical changes occurred in the magnetite during initial hot-pressing due to cation exchange between the matrix plagioclase and magnetite grains. Electron microprobe analysis (EMPA) of the synthesized samples showed that the opaque grains in the hot-pressed material are Fe-oxides containing almost 5 wt% Al based on

analyses of several grains. Microprobe analysis also revealed that the oxide grains are surrounded by rims composed of Al-Ca-Na-silicate which are depleted in Al and Ca but enriched in Si and Na relative to the silicate matrix. These rims are not visible in reflected light microscopy, and may be plagioclase of a more albite-rich composition (see Figure 5.1, Chapter 5). The average oxide composition before deformation compared with matrix and rim composition is shown in Table 6.1. Al^{3+} substitutes for Fe^{3+} in the magnetite-hercynite solid solution according to the formula $Al_xFe_{3-x}O_4$ where x=0 for pure magnetite with the inverse spinel structure and x=2 corresponds to hercynite with the normal spinel structure. The oxide phase in our hot-pressed samples has a composition around x=0.4 and will be referred to as magnetite for simplicity. EMPA was repeated on oxide grains for selected post-deformation samples, and showed that further compositional changes after deformation were relatively minor, although Al contents were slightly higher in magnetite grains from samples deformed at 1200°C. Microprobe analysis did not detect any compositional zoning or gradients in Fe or Al content from compositional profiles across several magnetite grains, either before or after deformation.

6.2.2 Deformation Procedures

After hot-pressing, all metallic material from the Ni canister was removed from the sample by cutting and grinding, and the sample material was cut into discs of 1 mm thickness. Sample discs were shaped to fit the elliptical cross-section of the pistons, which were made from 5 mm-diameter alumina rod cut at a 45° angle. The alumina pistons and sample disc were enclosed in an oxidized Ni jacket. A NiO layer on the interior surface of the jacket was visible after all experiments, indicating that the oxygen fugacity was maintained near the Ni-NiO buffer during deformation. The full sample assembly includes larger alumina and zirconia pistons on either side of the small angled pistons, all of which was enclosed in a thin Fe jacket. See Figure 4.3 for a simple diagram of the sample assembly geometry.

Experiments were performed in a coaxial Paterson deformation apparatus (Paterson, 1990) using Ar as a pressure medium. Deformation was performed at temperatures of 1000°, 1100° and 1200°C and samples were deformed to shear strains in the range

γ=1-3. Deformation was performed with a confining pressure of 300 MPa and at a constant piston displacement rate, approximating constant strain rates near 1x10^{-4} s^{-1}. Temperatures were maintained within $\pm 5^{\circ}$ of the target temperature during the experiments. Differential stresses were varied as necessary to maintain the strain rate, which produced nearly steady-state flow in experiments at 1100° and 1200°C, although deformation at 1000°C was marked by continuous strain hardening (Figure 6.1). Maximum differential stresses, finite strains and exact strain rates for each experiment are listed in Table 6.2. The sample strength in the present experiments is slightly weaker than the experimental deformation data for plagioclase aggregates reported by Rybacki & Dresen (2000), even for deformation in the presence of water. The lower strength of our samples may be caused by impurities in addition to the presence of water in the sample starting material, since no attempt was made to ensure that samples were thoroughly dry prior to deformation.

6.3 Shape Preferred Orientation

Reflected light image analysis was used to determine the mean change in magnetite grain shape and the shape-preferred orientation. Reflected light photomicrographs were obtained from polished cross-sectional shear zone surfaces on each sample (i.e. a surface containing both the shear direction and the shear plane normal) to observe the magnetite in the direction of highest grain elongation. Polishing was performed with progressively finer diamond lapping films down to a grit size of 0.1 μm. Because of the small sample size and low concentration of magnetite grains, serial sectioning was performed on the cross-sectional surfaces by repeatedly grinding, polishing, and acquiring images to provide an adequate number of magnetite grains for image analysis (>200 grains/sample). The destructive nature of the serial sectioning technique and the small sample size precludes making SPO measurements in three dimensions, and this is an inherent limitation in the accuracy of the strain estimates made with this method. The program *SPO* (Launeau & Robin, 1996) was used to calculate a mean grain shape (aspect ratio) with the inertia tensor method, which is a suitable analysis method for discrete, isolated objects in an image. The strain ratio S of the strain ellipsoid can be calculated from the bulk shear strain γ of the experiment. Similarly, the mean grain

shape of magnetite in two dimensions indicated by the SPO can be taken as a rough estimate of the magnetite strain ratio in each sample which can be converted back to shear strains. S is related to shear strain by the equation:

$$S = \sqrt{\frac{0.5(\gamma^2 + 2 + \gamma\sqrt{\gamma^2 + 4})}{0.5(\gamma^2 + 2 - \gamma\sqrt{\gamma^2 + 4})}} \tag{6.1}$$

(Ramsay & Huber, 1983, Eq. 2.7).

6.3.1 SPO Results

Magnetite SPO increases monotonically as a function of bulk shear strain (Figure 6.2a). The HIPed material has a weak, but measurable SPO indicating that the initial distribution of magnetite orientations is not perfectly isotropic. A comparison of three samples deformed to shear strains of γ=1 at different temperatures reveals a significant temperature-dependence of magnetite grain shape anisotropy (Figure 6.2b). The magnetite SPO of a sample deformed at 1200°C has an grain shape ratio approximately 15% higher than that of a sample deformed to the same shear strain at 1000°C. The orientation of the mean grain shape representing the SPO is always at a low angle to the shear plane, but this angle did not vary systematically with shear strain or temperature. In all samples, the mean magnetite grain shape has a lower ellipticity than that of the strain ellipse for the bulk sample, indicating that magnetite deforms at a lower average rate than the plagioclase at each studied temperature. The initial average grain shape of the starting magnetite particles is slightly elongate, with a mean shape ratio around 1.5 (Yu et al., 2002). An assemblage of non-equidimensional particles with a wide distribution of initial orientations deforming at a lower viscosity than the matrix will undergo some degree of rotation during deformation in addition to plastic strain (Gay, 1968). Therefore part of the measured SPO may consist of a contribution from the rotation and alignment of these particles. The mean magnetite grain shape increases over that of the starting grain shape at high strains (Figure 6.2a), so the measured SPO cannot result solely from the degree of particle alignment. It is difficult to separate the rotational contribution to SPO from the change in shape resulting from plastic strain, so the strain estimates should be considered to be upper bounds on the true magnetite strain.

6.3.2 Strain Partitioning

The observed temperature dependence implies that strain is partitioned between the two phases in all experiments, and that the strain partitioning varies with deformation temperature and applied stress. The small differences in experimental strain rates and the inverse correlation between SPO strength and the magnitude of differential stress suggest that temperature has a stronger influence than stress or strain rate in determining strain partitioning. Rheological descriptions of strain partitioning in two-phase materials typically refer to the end-member behaviors of constant stress and constant strain-rate (Voigt and Reuss bounds, respectively) (Handy, 1990; Tullis et al., 1991; Vigneresse & Tikoff, 1999). Given the small volume fraction of magnetite in the samples, the magnetite cannot support a greater load than the matrix, therefore the constant stress assumption is reasonable, and strain rate partitioning is the only quantity determining the viscosity contrast between the two phases. Using the constant stress approximation we also assume that the measured sample viscosity is effectively the viscosity of the plagioclase matrix, which was determined using the average differential stress from each experiment (Table 6.2). Assuming that the mean grain shape determined for each sample by the SPO analysis approximates the strain ratio S, these estimated magnetite strains can be compared with the bulk sample strains to determine approximate strain partitioning between the two phases. Converting magnetite strain ratios back to shear strains using Equation 6.1 results in estimated magnetite viscosities in the range 2.67-4.67 times that of the plagioclase matrix (Figure 6.2), with the highest inferred viscosity contrast at 1000°C and lowest viscosity contrast at 1200°C. We note that although the condition of steady-state deformation in magnetite cannot be verified, this should not significantly affect the estimated viscosity ratios unless extreme strain hardening occurred. To determine how strain partitioning between magnetite and plagioclase occurs at geologic temperature and strain rates, experimental data covering a broader range of temperatures, strain rates, and sample compositions are required.

6.4 Magnetite Microstructure

Electron backscatter diffraction (EBSD) was performed on all samples after deformation to quantitatively examine magnetite microstructure and crystallographic preferred

orientation (CPO). Polished surfaces were produced on each sample after deformation both parallel to the shear plane, and along a cross-sectional surface parallel to the shear direction and perpendicular to the shear plane. Sample preparation for EBSD included a final polish with a colloidal silica suspension in addition to polishing with diamond lapping films. EBSD was performed on a JEOL 6500 FEG scanning electron microscope using a 20 kV accelerating voltage, a working distance of 25 mm, and a 17 nA beam current in the Characterization Facility at the University of Minnesota. Diffraction patterns were automatically collected and indexed and later analyzed with Channel 5+ software by HKL Technology. Detailed EBSD maps were also collected in grids of points using step sizes less than a micron. EBSD maps were made for several magnetite grains in each deformed sample and one sample of undeformed material to show the changes in internal microstructure that resulted from deformation at different temperatures. Noise reduction in the EBSD maps was achieved by performing a "wildspike" removal, which corrects the orientation of single points that differ significantly from all neighboring measurement points, and extrapolating zero-solution points based on the orientation of five neighboring measurement points.

6.4.1 Crystallographic Preferred Orientation

For measurements of CPO, point analyses were made on several hundred individual grains per sample using one point per grain on a surface parallel to the shear plane. Crystallographic pole figures for <100>, <110>, and <111> axes in magnetite from EBSD measurements are shown in Figure 6.3a. Crystallographic textures are alternatively visualized in inverse pole figures showing the projection of certain sample directions onto the crystal coordinate system. Inverse pole figures for the shear plane normal and the shear direction are shown in Figure 6.3b. CPO strength is extremely weak in all deformed samples. No clear preferred direction of the crystallographic axes can be identified in the pole figures, although inverse pole figures for samples deformed at 1000 and 1100°C show a weak maximum of shear directions close to crystallographic <111> directions, and a weak association of the shear plane normals with <100> directions. CPO strength was quantified using calculated M-index values of Skemer et al. (2005), where an M-index of 1 represents a monocrystalline texture, and an M-index of 0 represents a perfectly random orientation distribution. M-index values in deformed

samples are low, ranging from 0.012 to 0.066, indicating that the magnetite textures are not significantly stronger than a random distribution of orientations and do not vary systematically as a function of deformation temperature or shear strain. EBSD data analysis by the Channel 5+ software also identified the histograms of misorientation distributions for most deformed samples as having a high probability of being random when compared to a theoretical random distribution for material with cubic crystal symmetry, also indicating that the CPOs in deformed samples are not statistically significant.

6.4.2 Intragrain Misorientation

Detailed EBSD maps were also made on individual magnetite grains to examine internal deformation microstructure. Magnetite grains in undeformed sample material contain only very small subgrains at the edges of grains and have cumulative changes in orientation of no more than 2° across each grain (Figure 6.4a). In strong contrast, many grains in samples deformed at 1000°C and 1100°C contain abundant low-angle boundaries (misorientation>1.5°)and are characterized by large changes in orientation across the grains. While discrete sub-grains are seen in some magnetite particles, most grains contain less distinct subgrain boundaries and are instead characterized by progressive changes in crystallographic orientation across the grain surface (Figure 6.4b,c). The extent of intragranular "bending" is as much as a 25° change in orientation within a single grain (Figure 6.5a,b). Similar subgrain boundaries or gradients in intragrain orientation are absent in samples deformed at 1200°C (Figure 6.4d). This suggests that a transition from a dislocation-dominant to a diffusion-dominant mechanism lies in the 1100-1200°C range for magnetite at the mean grain size studied here. In addition, high-angle grain boundaries (misorientation>10°) were occasionally seen in EBSD maps (Figure 6.4c), showing that a small number of magnetite particles are actually polycrystalline. These particles are interpreted as small aggregates of magnetite grains that originally clustered together during sample powder mixing, which is an unavoidable effect of the magnetic nature of the material. Alternatively, the starting magnetite material may have contained some polycrystalline particles initially.

For most of the magnetite in samples deformed at 1000°C and 1100°C, the crystal orientations within each grain typically disperse along small circle girdles about a central rotation axis. The rotation axis is most clearly identified when pole figures for

<100>, <110> and <111> in individual grains are superimposed on one another (e.g. Figure 6.5c). The central rotation axis in most magnetite grains coincides with <110> directions. More rarely, the rotation axis for individual grains corresponds to a <100> direction. Additionally, the orientations of the rotation axes are consistently subparallel to the shear plane and subperpendicular to the shear direction, and where subgrain boundaries can be discerned, the rotation axes are roughly parallel to the trace of the boundary walls. This configuration is expected for low-angle tilt boundaries composed of geometrically-necessary edge dislocations (Lloyd et al., 1997; Prior et al., 2002; Reddy et al., 2007). For twist boundaries composed of screw dislocations, the subgrain boundary walls would form parallel to the slip plane, and the rotation axis and pole to slip plane should both be normal to the subgrain walls.

Methods outlined by Lloyd et al. (1997) and Reddy et al. (2007) demonstrate how misorientation analysis may be used to determine the active slip system in a deformed crystal. The schematic diagram in Figure 6.6 illustrates the geometric relationships utilized by this method. The slip directions for magnetite were constrained to <110> directions on the basis on deformation studies in magnetite and other spinel-structured crystals (see below). For rotation axes aligned with <110> directions in magnetite grains, which is indicated by the misorientation microstructure of most magnetite grains deformed at 1000°C and 1100°C, the slip system determined by misorientation analysis is {100}<110>. The small number of grains that show orientation dispersions around <100> directions indicate slip in the $\{110\}\langle 1\bar{1}0\rangle$ system (Figure 6.6c).

6.4.3 Slip Systems in Magnetite and Spinels

Deformation experiments on magnetite single crystals and aggregates (Muller & Siemes, 1972; Hennig-Michaeli & Siemes, 1975, 1982) have determined that the dominant slip system for magnetite between room temperature and 400°C is $\{111\}\langle 1\bar{1}0\rangle$. Slip in this system typically produces a 110 fiber texture (Wenk et al., 1989) which was observed by Muller & Siemes (1972). Charpentier et al. (1968) observed slip along {111} and {100} planes after indentation tests on magnetite at room temperature. As in other spinels, slip in magnetite always occurs along <110> directions (Hornstra, 1960). Based on theoretical considerations, Hornstra (1960) also predicted {111} to be the most favorable slip plane for spinel-structured crystals, and this has been frequently found in studies

on spinels (Veyssiere et al., 1978; Mitchell et al., 1976). However, Lewis (1966) and Mitchell et al. (1976) demonstrated that slip on {110} becomes dominant with increasing nonstoichiometry in spinels. This was explained by a substantial decrease in lattice resistance to slip, or Peierls stress, on {110} planes due to increased concentrations of charge-compensating cation vacancies. An analogous process could favor {110} slip in magnetite at oxygen fugacities higher than those necessary for magnetite stoichiometry, resulting in cation deficiency. Additionally, experiments by Duclos et al. (1978) found that the $\{110\}<1\bar{1}0>$ slip system was active during high-temperature deformation of stoichiometric Al-Mg spinel single crystals for compression parallel to [100], but that compression parallel to [110] produced slip on {111}. Duclos et al. (1978) determined that the Peierls stress for slip on {111} was likely to be only 20% lower than that for slip on {110}.

In Li-ferrite spinel, Mishra & Thomas (1976) determined that dislocation motion occurred only on {110} planes by examination of stacking fault structures after deformation at 1200°C, despite this system being energetically less favorable than {111}<110>. In room-temperature indentation experiments on MnZn-ferrite, Broese Van Groenou & Kadijk (1989) observed dominant {100} and {111} slip planes, and secondary slip on {110}. A summary of the wide variation of dislocation configurations observed in spinel-structured phases, including the common tendency for dissociation into partial dislocations and the formation of stacking faults, is given by Zitzelsberger & Schmidbauer (1999). For magnetite, the temperature-dependence of dominant slip systems above 400°C appears to be a relatively unexplored topic.

The combined literature on deformation in spinels demonstrates that slip on planes other than {111} is commonly observed, and the question of which one is preferred during creep of magnetite may be determined by a combination of factors including temperature, composition, stoichiometry, and orientation of principal stresses relative to crystallographic orientation in a grain.

6.4.4 Absence of Magnetite CPO

The presence of subgrains and large cumulative misorientations in magnetite grains indicates that dislocation processes are active in magnetite at 1000° and 1100°C, yet there is no indication of CPO in any sample. Wenk et al. (1989, 2005) noted that in modeled

texture development for both simple cubic halite and spinel-structured ringwoodite, slip in the system {110}<1$\bar{1}$0> results in weak texture development at low strains due to canceling rotations. This slip system was observed as a secondary glide mode by Hennig-Michaeli & Siemes (1982) in magnetite single crystals deformed at 400°C. If this slip system is active during our experiments, it could be partially responsible for the lack of well-developed CPO. Additionally, Yamazaki & Karato (2002) observed slow development of CPO during high-strain deformation of (Mg,Fe)O in dislocation creep with slip along {100} and {111} planes, suggesting that texture development in some cubic minerals may be inherently slow compared to lower-symmetry phases. Among the few rare examples of CPO measurements in naturally-deformed magnetite, Terry & Heidelbach (2006) noted weak textures in magnetite from high-grade shear zones, and Agar & Lloyd (1997) mapped magnetite crystallographic orientations in oxide-rich oceanic shear zones but failed to detect any preferred orientation. The weak crystallographic textures measured in our experimentally deformed samples may simply be a function of the small sample size and the limited number of magnetite grains available for analysis on the sample surface. The number of data points may be insufficient to adequately define a CPO in a high-symmetry material. If this is the case, magnetite CPOs will also be difficult to detect in naturally deformed rocks, since magnetite concentrations in most rocks are typically less than 1% by volume. Alternatively, a magnetite CPO may not become well-defined until higher strains are reached, and processes of subgrain formation and rotation are more developed.

The indication of slip on {100} planes from grain misorientation configurations is unexpected for magnetite. Mehl & Hirth (2008) found that misorientation analysis of plagioclase subgrains in a mylonite indicated a distinctly different slip system than the slip system that characterized the strong sample CPO. Mehl & Hirth (2008) postulated that the misorientation structures in plagioclase may have formed by a different process than the process that controlled the formation of the strong CPO, but did not speculate on the specific mechanism responsible for development of the misorientation microstructures. In our samples the weak CPO does not indicate any slip system, but it is conceivable that slip in a different system controls the process of CPO development while slip activity in {100}<110> is responsible for the formation of incipient subgrains. It is possible that the previously described tendency for climb dissociation

of dislocations in magnetite (Zitzelsberger & Schmidbauer, 1999) is responsible for the appearance of slip on {100} through a complicated pattern of dislocation climb, but the process by which this might happen is not entirely clear. If {110}<1$\bar{1}$0> was active in our samples during deformation, the resulting CPO may be expected to be weak based on the symmetry considerations and modeled fabrics described by Wenk et al. (1989, 2005). These observations suggest caution in making assumptions about dominant deformation mechanisms on the basis of CPO alone. Experimental textural studies over a range of temperatures are needed to determine the conditions that will produce a strong CPO in magnetite.

6.5 Magnetite Deformation Mechanism Maps

6.5.1 Previously Published Maps

Atkinson (1977) formulated theoretical flow laws for magnetite and published an accompanying preliminary deformation mechanism map for 662° in the form of a grain size *vs* stress plot. For the temperatures and differential stresses of our experiments, the flow laws described by Atkinson (1977) predict magnetite strain rates near 10^{-7} s^{-1} at 1000°C and 150 MPa and strain rates near 10^{-10} s^{-1} at 1200°C and 10 MPa. The finite strain accumulated by magnetite deforming at rates over 3 orders of magnitude slower than plagioclase would be imperceptible in our deformed samples and these flow laws seem to strongly underestimate high-temperature magnetite creep rates.

Crouch & Robertson (1990) also presented a deformation mechanism map for magnetite and determined rate laws for various creep regimes based on creep experiments in a bending apparatus. The magnetite strain rates predicted by the creep equations in Crouch & Robertson (1990) for the conditions of our experiments are approximately 10^{-2} s^{-1}, or two orders of magnitude faster than the bulk rate at which the plagioclase deformed. The magnetite in our samples cannot deform more quickly than the matrix, and the strain partitioning indicated by the SPO analysis suggests that it is more viscous than the plagioclase, indicating that the Crouch & Robertson (1990) flow laws overestimate magnetite strain rates at high temperature.

Because oxygen diffusion is the rate-limiting process for magnetite creep, the reason for the discrepancy between the maps of Atkinson (1977) and Crouch & Robertson

(1990) quickly becomes apparent when the respective data for oxygen diffusion in magnetite used in each study are compared. Atkinson (1977) used the data of Castle & Surman (1967, 1969), who measured a relatively low activation energy of 71 kJ/mol for oxygen diffusion between 300 and 550°C. Crouch & Robertson (1990) inferred oxygen diffusivities in magnetite from their measured creep rates at temperatures between 500 and 1100°C and used these calculated diffusion rates in the construction of their map. The activation energy of 264 kJ/mol obtained by Crouch & Robertson (1990) is much higher than that of Castle & Surman (1967), and their obtained diffusivities are faster overall as well. An evaluation by Chokshi (1988) of similar creep studies determined that it is generally not possible to derive accurate diffusion coefficients from creep data. Additionally, Crouch & Robertson (1990) normalized all creep and diffusion data to an oxygen fugacity defined by a constant concentration of CO in CO_2, which differs from a constant oxygen fugacity relative to the buffers that define that magnetite stability field. This makes the true dependence of creep and oxygen diffusion in magnetite on both oxygen fugacity and temperature difficult to determine for their experiments.

A summary of previously published oxygen diffusion measurements in magnetite and other spinel-structured oxides are shown in Figure 6.7, including the data of Crouch & Robertson (1990). Oxygen diffusion in magnetite was also measured by Giletti & Hess (1988) from 500 to 800°C, who determined an activation energy of 188 kJ/mol, and rates similar to Castle & Surman (1969) where the temperature range of their measurements overlap. They suggested that a change in diffusion mechanism below 500°C may be responsible for the lower activation energy of Castle & Surman (1969). We consider the oxygen diffusion rate law found by Giletti & Hess (1988) the most appropriate to use in theoretical flow laws for magnetite by merit of having measured the diffusivity directly and over a temperature range relevant to deformation under geological conditions.

6.5.2 Construction of New Maps

We have constructed deformation mechanism maps for magnetite in the form of a stress *vs* temperature map, largely based on the flow laws described by Atkinson (1977) as summarized in Housen et al. (1995), but with changes to the oxygen diffusivities as described above. Strain rates in the dislocation creep regime were calculated according

to:

$$\dot{\epsilon} = \frac{AbD_vG}{kT}\left(\frac{\sigma}{G}\right)^3 \tag{6.2}$$

The Dorn constant, A, is given as 0.5736 by Atkinson (1977). The Burgers vector, b, for slip in <110> directions is 5.935x10^{-10} (Fleet, 1981) and the shear modulus, G, was estimated as 98 GPa based on data from Birch (1966). D_v is the lattice (volume) diffusivity of oxygen in magnetite (Giletti & Hess, 1988) given by $D_0 exp(-Q/RT)$ where the pre-exponential term D_0 is 3.5 x 10^{-10} cm^2/s and the activation energy is 188.4 kJ/mol. The stress exponent, n, was taken to be 3 since this value was found for magnetite by Crouch & Robertson (1990) and Gómez-García et al. (2002) and values near this have been found for other spinels (Nishikawa, 1980; Lawlis et al., 2001).

Creep rates in the diffusion creep regime were calculated according to the equation (Frost & Ashby, 1982):

$$\dot{\epsilon} = \frac{21\sigma\Omega D_v}{kTd^2}\left(1 + \frac{\pi\delta}{d}\frac{D_b}{D_v}\right) \tag{6.3}$$

where Ω is the molecular volume, given as 7.395x10^{-29} by Robie et al. (1966), d is the grain size, and δ is the grain-boundary width, which was chosen to be $3b$. The term in parentheses is an effective diffusion rate incorporating both lattice diffusion-dominated (Nabarro-Herring) creep which predominates at high temperatures, and lower-temperature flow dominated by grain-boundary diffusion (Coble) creep. The grain boundary diffusivity of oxygen was assumed to have the same pre-exponential value and an activation energy equal to 2/3 of that of the lattice diffusivity value (Frost & Ashby, 1982). After Crouch & Robertson (1990), a dislocation glide regime was included using a glide-flow boundary of $0.005G$, and a 0 K flow stress of $0.05G$, as suggested for oxides by Frost & Ashby (1982). Although Crouch & Robertson (1990) included a low-temperature dislocation creep regime limited by diffusion along dislocation cores in their map for magnetite, this regime has not been observed to occur in magnetite or many other ceramic oxides (Okamoto, 1989) and so has been omitted here.

The recalculated deformation mechanism map for magnetite is shown in Figure 6.8 with the limited high-temperature mechanical data on deformed magnetite, and data for some other spinel-structured ferrites (Nishikawa, 1979; Rabier et al., 1976), although the experimental measurements have not been used to constrain the map in any way. The map is plotted in terms of stress and temperature for a constant grain size of 20

μm. The stress and temperature conditions for our experiments are also indicated on the diagram. Figure 6.9 also contains Arrhenius diagrams comparing the temperature dependence of creep in the newly formulated flow laws with those suggested by Crouch & Robertson (1990) and Atkinson (1977) for different deformation regimes. Note that the rate laws in the diffusion creep regime for both the current study and the data from Atkinson (1977) show some curvature due to the use of the effective diffusion coefficient which contains contributions from both lattice and grain-boundary diffusion.

Predicted magnetite strain rates according to the map are of the same order of magnitude at 1000° and 1100°C as those estimated from strain partitioning coefficients obtained with SPO analysis. Magnetite strain rates predicted by the map at 1200°C are too low, and the inferred pattern of higher effective magnetite strain rates at higher temperatures during the experiments is not supported by the deformation map. However, the true magnetite strain rates during the experiments are unknown and without having direct mechanical and rheological data for the magnetite, the map appears to provide a good first-order prediction of the conditions under which magnetite will deform. The experiment conditions at 1200°C lie close to the boundary between dislocation and diffusional creep regimes, consistent with the interpretation that the magnetite in samples deformed at 1200°C deformed mainly by diffusion creep. The available experimental data on magnetite and other ferrites are generally in good agreement with the map.

6.5.3 Effect of Oxygen Fugacity

Although the dependence on oxygen fugacity, f_{O_2}, of Fe diffusion in magnetite is well known (Dieckmann & Schmalzried, 1977), several studies have also observed a dependence of O diffusion on f_{O_2}. Consequently, some studies have reported a similar relationship between f_{O_2} and magnetite creep rates. Because Giletti & Hess (1988) found no trend in oxygen diffusion with changing f_{O_2} within the error of their experiments, and because the f_{O_2}-dependencies determined experimentally vary from one study to another, we have not incorporated this factor into the deformation maps or flow laws for magnetite. However, a clear dependence on f_{O_2} was seen for oxygen diffusion by Castle & Surman (1969), who determined that O diffusion varied as $f_{O_2}^{-0.27}$. Millot & Niu (1997) and Millot et al. (1997) observed a change in the sign of f_{O_2}-dependence with $fO_2^{-0.5}$ at relatively reducing conditions and $fO_2^{0.17}$ at more oxidizing conditions.

This transition was explained by a change in diffusion mechanism from a simple vacancy mechanism involving isolated O defects to a mechanism involving coupled Fe and O vacancy pairs.

Crouch & Robertson (1990) reported that creep rates varied as $f_{O_2}^{0.59}$ in the low-T, high stress regime and found a broad creep dependence of $f_{O_2}^{-0.56}$ in the high-T, low stress regime, and also showed that the exact f_{O_2}-dependence varied with differential stresses. Creep experiments on magnetite single crystals by Gómez-García et al. (2002) showed distinct minima in strain rates over a range of f_{O_2}, with exponents ranging from -0.4 at low f_{O_2} to 0.5 at high f_{O_2}, however their data are only reported in terms of relative strain rates. The above studies all show that both diffusion and creep rates can vary by two orders of magnitude within the magnetite f_{O_2} stability field. In effect, this places error bars of at least one log unit around the strain rate contours in Figure 6.8. It seems clear that f_{O_2} has a significant effect on the deformation behavior of magnetite, but the change in the sign of the dependence due to transitions in the point defect structure will make this effect difficult to predict in nature unless f_{O_2} is well constrained.

6.6 Conclusions

Magnetite grains deformed in a silicate matrix during experimental shear deformation are characterized by a shape-preferred orientation that becomes increasingly strong with both shear strain and deformation temperature. Changes in the mean magnetite grain shape and SPO strength are primarily attributed to plastic deformation of magnetite, although some component of particle rotation and alignment is predicted as a result of strain partitioning between magnetite and the silicate matrix. Crystallographic-preferred orientations in deformed magnetite are extremely weak, however magnetite grains containing incipient subgrains and large gradients in crystallographic orientation are interpreted as evidence for active dislocation creep processes during deformation at 1000°C and 1100°C. The rate equations for magnetite deformation have been re-evaluated and adjusted to include more appropriate data on oxygen diffusion in magnetite and the updated flow laws are in reasonably good agreement with the observed magnetite strains during high-T experimental deformation. Future direct experiments on the deformation behavior of magnetite should help to refine the theoretical flow laws

outlined here.

Table 6.1: Quantitative composition of synthesized HIP samples from electron microprobe measurements in wt% oxides.

	magnetite	rim	matrix
TiO_2	0.109	-	-
Na_2O	0.044	2.059	1.898
Al_2O_3	6.193	27.293	32.897
FeO[1]	84.408	1.224	0.434
NiO	0.037	0.018	0.067
CaO	0.088	12.800	16.081
SiO_2	0.264	55.988	48.282
MgO	1.088	0.166	0.126
Total	92.231	99.548	99.784

[1]Total iron as FeO.

Table 6.2: Deformation conditions.

Specimen	T (°C)	γ	$\dot{\gamma}$ (s^{-1})	σ_{max} (MPa)	σ_{avg} (MPa)	Avg. viscosity[1] (Pa·s)
IsoJT08-011-02b	1100	1	8.49×10^{-05}	56	47.2	5.56×10^{11}
IsoJT08-011-03b	1100	2	1.13×10^{-04}	68.5	61.7	5.45×10^{11}
IsoJT08-011-04b	1100	3	1.56×10^{-04}	44	50.5	3.24×10^{11}
IsoJT08-011-05b	1000	1	8.49×10^{-05}	127	87.5	1.03×10^{12}
IsoJT08-011-06b	1200	1	1.13×10^{-04}	19	10.1	8.9×10^{10}
IsoJT08-011-08b	1200	1.72	1.41×10^{-04}	23	13.4	9.46×10^{10}

[1] Avg. viscosity = $\sigma_{avg}/\dot{\gamma}$.

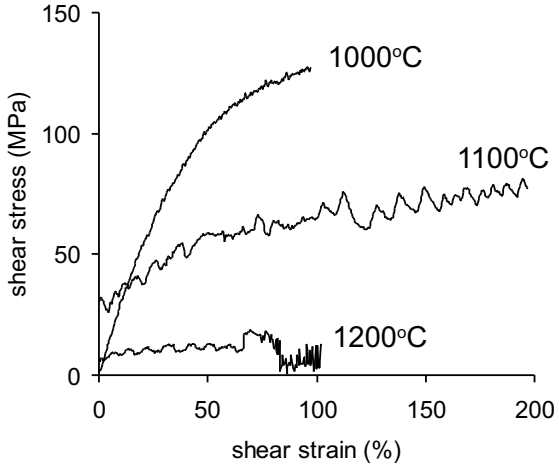

Figure 6.1: Representative stress *vs* strain curves for individual deformation experiments.

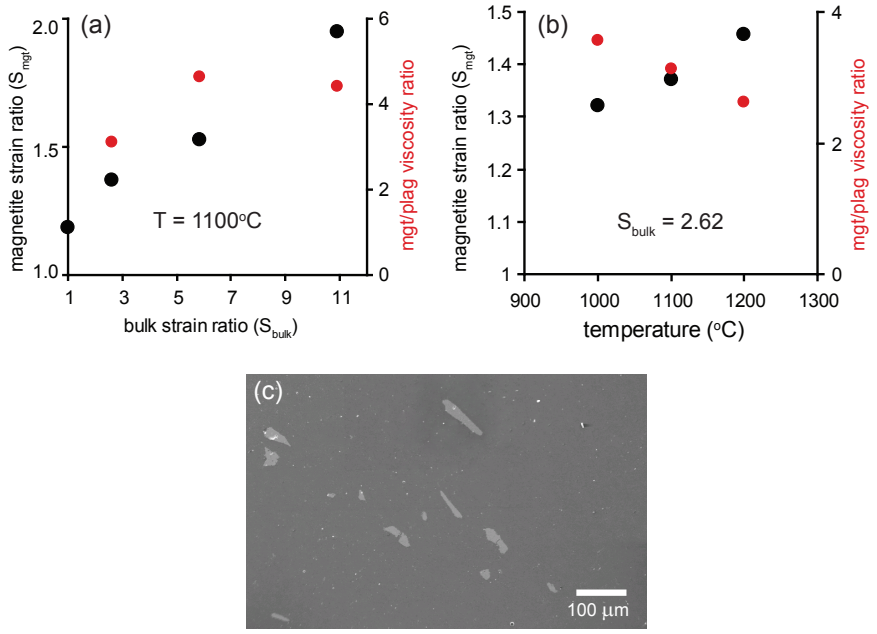

Figure 6.2: Magnetite shape-preferred orientations given by the mean grain shape ratio (black symbols) and the inferred magnetite/plagioclase viscosity ratios (red symbols) as a function of a) shear strain and b) temperature. c) Scanning electron microscope image taken from a cross-sectional shear zone surface showing the elongation of magnetite particles (brighter phase) in the plagioclase matrix after deformation at 1200°C. Additional photomicrographs illustrating SPO in magnetite before and after deformation are shown in Figure 5.7b.

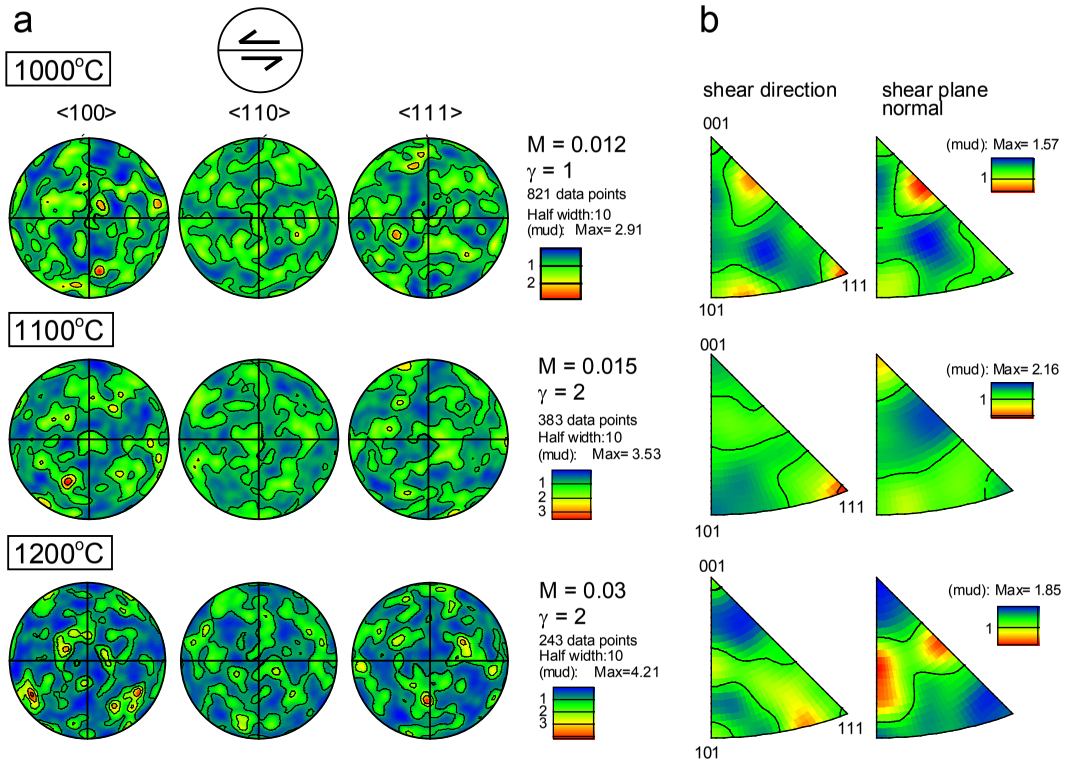

Figure 6.3: a) Pole figures for <100>, <110>, and <111> directions in magnetite. Plots are equal-area lower-hemisphere projections and use a Gaussian smoothing with a half-width of 10°. Contours are based on multiples of uniform density (mud). b) Inverse pole figures for magnetite using the same data in a). Pole figure data have been rotated from the acquisition surface to show the pole figures in relation to the shear geometry.

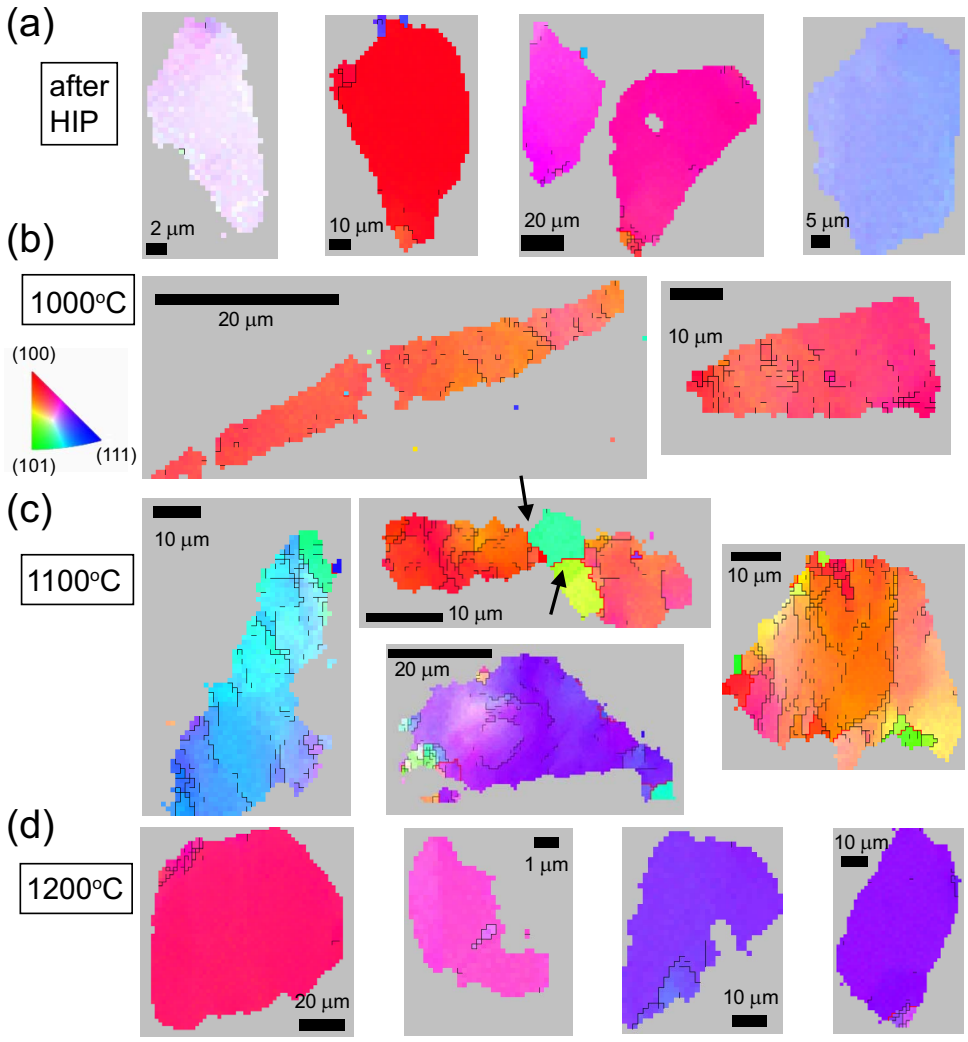

Figure 6.4: EBSD maps of magnetite grains in a) HIPed sample material and samples deformed at b) 1000°C, c) 1100°C and d) 1200°C. Black and red lines represent misorientations >1.5° and >10°, respectively. Map colors correspond to orientation according to the inverse pole figure coloring scheme for the direction normal to the acquisition surface. Arrows in c) highlight high-angle grain boundaries in a polycrystalline particle.

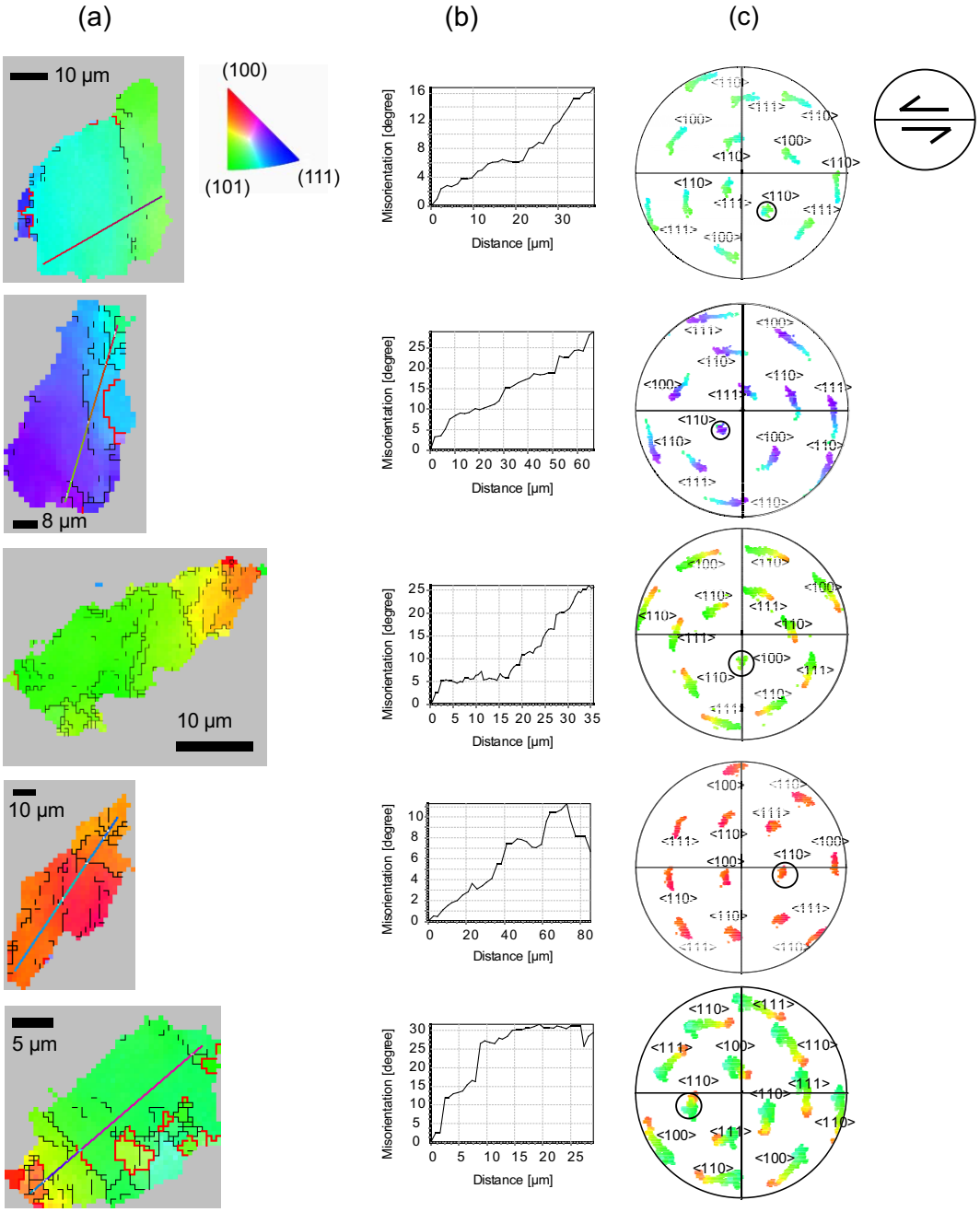
(a)
(b)
(c)
10 μm
(100)
(101)
(111)
8 μm
10 μm
10 μm
5 μm
Misorientation [degree]
Distance [μm]
<100>
<110>
<111>

Figure 6.5

: Figure 6.5: Details of misorientation and subgrain microstructure from EBSD maps on individual magnetite grains deformed at 1100°C. a) Orientation map using inverse pole figure coloring. Grain and subgrain boundaries are as in Figure 6.4. b) Cumulative misorientation profiles across areas indicated by grey lines in a). c) Composite pole figures of <100>, <110>, and <111> directions for grains in a) showing systematic rotation of grain orientations around a dispersion axis subparallel to the shear plane. Some data in c) have been rotated from the acquisition surface to show the relationship between the orientation dispersions and the shear geometry. Colors in c) do not indicate orientation; rather they correspond to the grain locations on the EBSD maps shown in a).

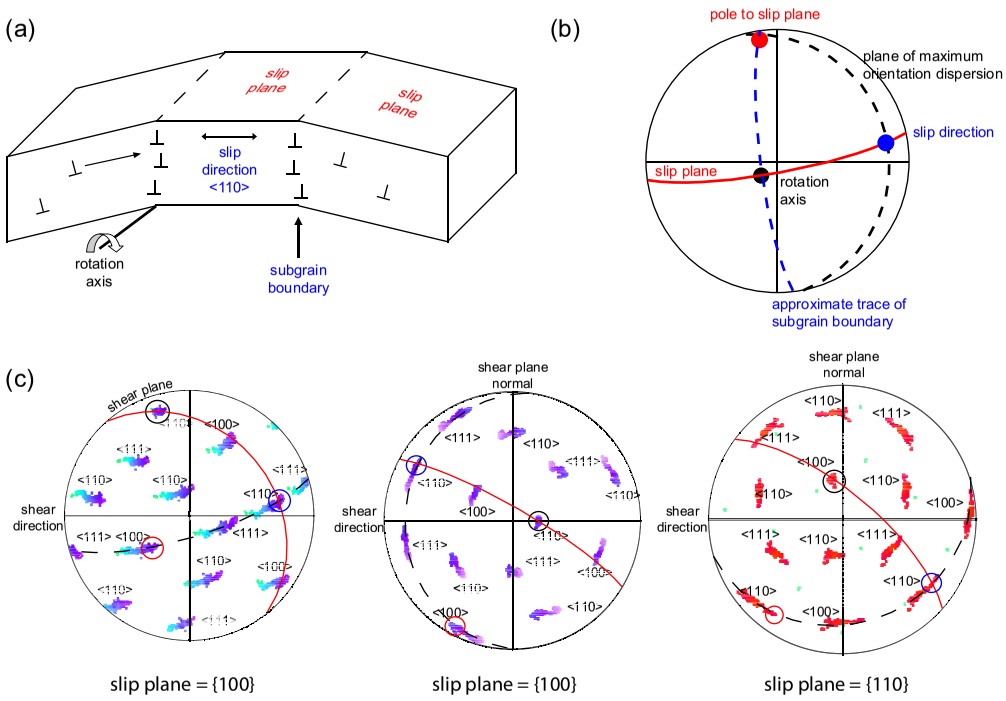

Figure 6.6: Schematic diagram illustrating the method of misorientation analysis. a) Geometric relationships between slip plane, slip direction, and the dispersion of grain orientations about a rotation axis for low-angle subgrain boundaries formed by edge dislocations. b) Stereoplot of planes and directions shown in a). c) Pole plots containing EBSD data from individual magnetite grains deformed at 1100°C showing active slip planes determined with misorientation analysis with rotation axes circled in black, pole to slip plane circled in red, and slip direction circled in blue. Slip directions for magnetite are constrained to <110> directions.

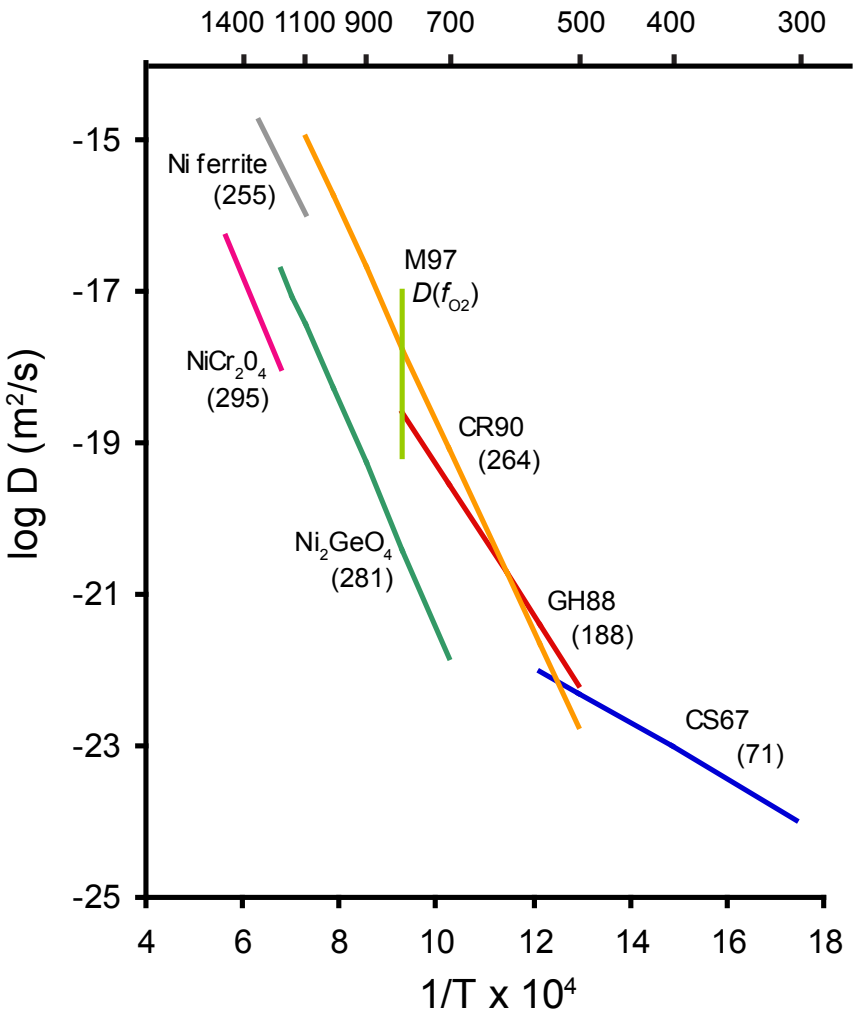

Figure 6.7: Arrhenius diagram of published rate laws for oxygen diffusion in magnetite and other spinel-structured phases. Activation energies in kJ/mol are labeled in parentheses. The vertical line labeled M97 represents diffusivities measured over a range of f_{O_2} at a constant temperature from (Millot et al., 1997). Other data sources are as follows: NiCr2O4 (Kingery et al., 1960); Ni-ferrite (O′Bryan & DiMarcello, 1970); CR90 (Crouch & Robertson, 1990); CS67 (Castle & Surman, 1967); Ni_2GeO_4 (Lawlis et al., 2001); GH88 (Giletti & Hess, 1988)

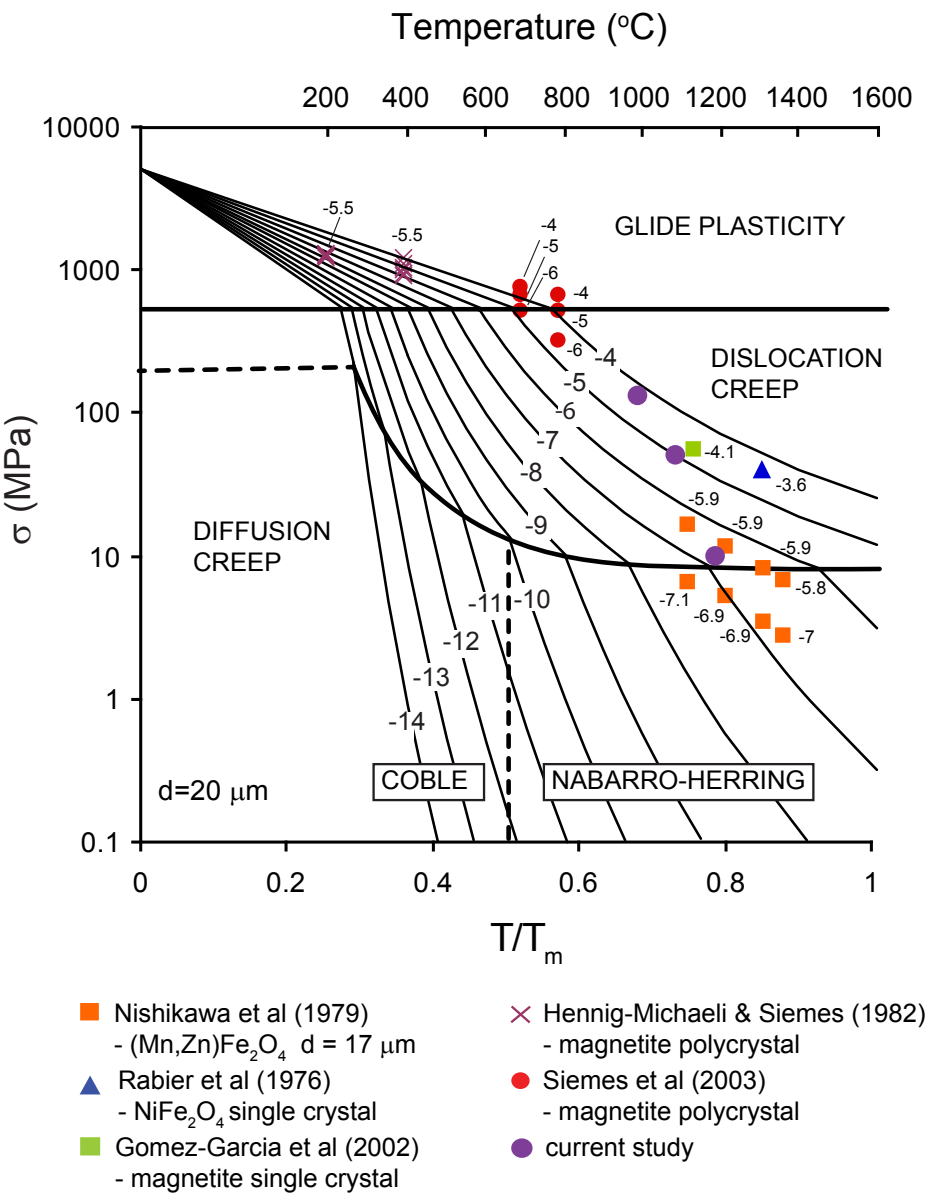

Figure 6.8: Deformation mechanism map for magnetite with a grain size of 20 μm. Contour lines and discrete data points are labeled in units of log strain rate.

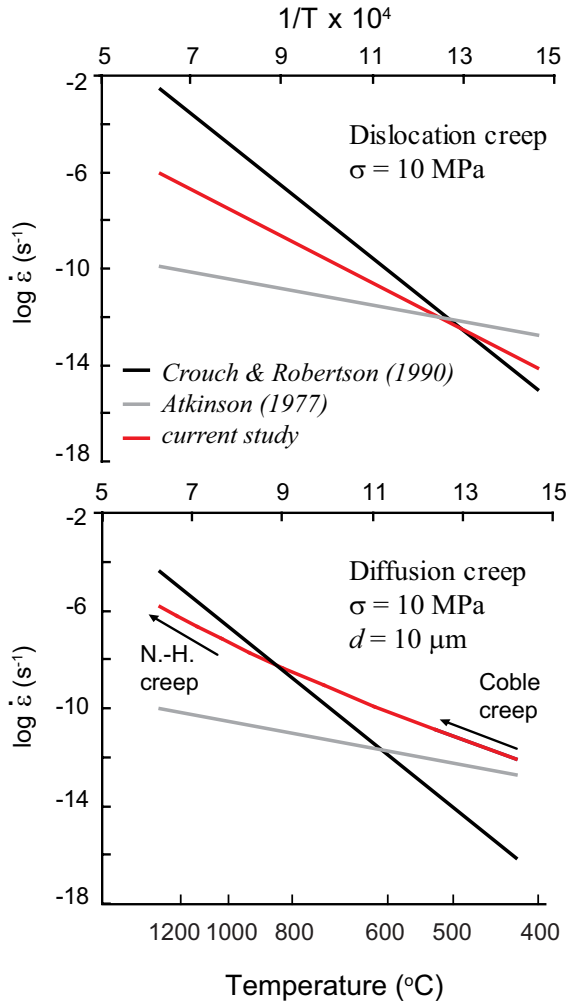

Figure 6.9: Arrhenius diagrams showing rate laws for magnetite creep according to flow laws proposed by Atkinson (1977) (grey lines), Crouch & Robertson (1990) (black lines), and the current study (red lines) for a) dislocation creep at a different stress of 10 MPa and b) diffusion creep at a differential stress of 10 MPa and grain size of 10 μm. The rate laws from Crouch & Robertson (1990) are normalized to an oxygen fugacity of a mixture of 1.5%CO in CO_2.

Chapter 7

Conclusion

The work presented in this thesis answers several questions related to the behavior of magnetite during deformation and the conditions and characteristics associated with the high-temperature growth of single-domain magnetite particles. However, the results raise as many new questions as they answer and provide an impetus for several topics of future study.

Firstly, the uncertainty of the upper grain-size limit for single-domain magnetic behavior in highly elongated grains on the micron scale is a critical gap in rock magnetism. Study of the magnetic domain structure of highly elongated magnetite grains is crucial for interpretation of magnetic properties in rocks and sediments containing fine magnetic particles. The discussion section in Chapter 2 illustrates the need to identify the threshold size and shape for single domain behavior in order to distinguish the effects of grain-size dependence on magnetic properties from other complicating effects such as those of interactions or stress. As seen in Chapter 3, determination of the single domain threshold for microscale magnetite needles is crucial for identifying the potential for chemical remanence acquisition in rocks where magnetic particle growth may have occurred near the Curie temperature during exsolution. Knowledge of the size transition from single-domain to pseudo-single domain structure will improve evaluations of the magnetic fidelity of such rocks and their practicality for use in paleomagnetism. A careful and systematic study of domain structure with high-resolution domain imaging techniques such as magnetic force microscopy or Lorentz microscopy in well-sized elongated magnetite should help to better demarcate the range of single domain behavior

in naturally-occurring magnetite.

Another question regarding magnetic domain structures in magnetite is whether internal microstructures in deformed magnetite, such as those imaged with EBSD in Chapter 6, are reflected in the magnetic microstructure. It remains to be seen whether domains can be imaged easily in Al-substituted magnetite or whether the cation substitution results in increased magnetostriction as in titanomagnetites, which show complex stress-controlled domain structures due to residual mechanical stresses induced by polishing. If changes in magnetostriction are slight in aluminomagnetite, the samples containing deformed magnetite will offer a unique opportunity to compare the magnetic microstructure of magnetic particles with the crystallographic microstructure by using domain imaging with magnetic force microscopy. This work would inform paleomagnetic studies on deformed terranes, as well as enhance understanding of the connection between crystalline defects and fundamental rock magnetic properties, such as magnetic remanence stability in magnetite.

A more pertinent problem of significance to paleomagnetism is determining the actual temperatures of nucleation and growth of Fe-oxide particles during exsolution from plagioclase. While indirect approaches such as the optimal phase boundary technique have been used to estimate exsolution temperatures of magnetite in pyroxene (Fleet et al., 1980; Feinberg et al., 2004), a more quantitative approach to the problem may be a geochemical study of equilibrium trace element concentrations at various temperatures. Once a pattern of Fe partitioning in plagioclase as a function of temperature is determined, it may then be scaled down to determine the low-temperature solubility of Fe and other trace element metals, and identify the conditions favorable for magnetite exsolution. Such a study would also help determine whether Fe becomes insoluble due to decreases in temperature alone, or whether chemical factors such as changes in oxygen fugacity or hydrogen fugacity play a role as well.

In Chapter 4, discrepancies between anisotropy of susceptibility and anisotropy of remanence raise questions about the role of interactions and the potential for inverse fabrics in pseudo-single domain magnetite. Inverse fabrics are typically restricted to single-domain magnetite, and are the most frequent source of disagreement between the two magnetic fabric measurement methods. Similarly, strong magnetic interaction effects are typically only observed in single-domain magnetite, but some studies indicate

that certain magnetic properties are so sensitive to interactions that their effects are measurable in coarser particles, throughout the pseudo-single domain size range for magnetite. More work needs to be performed on truly non-interacting pseudo-single domain particles of known size to ascertain the extent of magnetic interactions in this grain-size interval. However, these data suggest that rock magnetism studies, including magnetic fabric analysis, should take interaction effects into consideration in in a much wider range of rocks than is typically done.

Lastly, the theoretical flow laws for magnetite outlined in Chapter 6 are likely to more accurately predict the deformation behavior of magnetite at high temperatures, but direct experimental data are needed to verify their accuracy. A simple series of creep experiments involving a range of different temperatures, differential stresses, and grain sizes will define the regions of dominant deformation mechanisms, and the true activation energy for creep from strain rates. Additionally, better determinations of strain partitioning between magnetite and silicates may be made from deformation experiments on samples containing systematically varying proportions of magnetite and silicate minerals. These systems may be representative of shear zones in oceanic core complexes that form important regions of strain localization along slow-spreading ocean ridges.

The ubiquitous occurrence of magnetite in soils, sediments, and crystalline rocks merits continued study of the physical processes that produce and transform it. Although vast advances have been made in understanding various aspects of mineralogy, geochemistry, and material magnetism related to magnetite, the underlying message in the collective results of this thesis is that much more remains to be learned.

References

Abart, R., Petrishcheva, E., Wirth, R., & Rhede, D. (2009). Exsolution by spinodal decomposition II: Perthite formation during slow cooling of anatexites from Ngoronghoro, Tanzania. *American Journal of Science*, 309(6), 450.

Agar, S. & Lloyd, G. (1997). Deformation of Fe-Ti oxides in gabbroic shear zones from the Mark area. In J. Karson, M. Cannat, D. Miller, & D. Elthon (Eds.), *Proceedings of the Ocean Drilling Program, Scientific Results*, volume 153 (pp. 123–141).

Aragòn, R., Buttrey, D. J., Shepherd, J. P., & Honig, J. M. (1985). Influence of nonstoichiometry on the Verwey transition. *Physics Review B*, 31(1), 430.

Armbrustmacher, T. & Banks, N. (1974). Clouded plagioclase in metadolerite dikes, Southeastern Bighorn Mountains, Wyoming. *American Mineralogist*, 59, 656–665.

Atkinson, B. K. (1977). The kinetics of ore deformation: Its illustration and analysis by means of deformation-mechanism maps. *Geologiska Foreningens i Stockholm Forhandlingar*, 99, Part 2(569), 186–197.

Banerjee, S., King, J., & Marvin, J. (1981). A rapid method for magnetic granulometry with applications to environmental studies. *Geophysical Research Letters*, 8(4), 333–336.

Barbosa, P. F. & Lagoeiro, L. (2010). Crystallographic texture of the magnetite-hematite transformation: Evidence for topotactic relationships in natural samples from Quadrilatero Ferrifero, Brazil. *American Mineralogist*, 95(1), 118–125.

Barnhoorn, A., Bystricky, M., Burlini, L., & Kunze, K. (2004). The role of recrystallisation on the deformation behaviour of calcite rocks: Large strain torsion experiments on Carrara marble. *Journal of Structural Geology*, 26(5), 885–903.

Beaty, D. & Albee, A. (1980). Silica solid solution and zoning in natural plagioclase. *American Mineralogist*, 65(1-2), 63.

Behrens, H., Johannes, W., & Schmalzried, H. (1990). On the mechanisms of cation diffusion processes in ternary feldspars. *Physics and Chemistry of Minerals*, 17(1), 62–78.

Birch, F. (1966). Compressibility; elastic constants. *Handbook of Physical Constants*, 97, 97–173.

Boone, G. (1969). Origin of clouded red feldspars: Petrologic contrasts in a granitic porphyry intrusion. *American Journal of Science*, 267(6), 633.

Borradaile, G. & Mothersill, J. (1989). Tectonic strain and paleomagnetism: Experimental investigation. *Physics of the Earth and Planetary Interiors*, 56(3-4), 254–265.

Borradaile, G. & Mothersill, J. (1991). Experimental strain of isothermal remanent magnetization in ductile sandstone. *Physics of the Earth and Planetary Interiors*, 65(3-5), 308–318.

Borradaile, G. J. (1988). Magnetic susceptibility, petrofabrics and strain. *Tectonophysics*, 156(1-2), 1–20.

Borradaile, G. J. (1994). Remagnetisation of a rock analogue during experimental triaxial deformation. *Physics of the Earth and Planetary Interiors*, 83(2), 147–163.

Borradaile, G. J. (1996). Experimental stress remagnetization of magnetite. *Tectonophysics*, 261(4), 229–248.

Borradaile, G. J. & Alford, C. (1987). Relationship between magnetic susceptibility and strain in laboratory experiments. *Tectonophysics*, 133(1-2), 121–135.

Borradaile, G. J. & Alford, C. (1988). Experimental shear zones and magnetic fabrics. *Journal of Structural Geology*, 10, 895–904.

Borradaile, G. J. & Jackson, M. (1993). Changes in magnetic remanence during simulated deep sedimentary burial. *Physics of the Earth and Planetary Interiors*, 77(3-4), 315–327.

Borradaile, G. J. & Jackson, M. (2004). Anisotropy of magnetic susceptibility (AMS): magnetic petrofabrics of deformed rocks. In F. Martin-Hernandez, C. M. Lueneburg, C. Aubourg, & M. Jackson (Eds.), *Magnetic Fabric: Methods and Applications*, volume 238 of *Special Publications* (pp. 299–360). London: Geological Society of London.

Bouchez, J. (1997). Granite is never isotropic. *Granite: from Segregation of Melt to Emplacement Fabrics. Kluwer Academic, Dordrecht*, (pp. 95–112).

Bridgwater, D. & Harry, W. (1968). *Anorthosite Xenoliths and Plagioclase Megacrysts in Precambrian Intrusions of South Greenland.* CA Reitzel.

Broese Van Groenou, A. & Kadijk, S. (1989). Slip patterns made by sphere indentations on single crystal MnZn ferrite. *Acta Metallurgica*, 37(10), 2613–2624.

Bryan, W. (1974). Fe-Mg relationships in sector-zoned submarine basalt plagioclase. *Earth and Planetary Science Letters*, 24(2), 157–165.

Burns, D. (1966). Chemical and mineralogical changes associated with the Laxfordian metamorphism of dolerite dykes in the Scourie-Loch Laxford area, Sutherland, Scotland. *Geological Magazine*, 103, 19–35.

Butler, R. & Banerjee, S. (1975). Theoretical single-domain grain size range in magnetite and titanomagnetite. *Journal of Geophysical Research*, 80(29), 4049–4058.

Byers, F., Carr, W., Orkild, P., Quinlivan, W., & Sargent, K. (1976). *Volcanic Suites and Related Cauldrons of Timber Mountain-Oasis Valley Caldera Complex, Southern Nevada.* United States Government Print Office.

Castle, J. & Surman, P. (1967). Self-diffusion of oxygen in magnetite. Techniques for sampling and isotopic analysis of micro quantities of water. *The Journal of Physical Chemistry*, 71(13), 4255–4259.

Castle, J. & Surman, P. (1969). Self-diffusion of oxygen in magnetite. Effect of anion vacancy concentration and cation distribution. *The Journal of Physical Chemistry*, 73(3), 632–634.

Charpentier, P., Rabbe, P., & Manenc, J. (1968). Mise en evidence de la plasticite de la magnetite mesure de la durete en fonction de la temperature. *Materials Research Bulletin*, 3(2), 69–78.

Cherniak, D. (2003). Silicon self-diffusion in single-crystal natural quartz and feldspar. *Earth and Planetary Science Letters*, 214(3-4), 655–668.

Cherniak, D. (2010). Cation diffusion in feldspars. *Reviews in Mineralogy and Geochemistry*, 72(1), 691.

Cherniak, D. & Watson, E. (1994). A study of strontium diffusion in plagioclase using rutherford backscattering spectroscopy. *Geochimica et Cosmochimica Acta*, 58(23), 5179–5190.

Cherniak, D., Watson, E., & Wark, D. (2007). Ti diffusion in quartz. *Chemical Geology*, 236(1-2), 65–74.

Chokshi, A. (1988). Critical appraisal of diffusivity determinations from experimental creep data. *Journal of the American Ceramic Society*, 71(5).

Christoffersen, R., Yund, R., & Tullis, J. (1983). Inter-diffusion of K and Na in alkali feldspars: Diffusion couple experiments. *American Mineralogist*, 68(11-12), 1126.

Cogné, J. P. & Perroud, H. (1988). Anisotropy of magnetic susceptibility as a strain gauge in the Flamanville granite, NW France. *Physics of the Earth and Planetary Interiors*, 51(4), 264–270.

Coogan, L., Jenkin, G., & Wilson, R. (2002). Constraining the cooling rate of the lower oceanic crust: A new approach applied to the Oman ophiolite. *Earth and Planetary Science Letters*, 199(1-2), 127–146.

Crank, J. (1975). *The Mathematics of Diffusion, 2nd edn.* Oxford.

Crouch, A. & Robertson, J. (1990). Creep and oxygen diffusion in magnetite. *Acta Metallurgica et Materialia*, 38(12), 2567–2572.

Davis, K. (1981). Magnetite rods in plagioclase as the primary carrier of stable NRM in ocean floor gabbros. *Earth and Planetary Science Letters*, 55(1), 190–198.

Day, R., Fuller, M., & Schmidt, V. (1977). Hysteresis properties of titanomagnetites: grain-size and compositional dependence. *Physics of the Earth and Planetary Interiors*, 13(4), 260–267.

de Bresser, J. H. P. & Spiers, C. J. (1993). Slip systems in calcite single crystals deformed at 300-800°C. *Journal of Geophysical Research*, 98(B4), 6397–6409.

Dieckmann, R. & Schmalzried, H. (1977). Defects and cation diffusion in magnetite (I). *Berichte der Bunsengesellschaft für physikalische Chemie*, 81(3), 344–347.

Doolittle, L. (1985). Algorithms for the rapid simulation of Rutherford backscattering spectra. *Nuclear Instruments and Methods in Physics Research*, B9, 334.

Draeger, U., Prévot, M., Poidras, T., & Riisager, J. (2006). Single-domain chemical, thermochemical and thermal remanences in a basaltic rock. *Geophysical Journal International*, 166(1), 12–32.

Duclos, R., Doukhan, N., & Escaig, B. (1978). High temperature creep behaviour of nearly stoichiometric alumina spinel. *Journal of Materials Science*, 13(8), 1740–1748.

Dunlop, D. (1984). A method of determining demagnetizing factor from multidomain hysteresis. *Journal of Geophysical Research*, 89(B1), 553–558.

Dunlop, D. (1986). Hysteresis properties of magnetite and their dependence on particle size: A test of pseudo-single-domain remanence models. *Journal of Geophysical Research*, 91(B9), 9569–9584.

Dunlop, D. (2002). Theory and application of the Day plot (M_{rs}/M_s versus H_{cr}/H_c) 1. Theoretical curves and tests using titanomagnetite data. *Journal of Geophysical Research*, 107(B3), 2056.

Dunlop, D. & Argyle, K. (1997). Thermoremanence, anhysteretic remanence and susceptibility of submicron magnetites: Nonlinear field dependence and variation with grain size. *Journal of Geophysical Research*, 102(20), 199–20.

Dunlop, D. & Carter-Stiglitz, B. (2006). Day plots of mixtures of superparamagnetic, single-domain, pseudosingle-domain, and multidomain magnetites. *Journal of Geophysical Research*, 111.

Dunlop, D., Newell, A., & Enkin, R. (1994). Transdomain thermoremanent magnetization. *Journal of Geophysical Research*, 99, 19–19.

Dunlop, D. J. (1983). On the demagnetizing energy and demagnetizing factor of a multidomain ferromagnetic cube. *Geophysical Research Letters*, 10(1), 79–82.

Dunlop, D. J. & Özdemir, O. (1997). *Rock Magnetism: Fundamentals and Frontiers*. Cambridge Univeristy Press.

Egli, R. (2003). Analysis of the field dependence of remanent magnetization curves. *Journal of Geophysical Research*, 108(B2), 2081.

Egli, R. (2004). Characterization of individual rock magnetic components by analysis of remanence curves, 1. Unmixing natural sediments. *Studia Geophysica et Geodaetica*, 48(2), 391–446.

Egli, R. (2006). Theoretical considerations on the anhysteretic remanent magnetization of interacting particles with uniaxial anisotropy. *Journal of Geophysical Research*, 111(B12), S18.

Egli, R. & Lowrie, W. (2002). Anhysteretic remanent magnetization of fine magnetic particles. *Journal of Geophysical Research*, 108(B2).

Evans, M., Lewchuk, M., & Elmore, R. (2003). Strain partitioning of deformation mechanisms in limestones: Examining the relationship of strain and anisotropy of magnetic susceptibility (AMS). *Journal of Structural Geology*, 25(9), 1525–1549.

Fabian, K. (2009). Thermochemical remanence acquisition in single-domain particle ensembles: A case for possible overestimation of the geomagnetic paleointensity. *Geochemistry Geophysics Geosystems*, 10(6), Q06Z03.

Fabian, K., Kirchner, A., Williams, W., Heider, F., Leibl, T., & Huber, A. (1996). Three-dimensional micromagnetic calculations for magnetite using FFT. *Geophysical Journal International*, 124(1), 89–104.

Feinberg, J., Scott, G., Renne, P., & Wenk, H. (2005). Exsolved magnetite inclusions in silicates: Features determining their remanence behavior. *Geology*, 33(6), 513.

Feinberg, J., Wenk, H., Renne, P., & Scott, G. (2004). Epitaxial relationships of clinopyroxene-hosted magnetite determined using electron backscatter diffraction (EBSD) technique. *American Mineralogist*, 89(2-3), 462.

Fleet, M. (1981). The structure of magnetite. *Acta Crystallographica Section B: Structural Crystallography and Crystal Chemistry*, 37(4), 917–920.

Fleet, M., Bilcox, G., & Barnett, R. (1980). Oriented magnetite inclusions in pyroxenes from the grenville province. *Canadian Mineralogist*, 18(1), 89.

Frandsen, C., Stipp, S., McEnroe, S., Madsen, M., & Knudsen, J. (2004). Magnetic domain structures and stray fields of individual elongated magnetite grains revealed by magnetic force microscopy (MFM). *Physics of the Earth and Planetary Interiors*, 141(2), 121–129.

Frost, B. R. (1991). Introduction to oxygen fugacity and its petrologic importance. In D. Lindsley (Ed.), *Oxide Minerals: Petrologic and Magnetic Significance*, volume 25 of *Rev. Mineral. Geochem.* (pp. 1–9). Washington, DC: Mineralogical Society of America.

Frost, H. & Ashby, M. (1982). *Deformation Mechanism Maps: The Plasticity and Creep of Metals and Ceramics*. Pergamon press.

Gay, N. (1968). Pure shear and simple shear deformation of inhomogeneous viscous fluids. 1. Theory. *Tectonophysics*, 5(3), 211–234.

Gee, J. & Kent, D. (2007). Source of oceanic magnetic anomalies and the geomagnetic polarity timescale. *Treatise on Geophysics*, 5, 455–507.

Geissman, J., Harlan, S. S., & Brearly, A. (1988). The physical isolation and identification of carriers of geologically stable remanent magnetization: Paleomagnetic and

rock magnetic microanalysis and electron microscopy. *Geophysical Research Letters*, 15(5), 479–482.

Giletti, B. & Hess, K. (1988). Oxygen diffusion in magnetite. *Earth and Planetary Science Letters*, 89(1), 115–122.

Giletti, B. & Shanahan, T. (1997). Alkali diffusion in plagioclase feldspar. *Chemical Geology*, 139(1-4), 3–20.

Gómez-García, D., Dominguez-Rodriguez, A., Castaing, J., & Millot, F. (2002). The influence of oxygen partial pressure on recovery creep in magnetite single crystals. *Journal of Physics and Chemistry of Solids*, 63(2), 185–191.

Graham, J. (1966). Significance of magnetic anisotropy in Appalachian sedimentary rocks. In J. Steinhart & T. Smith (Eds.), *The Earth Beneath the Continents*, volume 10 of *Geophysical Monograph* (pp. 627–648). Washington, DC: American Geophysical Union.

Grove, T. (1982). Use of exsolution lamellae in lunar clinopyroxenes as cooling rate speedometers: An experimental calibration. *American Mineralogist*, 67, 251–268.

Grove, T. & Bence, A. (1979). Crystallization kinetics in a multiply saturated basalt magma-an experimental study of Luna 24 ferrobasalt. In *Lunar and Planetary Science Conference Proceedings*, volume 10 (pp. 439–478).

Halls, H., Kumar, A., Srinivasan, R., & Hamilton, M. (2007). Paleomagnetism and U-Pb geochronology of easterly trending dykes in the Dharwar craton, India: feldspar clouding, radiating dyke swarms and the position of India at 2.37 Ga. *Precambrian Research*, 155(1-2), 47–68.

Halls, H., McArdle, N., Gratton, M., Hill, M., & Shaw, J. (2004). Microwave paleointensities from dyke chilled margins: A way to obtain long-term variations in geodynamo intensity for the last three billion years. *Physics of the Earth and Planetary Interiors*, 147(2-3), 183–195.

Handy, M. (1990). The solid-state flow of polymineralic rocks. *Journal of Geophysical Research*, 95(B6), 8647–8661.

Hargraves, R., Johnson, D., & Chan, C. Y. (1991). Distribution anisotropy: The cause of AMS in igneous rocks? *Geophysical Research Letters*, 18(12), 2193–2196.

Harlow, G. & Klimentidis, R. (1980). Clouding of pyroxene and plagioclase in eucrites - Implications for post-crystallization processing. In *Lunar and Planetary Science Conference Proceedings*, volume 11 (pp. 1131–1143).

Harrison, R. & Feinberg, J. (2008). FORCinel: An improved algorithm for calculating first-order reversal curve distributions using locally weighted regression smoothing. *Geochemistry Geophysics Geosystems*, 9, Q05016.

Hayden, L., Watson, E., & Wark, D. (2008). A thermobarometer for sphene (titanite). *Contributions to Mineralogy and Petrology*, 155(4), 529–540.

Heider, F. & Dunlop, D. (1987). Two types of chemical remanent magnetization during the oxidation of magnetite. *Physics of the Earth and Planetary Interiors*, 46(1-3), 24–45.

Heider, F., Dunlop, D., & Sugiura, N. (1987). Magnetic properties of hydrothermally recrystallized magnetite crystals. *Science*, 236(4806), 1287.

Heider, F., Zitzelsberger, A., & Fabian, K. (1996). Magnetic susceptibility and remanent coercive force in grown magnetite crystals from 0.1μm to 6 mm. *Physics of the Earth and Planetary Interiors*, 93(3-4), 239–256.

Hennig-Michaeli, C. & Siemes, H. (1975). Zwillungsgleitung beim Magnetite. *Neues Jahrbuch Mineralogie Abhandlungen*, 123, 330–334.

Hennig-Michaeli, C. & Siemes, H. (1982). Compression experiments on natural magnetite crystals at 200°C and 400°C at 400 MPa confining pressure. In *Issues in rock mechanics: Proceedings, twenty-third Symposium on Rock Mechanics, the University of California, Berkeley, California, August 25-27, 1982* (pp. 380).: Random House Trade.

Heslop, D., Dekkers, M., Kruiver, P., & Van Oorschot, I. (2002). Analysis of isothermal remanent magnetization acquisition curves using the expectation–maximization algorithm. *Geophysical Journal International*, 148(1), 58–64.

Hodych, J. (1986). Determination of self-demagnetizing factor N for multidomain magnetite grains in rock. *Physics of the Earth and Planetary Interiors*, 41(4), 283–291.

Hofmeister, A. & Rossman, G. (1984). Determination of Fe^{3+} and Fe^{2+} concentrations in feldspar by optical absorption and EPR spectroscopy. *Physics and Chemistry of Minerals*, 11(5), 213–224.

Hornstra, J. (1960). Dislocations, stacking faults and twins in the spinel structure. *Journal of Physics and Chemistry of Solids*, 15(3-4), 311–323.

Housen, B. A., Pluijm, B. A. V. D., & Essene, E. J. (1995). Plastic behavior of magnetite and high strains obtained from magnetic fabrics in the Parry Sound shear zone, Ontario Grenville Province. *Journal of Structural Geology*, 17(2), 265–278.

Hrouda, F. (1993). Theoretical models of magnetic anisotropy to strain relationship revisited. *Physics of the Earth and Planetary Interiors*, 77(3-4), 237–249.

Hrouda, F. & Lanza, R. (1989). Magnetic fabric in the Biella and Traversella stocks (Periadriatic Line) : Implications for the mode of emplacement. *Physics of the Earth and Planetary Interiors*, 56(3-4), 337–348.

Hunt, C., Banerjee, S., Han, J., Solheid, P., Oches, E., Sun, W., & Liu, T. (1995a). Rock-magnetic proxies of climate change in the loess-palaeosol sequences of the western Loess Plateau of China. *Geophysical Journal International*, 123(1), 232–244.

Hunt, C., Moskowitz, B., & Banerjee, S. (1995b). Magnetic properties of rocks and minerals. *Rock Physics and Phase Relations: A Handbook of Physical Constants*, 3, 189–204.

Hustoft, J. W. & Kohlstedt, D. L. (2006). Metal-silicate segregation in deforming dunitic rocks. *Geochemistry, Geophysics, Geosystems*, 7(2).

Jackson, M., Borradaile, G. J., Hudleston, P., & Banerjee, S. (1993). Experimental deformation of synthetic magnetite-bearing calcite sandstones; Effects on remanence, bulk magnetic properties, and magnetic anisotropy. *Journal of Geophysical Research*, 98(B1), 383–401.

Jackson, M., Carter-Stiglitz, B., Egli, R., & Solheid, P. (2006). Characterizing the superparamagnetic grain distribution $f(V, Hk)$ by thermal fluctuation tomography. *Journal of Geophysical Research*, 111(B12), B12S07.

Jackson, M., Moskowitz, B., Rosenbaum, J., & Kissel, C. (1998). Field-dependence of AC susceptibility in titanomagnetites. *Earth and Planetary Science Letters*, 157, 129–139.

Jelinek, V. (1981). Characterization of the magnetic fabric of rocks. *Tectonophysics*, 79(3-4), T63–T67.

Johnson, E. (2006). Water in nominally anhydrous crustal minerals: Speciation, concentration, and geologic significance. *Reviews in Mineralogy and Geochemistry*, 62(1), 117.

King, J., Banerjee, S., Marvin, J., & Özdemir, O. (1982). A comparison of different magnetic methods for determining the relative grain size of magnetite in natural materials: Some results from lake sediments. *Earth and Planetary Science Letters*, 59(2), 404–419.

Kingery, W., Hill, D., & Nelson, R. (1960). Oxygen mobility in polycrystalline $NiCr_2O_4$ and α-Fe_2O_3. *J. Am. Ceram. Soc*, 43, 473–476.

Kligfield, R., Lowrie, W., Hirt, A., & Siddans, A. W. B. (1983). Effect of progressive deformation on remanent magnetization of Permian redbeds from the Alpes Maritimes (France). *Tectonophysics*, 98(1-2), 59–85.

Kligfield, R., Owens, W., & Lowrie, W. (1981). Magnetic susceptibility anisotropy, strain, and progressive deformation in Permian sediments from the Maritime Alps (France). *Earth and Planetary Science Letters*, 55, 181–189.

Kneen, S. J. (1976). The relationship between the magnetic and strain fabrics of some haematite-bearing Welsh slates. *Earth and Planetary Science Letters*, 31(3), 413–416.

Kohler, T. & Brey, G. (1990). Calcium exchange between olivine and clinopyroxene calibrated as a geothermobarometer for natural peridotites from 2 to 60 kb with applications. *Geochimica et Cosmochimica Acta*, 54(9), 2375–2388.

Kosterov, A. (2003). Low-temperature magnetization and AC susceptibility of magnetite: Effect of thermomagnetic history. *Geophysical Journal International*, 154(1), 58–71.

Launeau, P. & Cruden, A. (1998). Magmatic fabric acquisition mechanisms in a syenite: Results of a combined anisotropy of magnetic susceptibility and image analysis study. *Journal of Geophysical Research*, 103(B3), 5067–5089.

Launeau, P. & Robin, P. (1996). Fabric analysis using the intercept method. *Tectonophysics*, 267(1-4), 91–119.

Lawlis, J., Zhao, Y., & Karato, S. (2001). High-temperature creep in a Ni_2GeO_4: A contribution to creep systematics in spinel. *Physics and Chemistry of Minerals*, 28(8), 557–571.

Levi, S. & Merrill, R. (1976). A comparison of ARM and TRM in magnetite. *Earth and Planetary Science Letters*, 32(2), 171–184.

Lewis, M. (1966). Defects in spinel crystals grown by the verneuil process. *Philosophical Magazine*, 14, 1003–1018.

Lindsley, D. (1991). Experimental studies of oxide minerals. *Reviews in Mineralogy and Geochemistry*, 25(1), 69.

Lloyd, G., Farmer, A., & Mainprice, D. (1997). Misorientation analysis and the formation and orientation of subgrain and grain boundaries. *Tectonophysics*, 279(1-4), 55–78.

Longhi, J., Walker, D., & Hays, J. (1976). Fe and Mg in plagioclase. In *Lunar and Planetary Science Conference Proceedings*, volume 7 (pp. 1281–1300).

Lundgaard, K. & Tegner, C. (2004). Partitioning of ferric and ferrous iron between plagioclase and silicate melt. *Contributions to Mineralogy and Petrology*, 147(4), 470–483.

Maher, B. (1988). Magnetic properties of some synthetic sub-micron magnetites. *Geophysical Journal International*, 94(1), 83–96.

Mamtani, M., Mukherji, A., & Chaudhuri, A. (2007). Microstructures in a banded iron formation (Gua mine, India). *Geological Magazine*, 144(2), 271.

McClelland, E. (1996). Theory of CRM acquired by grain growth, and its implications for TRM discrimination and palaeointensity determination in igneous rocks. *Geophysical Journal International*, 126(1), 271–280.

Means, W., Hobbs, B., Lister, G., & Williams, P. (1980). Vorticity and non-coaxiality in progressive deformations. *Journal of Structural Geology*, 2(3), 371–378.

Mehl, L. & Hirth, G. (2008). Plagioclase preferred orientation in layered mylonites: Evaluation of flow laws for the lower crust. *Journal of Geophysical Research*, 113(5).

Merrill, R. T. (1977). The demagnetizing field of multidomain magnetite. *J. Geomag. Geoelectr.*, 29(4), 285–292.

Millot, F., Lorin, J., Klossa, B., Niu, Y., & Tarento, J. (1997). Oxygen self-diffusion in Fe_3O_4: An experimental example of interactions between defects. *Berichte der Bunsen-Gesellschaft*, 101(9), 1351–1354.

Millot, F. & Niu, Y. (1997). Diffusion of O^{18} in Fe_3O_4: An experimental approach to study the behavior of minority defects in oxides. *Journal of Physics and Chemistry of Solids*, 58(1), 63–72.

Mishra, R. & Thomas, G. (1976). Lattice defects in lithium ferrite spinel. In R. Fulrath & J. J.A. Pask (Eds.), *Ceramic Microstructures, 1976, with Emphasis on Energy Related Applications: Proceedings of the Sixth International Materials Symposium Ceramic Microstructures' 76, Held at the University of California, Berkeley, August 24-27, 1976*, volume 1. Westview Press.

Mitchell, T., Hwang, L., & Heuer, A. (1976). Deformation in spinel. *Journal of Materials Science*, 11(2), 264–272.

Morales, L. F. G., Lagoeiro, L. E., & Endo, I. (2008). First results on the LPO-derived seismic properties of iron ores from the Quadrilatero Ferrifero region, southeastern Brazil. *Tectonophysics*, 460(1-4), 21–33.

Morgan, G. & Smith, P. (1981). Transmission electron microscope and rock magnetic investigations of remanence carriers in a precambrian metadolerite. *Earth and Planetary Science Letters*, 53(2), 226–240.

Moskowitz, B., Frankel, R., Flanders, P., Blakemore, R., & Schwartz, B. (1988). Magnetic properties of magnetotactic bacteria. *Journal of Magnetism and Magnetic Materials*, 73(3), 273–288.

Muller, P. & Siemes, H. (1972). Zur Festigkeit und Gefugeregulung von experimentell verformten Magnetiterzen. *Neues Jahrbuch Mineralogie Abhandlungen*, 117, 39–60.

Muxworthy, A. & Williams, W. (2009). Critical superparamagnetic/single-domain grain sizes in interacting magnetite particles: Implications for magnetosome crystals. *Journal of The Royal Society Interface*, 6(41), 1207.

Muxworthy, A. R. & Dunlop, D. J. (2002). First-order reversal curve (FORC) diagrams for pseudo-single-domain magnetites at high temperature. *Earth and Planetary Science Letters*, 203(1), 369–382.

Muxworthy, A. R. & Williams, W. (2004). Distribution anisotropy: The influence of magnetic interactions on the anisotropy of magnetic remanence. In F. Martin-Hernandez, C. M. Lueneburg, C. Aubourg, & M. Jackson (Eds.), *Magnetic Fabric: Methods and Applications*, volume 238 of *Special Publications* (pp. 37–47). London: Geological Society of London.

Nagata, T. (1961). *Rock Magnetism*. Tokyo: Maruzen.

Nakamura, N. & Borradaile, G. (2001). Do reduction spheroids predate finite strain? A magnetic diagnosis of Cambrian slates in North Wales. *Tectonophysics*, 304, 133–139.

Natland, J. (2002). Magnetic susceptibility as an index of the lithology and composition of gabbros, ODP Leg 176, Hole 735B, Southwest Indian Ridge. In *Proceedings of the Ocean Drilling Program, Scientific Results*, volume 176 (pp. 1–69).

Nishikawa, T. (1979). Diffusional creep of polycrystalline Ni-Zn ferrite of coarse grain. *Journal of the Ceramics Society of Japan*, 87(1010), 529.

Nishikawa, T. (1980). Dislocation climb-controlled creep of polycrystalline Mn-Zn ferrite. *Journal of the Ceramics Society of Japan*, 88(1021), 538.

O′Bryan, H. & DiMarcello, F. (1970). Oxygen diffusion in nickel ferrous ferrite. *Journal of the American Ceramic Society*, 53, 413–416.

Okamoto, Y. (1989). Creep deformation mechanisms in oxides and deformation of spinel ferrites. *Rheology of Solids and of the Earth. Oxford University Press, Oxford*, (pp. 83–104).

O′Reilly, W. (1984). Rock and Mineral Magnetism. *Blackie, Glasgow*, (pp. 220).

Osborn, J. A. (1945). Demagnetizing factors of the general ellipsoid. *Phys. Rev.*, 67(11-12), 351–357.

Owens, W. (1974). Mathematical model studies on factors affecting the magnetic anisotropy of deformed rocks. *Tectonophysics*, 24(1-2), 115–131.

Özdemir, O. & Banerjee, S. K. (1982). A preliminary magnetic study of soil samples from west-central Minnesota. *Earth and Planetary Science Letters*, 59, 393–403.

Özdemir, O., Dunlop, D. J., & Moskowitz, B. M. (1993). The effect of oxidation on the verwey transition in magnetite. *Geophysical Research Letters*, 20(16), 1671–1674.

Özdemir, O. & O′Reilly, W. (1978). Magnetic properties of monodomain aluminium-substituted titanomagnetite. *Physics of The Earth and Planetary Interiors*, 16(3), 190–195.

Özdemir, O. & O′Reilly, W. (1981). High-temperature hysteresis and other magnetic properties of synthetic monodomain titanomagnetites. *Physics of the Earth and Planetary Interiors*, 25(4), 406–418.

Pares, J. (2004). How deformed are weakly deformed mudrocks? Insights from magnetic anisotropy. In F. Martin-Hernandez, C. M. Lueneburg, C. Aubourg, & M. Jackson (Eds.), *Magnetic Fabric: Methods and Applications*, volume 238 of *Special Publications* (pp. 191–204). London: Geological Society of London.

Paterson, M. S. (1990). Rock deformation experimentation. In A. G. Duba, W. B. Durham, J. W. Handin, & H. F. Wang (Eds.), *The Brittle-Ductile Transition in Rocks*, volume 56 of *Geophysical Monograph* (pp. 187–194). Washington, DC: American Geophysical Union.

Pickart, S. & Turnock, A. (1959). Magnetic properties of solid solution of Fe_3O_4 and Fe_2AlO_4. *Physics and Chemistry of Solids*, 10, 242–244.

Pike, C., Roberts, A., & Verosub, K. (1999). Characterizing interactions in fine magnetic particle systems using first order reversal curves. *Journal of Applied Physics*, 85, 6660.

Pike, C., Roberts, A., & Verosub, K. (2001). First-order reversal curve diagrams and thermal relaxation effects in magnetic particles. *Geophysical Journal International*, 145(3), 721–730.

Poldervaart, A. & Gilkey, A. (1954). On clouded plagioclase. *American Mineralogist*, 39, 75–91.

Prior, D., Wheeler, J., Peruzzo, L., Spiess, R., & Storey, C. (2002). Some garnet microstructures: An illustration of the potential of orientation maps and misorientation analysis in microstructural studies. *Journal of Structural Geology*, 24(6-7), 999–1011.

Putnis, A. (1978). The mechanism of exsolution of hematite from iron-bearing rutile. *Physics and Chemistry of Minerals*, 3(2), 183–197.

Putnis, A., Hinrichs, R., Putnis, C., Golla-Schindler, U., & Collins, L. (2007). Hematite in porous red-clouded feldspars: Evidence of large-scale crustal fluid-rock interaction. *Lithos*, 95(1-2), 10–18.

Rabier, J., Veyssière, P., & Grilhé, J. (1976). Plastic deformation of $Ni_{0.66}Fe_{2.34}O_4$ spinel ferrite single crystals. *Journal of Materials Science*, 11(1), 193–195.

Ramberg, H. (1975). Particle paths, displacement and progressive strain applicable to rocks. *Tectonophysics*, 28, 1–37.

Ramsay, J. G. & Huber, M. I. (1983). *The Techniques of Modern Structural Geology Vol. 1: Strain Analysis.* Academic Press.

Rathore, J. S. & Becke, M. (1980). Magnetic fabric analyses in the Gail Valley (Carinthia, Austria) for the determination of the sense of movements along this region of the Periadriatic line. *Tectonophysics*, 69, 349–368.

Reddy, S., Timms, N., Pantleon, W., & Trimby, P. (2007). Quantitative characterization of plastic deformation of zircon and geological implications. *Contributions to Mineralogy and Petrology*, 153(6), 625–645.

Renne, P. R., Scott, G., Glen, J., & Feinberg, J. (2002). Oriented inclusions of magnetite in clinopyroxene: Source of stable remanent magnetization in gabbros of the Messum Complex, Namibia. *Geochemistry, Geophysics, Geosystems*, 3(12), 1079.

Roberts, A., Pike, C., & Verosub, K. (2000). First-order reversal curve diagrams: A new tool for characterizing the magnetic properties of natural samples. *Journal of Geophysical Research*, 105, 28461–28476.

Robie, R., Bethke, P., Toulmin, M., & Edwards, J. (1966). X-ray crystallographic data, densities, and molar volumes of minerals. *Handbook of Physical Constants*, (pp. 27–73).

Rochette, P. (1988). Inverse magnetic fabric in carbonate-bearing rocks. *Earth and Planetary Science Letters*, 90(2), 229–237.

Rochette, P., Jackson, M., & Aubourg, C. (1992). Rock magnetism and the interpretation of anisotropy of magnetic susceptibility. *Reviews of Geophysics*, 30(3), 209226.

Rosenbaum, J. G. (1993). Magnetic grain-size variations through an ash flow sheet: Influence on magnetic properties and implications for cooling history. *Journal of Geophysical Research*, 98(B7), 11715–11727.

Rosenbaum, J. G., Hudson, M. R., & Scott, R. B. (1991). Paleomagnetic constraints on the geometry and timing of deformation at Yucca Mountain, Nevada. *Journal of Geophysical Research*, B96, 1963–1980.

Ruf, A. S., Naruk, S. J., Butler, R. F., & Calderone, G. J. (1988). Strain and magnetic fabric in the Santa Catalina and Pinaleno Mountains metamorphic core complex mylonite zones, Arizona. *Tectonics*, 7(2), 235–248.

Rutter, E. H. (1974). The influence of temperature, strain rate and interstitial water in the experimental deformation of calcite rocks. *Tectonophysics*, 22(3-4), 311–334.

Rybacki, E. & Dresen, G. (2000). Dislocation and diffusion creep of synthetic anorthite aggregates. *Journal of Geophysical Research*, 105(B11), 26017–26.

Sawyer, D., Fleck, R., Lanphere, M., Warren, R., Broxton, D., & Hudson, M. (1994). Episodic caldera volcanism in the Miocene southwestern Nevada volcanic field: Revised stratigraphic framework, $^{40}Ar/^{39}Ar$ geochronology, and implications for magmatism and extension. *Bulletin of the Geological Society of America*, 106(10), 1304.

Schlinger, C. M., Veblen, D. R., & Rosenbaum, J. G. (1991). Magnetism and magnetic mineralogy of ash flow tuffs from Yucca Mountain, Nevada. *Journal of Geophysical Research*, 96(B4), 6035–6052.

Schmidt, V., Burlini, L., Hirt, A., & Leiss, B. (2008). Fabrication of synthetic calcite-muscovite rocks with variable texture–An analogue to cataclasite fabrics? *Tectonophysics*, 449, 105–119.

Sclar, C. (1979). Iron in lunar anorthite: Substitutional mechanism and subsolidus history. *Meteoritics*, 14(4).

Sclar, C. & Kastelic, R. (1979). Iron in anorthite: An experimental study. In *Lunar and Planetary Institute Science Conference Abstracts*, volume 10 (pp. 1087–1089).

Selkin, P. A., Gee, J. S., Meurer, W. P., & Hemming, S. R. (2008). Paleointensity record from the 2.7 Ga Stillwater Complex, Montana. *Geochemistry, Geophysics, Geosystems*, 9(12), Q12023.

Shcherbakov, V. & Fabian, K. (2005). On the determination of magnetic grain-size distributions of superparamagnetic particle ensembles using the frequency dependence of susceptibility at different temperatures. *Geophysical Journal International*, 162(3), 736–746.

Siemes, H., Hennig-Michaeli, C., & Martens, L. (1991). The importance of deformation experiments on minerals for the interpretation of metamorphic ore textures. *Ore Geology Reviews*, 6(5), 475–483.

Skemer, P., Katayama, I., Jiang, Z., & Karato, S. (2005). The misorientation index: Development of a new method for calculating the strength of lattice-preferred orientation. *Tectonophysics*, 411(1-4), 157–167.

Smirnov, A., Tarduno, J., & Pisakin, B. (2003). Paleointensity of the early geodynamo (2.45 Ga) as recorded in Karelia: A single-crystal approach. *Geology*, 31(5), 415.

Smith, J. & Brown, W. (1988). *Feldspar minerals: Crystal structures, physical, chemical, and microtextural properties*, volume 1. Springer-Verlag.

Snow, E. & Kidman, S. (1991). Effect of fluorine on solid-state alkali interdiffusion rates in feldspar. *Nature*, 349, 231–233.

Stacey, F. & Banerjee, S. (1974). *The Physical Principles of Rock Magnetism*.

Sugawara, T. (2001). Ferric iron partitioning between plagioclase and silicate liquid: Thermodynamics and petrological applications. *Contributions to Mineralogy and Petrology*, 141(6), 659–686.

Sugiura, N. (1979). ARM, TRM and magnetic interactions: Concentration dependence. *Earth and Planetary Science Letters*, 42(3), 451–455.

Tarduno, J., Cottrell, R., & Smirnov, A. (2006). The paleomagnetism of single silicate crystals: Recording geomagnetic field strength during mixed polarity intervals, superchrons, and inner core growth. *Reviews of Geophysics*, 44(1), RG1002.

Tarduno, J., Cottrell, R., Watkeys, M., & Bauch, D. (2007). Geomagnetic field strength 3. 2 billion years ago recorded by single silicate crystals. *Nature*, 446(7136), 657–660.

Tarduno, J. A. & Cottrell, R. D. (2005). Dipole strength and variation of the time-averaged reversing and nonreversing geodynamo based on Thellier analyses of single plagioclase crystals. *Journal of Geophysical Research*, 110, B11101.

Tarling, D. H. & Hrouda, F. (1993). *The Magnetic Anisotropy of Rocks*. London: Chapman and Hall.

Tegner, C. (1997). Iron in plagioclase as a monitor of the differentiation of the Skaergaard intrusion. *Contributions to Mineralogy and Petrology*, 128(1), 45–51.

Terry, M. & Heidelbach, F. (2006). Deformation-enhanced metamorphic reactions and the rheology of high-pressure shear zones, Western Gneiss Region, Norway. *Journal of Metamorphic Geology*, 24(1), 3–18.

Till, J., Jackson, M., & Moskowitz, B. (2010). Remanence stability and magnetic fabric development in synthetic shear zones deformed at 500°C. *Geochemistry Geophysics Geosystems*, 11(12), Q12Z21.

Till, J., Jackson, M., Rosenbaum, J., & Solheid, P. (2011). Magnetic properties in an ash flow tuff with continuous grain size variation: A natural reference for magnetic particle granulometry. *Geochemistry Geophysics Geosystems*, 12(7), Q07Z26.

Tullis, T., Horowitz, F., & Tullis, J. (1991). Flow laws of polyphase aggregates from end-member flow laws. *Journal of Geophysical Research*, 96(B5), 8081–8096.

Turner, F. J., Griggs, D. T., & Heard, H. (1954). Experimental deformation of calcite crystals. *Geological Society of America Bulletin*, 65(9), 883–934.

Uyeda, S., Fuller, M. D., Belshé, J. C., & Girdler, R. W. (1963). Anisotropy of magnetic susceptibility of rocks and minerals. *Journal of Geophysical Research*, 68(1), 279–291.

Veyssiere, P., Rabier, J., Garem, H., & Grilhe, J. (1978). Influence of temperature on dissociation of dislocations and plastic deformation in spinel oxides. *Philosophical Magazine A*, 38(1), 61–79.

Vigneresse, J. & Tikoff, B. (1999). Strain partitioning during partial melting and crystallizing felsic magmas. *Tectonophysics*, 312(2-4), 117–132.

Walker, A. N., Rutter, E. H., & Brodie, K. H. (1990). Experimental study of grain-size sensitive flow of synthetic, hot-pressed calcite rocks. *Geological Society, London, Special Publications*, 54(1), 259–284.

Wark, D. & Watson, E. (2006). Titaniq: A titanium-in-quartz geothermometer. *Contributions to Mineralogy and Petrology*, 152(6), 743–754.

Wenk, H., Canova, G., Molinari, A., & Mecking, H. (1989). Texture development in halite: Comparison of Taylor model and self-consistent theory. *Acta Metallurgica*, 37(7), 2017–2029.

Wenk, H., Ischia, G., Nishiyama, N., Wang, Y., & Uchida, T. (2005). Texture development and deformation mechanisms in ringwoodite. *Physics of the Earth and Planetary Interiors*, 152(3), 191–199.

Wilke, M. & Behrens, H. (1999). The dependence of the partitioning of iron and europium between plagioclase and hydrous tonalitic melt on oxygen fugacity. *Contributions to Mineralogy and Petrology*, 137(1), 102–114.

Worm, H. & Markert, H. (1987). Magnetic hysteresis properties of fine particle titanomagnetites precipitated in a silicate matrix. *Physics of the Earth and Planetary Interiors*, 46(1-3), 84–92.

Worm, H.-U. & Jackson, M. (1999). The superparamagnetism of Yucca Mountain Tuff. *Journal of Geophysical Research*, 104(B11), 25,415–25,425.

Yamazaki, D. & Karato, S. (2002). Fabric development in (Mg,Fe)O during large strain, shear deformation: Implications for seismic anisotropy in Earth's lower mantle. *Physics of the Earth and Planetary Interiors*, 131(3-4), 251–267.

Yu, Y. & Dunlop, D. J. (2001). Paleointensity determination on the Late Precambrian Tudor Gabbro, Ontario. *Journal of Geophysical Research*, 106(B11), 26,331–26,343.

Yu, Y., Dunlop, D. J., & Özdemir, O. (2002). Partial anhysteretic remanent magnetization in magnetite 1. Additivity. *Journal of Geophysical Research*, 107(B10), 2244.

Yund, R. (1986). Interdiffusion of NaSi-CaAl in peristerite. *Physics and Chemistry of Minerals*, 13(1), 11–16.

Yund, R. & Davidson, P. (1978). Kinetics of lamellar coarsening in cryptoperthites. *American Mineralogist*, 63(5-6), 470.

Yund, R. & Snow, E. (1989). Effects of hydrogen fugacity and confining pressure on the interdiffusion rate of NaSi–CaAl in plagioclase. *Journal of Geophysical Research*, 94(B8), 10662–10.

Zack, T., Moraes, R., & Kronz, A. (2004). Temperature dependence of Zr in rutile: Empirical calibration of a rutile thermometer. *Contributions to Mineralogy and Petrology*, 148(4), 471–488.

Zijderveld, J. (1967). A.C. demagnetization of rocks: Analysis of results. In D. W. Collinson et al. (Ed.), *Methods in Paleomagnetism* (pp. 254–286). Amsterdam: Elsevier.

Zitzelsberger, A. & Schmidbauer, E. (1999). Temperature dependence of magnetic hysteresis properties, and thermoremanent and anhysteretic remanent magnetization of stress-controlled synthetic 1-125 μm titanomagnetite ($Fe_{2.3}Ti_{0.7}O_4$) particles. *Geophysical Journal International*, 136(3), 505–518.